1-D Particle-in-cell simulations of plasmas with kappa velocity distributions

by

Reginald Francis Abdul

Submitted in fulfilment of the requirements for the degree of Master of Science in the School of Chemistry and Physics, University of KwaZulu-Natal, Westville, June 2013.

Abstract

The main aim of this project was the development of a particle-in-cell (PIC) plasma simulation code. While particle-in-cell simulations are not new, they have largely focused on using an initial Maxwellian particle loading. The new feature the code implemented for this project is the use of kappa distributions as an initial loading. This specialises the code for the investigation of waves and instabilities in space plasmas having kappa-type velocity distributions. The kappa distribution has been found to provide a better fit to space plasma particle velocity distributions than the Maxwellian in a wide variety of situations. In particular, it possesses a power law tail which is a frequent feature of charged particle velocity distributions in space plasmas.

Traditionally, the treatment of such out-of-equilibrium velocity distributions has been via a summation over several Maxwellians with different temperatures and average number densities. Instead, the approach used in this work is guided by recent advances in non-extensive statistical mechanics, which provide a rigorous underpinning for the existence of kappa distributions.

As case studies, the simulation code was used to investigate the ion-acoustic instability as well as electrostatic Bernstein waves in both Maxwellian and kappa plasmas. Results were compared to kinetic theory and the differences in the Maxwellian and kappa plasma behaviours are discussed. To analyse the instabilities various diagnostics were used, including Fourier analysis of the wave fields to determine the dispersion relation, and particle binning to determine the particle velocity distributions. Both the Maxwellian and kappa particle loading algorithms were found to agree well with the theoretical velocity distributions and the dispersion relations were found to agree with kinetic theory for both kappa and Maxwellian plasmas.

The code was developed in the C programming language using an incremental approach that enabled careful testing after each new level of sophistication was added. A version of the code was parallelised using Message Passing Interface (MPI) to take advantage of the distributed supercomputing environment provided by the CHPC.

Preface

The work described in this dissertation was carried out by the author from January 2011 to June 2013, in the School of Chemistry and Physics, University of KwaZulu-Natal, Westville, under the supervision of Professor R. L. Mace.

These studies represent original work by the author and have not otherwise been submitted in any form for a degree or diploma to another tertiary institution. Where use was made of the works of others, it has been duly acknowledged in the text.

DECLARATION 1 - PLAGIARISM

I, ..., declare that

1. The research reported in this dissertation, except where otherwise indicated, is my original research.

2. This dissertation has not been submitted for any degree or examination at any other university.

3. This dissertation does not contain other persons' data, pictures, graphs or other information, unless specifically acknowledged as being sourced from other persons.

4. This dissertation does not contain other persons' writing, unless specifically acknowledged as being sourced from other researchers. Where other written sources have been quoted, then: (a) Their words have been rewritten but the general information attributed to them has been referenced (b) Where their exact words have been used, then their writing has been placed in italics and inside quotation marks, and referenced.

5. This dissertation does not contain text, graphics or tables copied and pasted from the Internet, unless specifically acknowledged, and the source being detailed in the dissertation and in the References sections.

Signed: .....

Contents

Acknowledgements

I would first and foremost like to thank my supervisor Prof. R. L. Mace for his support, extensive knowledge and for his efforts in helping me improve my research abilities. His advice and guidance throughout this project has been invaluable.

I extend my sincere thanks to Prof. S. R. Pillay for all his encouragements, tireless assistance and advice over the years.

I thank my fellow students, Sharmini Pillay, Farran Henning, Francois Nsengiyumva and Harry Pillay, for useful discussions and support during this project.

To my family, thank you for all the sacrifices, unwavering support and encouragements you have given me.

The financial assistance of the National Research Foundation (NRF) towards this research is hereby acknowledged. Opinions expressed and conclusions arrived at, are those of the author and are not necessarily to be attributed to the NRF.

List of commonly used symbols

e	charge of an electron
$\boldsymbol{B}_0$	a static magnetic field
$\boldsymbol{E}$	electric field
E_e, E_f, E_i, E_{tot}	energies in the plasma
$f(v)$	particle velocity distribution
${}_pF_q[\cdots]$	hypergeometric function
i	particle index
$I_n()$	modified Bessel function of order n
j	grid index
k	wavenumber
L	simulation box length
m_e, m_i	mass of an electron and ion
n_{0e}, n_{0i}	number density for electron and ion species
$S(x)$	particle shape function
t	time
Δt	simulation time step
T	temperature in energy units
$\boldsymbol{v}$	velocity vector
v_d	drift velocity of plasma species
v_s, v_s^κ	ion sound speed for Maxwellian and kappa plasmas
v_{the}	thermal velocity of plasma particles
x_i	position of a particle
Δx	cell size
X_j	location of grid point

α	an arbitrary plasma species
$\Gamma()$	gamma function
ϵ_0	permittivity of free space
θ	generalised thermal speed
κ	kappa index
$\lambda_{De}, \lambda_{\kappa e}$	Debye length in Maxwellian and kappa plasmas
ρ	charge density
ϕ	scalar potential
$\varphi()$	Stix function
ω_{ce}, ω_{ci}	cyclotron frequency of electrons and ions
ω_{pe}, ω_{pi}	plasma frequency of electron and ion species
ω_{uh}, ω_{lh}	the hybrid frequencies

Chapter 1

Introduction

Space plasmas are a rich source of waves and instabilities. Owing to the dynamic nature of the space plasma environment, sources of free energy are abundant and plasma waves and instabilities are spontaneously produced. The investigation of plasma waves and instabilities is vital to a proper understanding of space plasma dynamics and the interpretation of satellite observations. Kinetic theory considers the particle velocity distribution for each plasma species and provides the most comprehensive description of the plasma, but also the most complex (Swanson, 2003).

The thermodynamic equilibrium state, modelled by the Maxwellian distribution, is often used in the kinetic investigation of plasma waves. However, space plasmas are seldom in an equilibrium state and non-Maxwellian velocity distributions are often observed (Treumann et al., 2004; Leubner, 2004; Livadiotis and McComas, 2009). These non-Maxwellian velocity distributions often exhibit power law tails owing to an over abundance of high energy, or suprathermal particles (Parker and Tidman, 1958). It has generally been suggested that the suprathermal particles gain energy as a result of Fermi acceleration at collisionless shocks (Parker and Tidman, 1958; Drury, 1983), but other mechanisms are also known to lead to similar energisation.

Vasyliunas (1968) introduced the kappa distribution function as a fit to observed space plasma velocity distributions, and successfully modelled satellite OGO 1 and OGO 3 solar wind electron data. The isotropic three-dimensional kappa distribution, in the form given by Summers and Thorne (1991), is

$$f(\boldsymbol{v}) = (\pi\kappa\theta^2)^{-3/2}\frac{\Gamma(\kappa+1)}{\Gamma(\kappa-1/2)}\left(1+\frac{\boldsymbol{v}^2}{\kappa\theta^2}\right)^{-(\kappa+1)}, \tag{1.1}$$

where $\theta^2 = 2[(\kappa-3/2)/\kappa](T/m) = 2[(\kappa-3/2)/\kappa]v_{th}^2$ is known as the generalised thermal speed, Γ is the gamma function and the parameter κ shapes the tail of the distribution, with $\kappa \to \infty$ producing the Maxwellian distribution. On the other hand, for low κ values, the kappa distribution reduces to a power law distribution. Thus, the kappa distribution enables one to study a wide range of velocity distributions, ranging from the Lorentzian (for low values of κ) to the Maxwellian (for $\kappa \to \infty$).

The family of kappa distributions, Equation (1.1), have generally been found to provide a more realistic representation of observed particle velocity distributions in space plasmas than the Maxwellian distribution, or sums of Maxwellians (Pierrard and Lazar, 2010). In situ satellite observations have found kappa velocity distributions, with $2 < \kappa < 6$, for the solar wind ions (Gloeckler et al., 1992) and electrons (Maksimovic et al., 1997), for the ions in the terrestrial magnetosphere (Gloeckler and Hamilton, 1987) as well as for the terrestrial plasmasheet electrons and ions (Christon et al., 1988, 1989). The kappa distribution also has a significant theoretical foundation provided by Tsallis statistical mechanics (Tsallis, 1988), which provides a theoretical framework for describing and analysing systems out of equilibrium. The kappa distribution is thus an effective tool in the study of space plasma phenomena.

The use of kappa velocity distributions has become widespread in the analytical investigation of space plasmas. Both the modified plasma dispersion function Z_κ^*, valid only for integer values of κ (Summers and Thorne, 1991), and the generalised plasma dispersion function Z_κ, valid for arbitrary real κ values (Mace and Hellberg, 1995), have been successfully used to study waves and instabilities in plasmas with excess suprathermals. Thorne and Summers (1991), Meng et al. (1992) and Mace et al. (1998) investigated ion-acoustic waves in a kappa plasma and showed that the ion-acoustic speed was kappa dependent and that the growth rate of the instability was altered. Thermal fluctuations were also found to be enhanced in the kappa plasma (Mace et al., 1998). Further, Bryant (1996) and Mace et al. (1998) showed that the Debye shielding length depends significantly on the parameter κ of the kappa distribution. Mace (2003, 2004) and Henning et al. (2011) investigated Bernstein waves in a kappa plasma and showed that the dis-

persion relation of electron Bernstein modes had strong dependence on the parameter κ.

Although the kappa distribution has been successfully used in many analytical studies of space plasmas, it has yet to become as widespread in computer simulation studies of space plasmas. One of the goals of this research project will be to model and simulate plasmas having kappa distributions.

1.1 The computational simulation of plasmas

The use of computer simulations to model and investigate plasmas started in the late 1950s, with the large scale systematic effort to model fusion plasmas (Tajima, 1989), and has since provided an effective means to study plasma wave phenomena. They are especially useful as a tool to study the non-linear regime of plasma wave evolution where analytical investigation may be difficult (Matsumoto and Omura, 1993). The analytical modelling of plasmas often employs simplification and approximation, i.e., analysis usually assumes linearity or weak non-linearity or symmetry characteristics (Dawson, 1983; Matsumoto and Omura, 1984; Dawson et al., 1993; Treumann and Baumjohann, 1997). Conversely, computer simulations maintain high levels of physical detail and can describe, with minimal approximation, the non-linear regime of plasma wave instabilities, from growing modes to eventual saturation and quenching of the instabilities, producing new equilibrium states (Forslund, 1985; Tajima, 1989; Dawson et al., 1993). Thus, plasma simulation extends and complements linear analysis and can provide a deeper understanding of plasma waves and instabilities. The rapid emergence, and ready availability, of fast modern computing and the increase in memory capacity further motivates the use of the computer as a tool in the study of plasma waves and instabilities as increasingly large scale plasma simulations become feasible (Dawson, 1985; Forslund, 1985; Dawson et al., 1993).

The numerical simulation of plasmas can be broadly classified into different types, each of which describes the plasma in varying levels of detail and resolution.

In magnetohydrodynamic (MHD) simulations, the plasma is modelled as a continuous fluid and the evolution of the fluid in its self-consistent electromagnetic field is followed (Matsumoto and Omura, 1984). The magnetohy-

drodynamic fluid equations (see Chen, 2006, p. 184) are used to describe the plasma dynamics and together with the appropriate set of Maxwellian equations, are numerically solved in the simulation (Birdsall and Langdon, 1985; Matsumoto and Omura, 1993). Simple fluid (MHD) models coarse grain the single particle effects and kinetic phenomena such as damping and non-linear saturation of microinstabilities are not resolvable (Winske and Omidi, 1996). Thus, MHD simulations are useful in the understanding of the long time macroscopic, global-scale dynamics of plasmas (Matsumoto and Omura, 1984; Tajima, 1989; Matsumoto and Omura, 1993) and have been used to investigate large scale plasma systems, e.g., the Earth's magnetosphere was simulated by Leboeuf et al. (1978, 1981) in two and three dimensions to produce an interplanetary magnetic field and the interaction of the solar wind with the magnetosphere was simulated by Brecht et al. (1981, 1982) and Groth et al. (2000).

Kinetic simulations provide the most detailed description of the plasma and consider the interaction between the plasma particles and the electromagnetic fields (Birdsall and Langdon, 1985; Tajima, 1989; Winske and Omidi, 1996). These simulations are required when single particle effects such as wave particle interactions, particle heating and acceleration and wave saturation are important (Matsumoto and Omura, 1984; Forslund, 1985; Winske and Omidi, 1996). Kinetic simulations include Vlasov simulations, which directly solve the Vlasov equation on a phase space grid (Bertrand, 2005), and particle-in-cell simulations, which model the plasma as being composed of particles and follows the trajectories of each particle throughout the simulation (Hockney and Eastwood, 1981; Birdsall and Langdon, 1985). Matsumoto and Omura (1984), Kasaba et al. (2001), Hellinger et al. (2004) and Lu et al. (2005) have used kinetic simulations to investigate the excitation and non-linear evolution of plasma waves and instabilities, using plasma beams to excite instabilities such as the ion-acoustic and the electron-acoustic instability.

Hybrid simulations refer to those which model part of the plasma using an individual particle approach, as done in PIC, and part as a fluid, as done in MHD (Winske and Omidi, 1996; Giacalone, 2006). The most common type of hybrid simulation of space plasmas, models the ions as particles, with electrons modelled as a singly charged, neutralising, mass-less fluid, thus allowing the investigation of phenomena on the slower ion time scales (Matsumoto and Omura, 1993; Dawson et al., 1993; Winske and Omidi, 1996). Examples of the application of hybrid simulations can be found in

the simulation studies of the Earth's bow shock, where time scales of interest are usually on the order of the ions, such as those carried out by Winske (1985), Quest (1988), Omidi and Winske (1990), Matsumoto and Omura (1993) and Burgess (2006), among others.

1.2 The particle-in-cell simulation technique

The aim of this research project was to create plasma simulation codes using the particle-in-cell (PIC) simulation technique, where the PIC technique models the plasma as being composed of individual particles. The advantage of the PIC technique is its ability to simulate plasma micro-instabilities and their non-linear evolution (Matsumoto and Omura, 1984; Birdsall and Langdon, 1985; Forslund, 1985; Tajima, 1989). Presented in this section is a general description of the particle-in-cell technique as well a brief history of particle-in-cell simulations, outlining the development in the sophistication of the models used, from the early one dimensional electrostatic models to the massively parallel, electromagnetic simulations run today. A detailed description of the simulation code developed for this thesis is presented in Chapter 2.

In the particle-in-cell method, simulation particles are initialised by assigning to each an initial position and velocity, according to some given statistical distribution. The trajectories of the particles are then calculated using the Newton-Lorentz equations, employing the self-consistent electromagnetic fields, which are determined from Maxwell's equations (Hockney and Eastwood, 1981; Birdsall and Langdon, 1985; Tajima, 1989). Externally applied fields are readily taken into account. Limitations in early computing power, however, greatly reduced the sophistication of the early plasma simulation models, i.e., early simulations were one dimensional and often relied on the electrostatic approximation, the particles usually took the form of charged sheets and the fields were calculated directly from the particle positions (Birdsall, 1991).

Even with the early lack of sophistication, particle simulation was still an effective tool in the study of plasmas. In one of the first papers on particle simulations, Buneman (1959) simulated cold electrons drifting through cold ions and showed that the electron beam loses its drift motion in the produced instability. The loss in drift motion amounted to an effective col-

lision rate, on the order of the growth rate of the instability, and was a possible explanation for the mechanism of electron-cooling in low pressure RF discharges. Dawson (1962) simulated warm particles in the form of negatively charged sheets, using 5 to 20 sheets per Debye length, embedded in a uniform neutralising background of positive charge. The properties of the plasma system, such as the velocity distribution of the particles, the thermalising properties of the plasma, diffusion in velocity space and the drag on fast and slow sheets were examined and found to be in agreement with theoretical predictions. The results of Dawson (1962) showed that the kinetic behaviour of plasmas could be observed in one dimensional simulations using only a small number of particles per Debye length. Furthermore, Dawson (1964) demonstrated the effects of Landau damping (Landau, 1946) of electrostatic waves which, at the time, was predicted by theory but had not yet been observed experimentally.

As mentioned above, in the particle-in-cell method the particle dynamics and fields are governed by Newton's and Maxwell's equations, respectively. These equations are numerically integrated in time throughout the simulation and this numerical integration places limits on the allowable time steps, ensuring stability of the method (Hockney and Eastwood, 1981; Birdsall and Langdon, 1985). These stability constraints make the particle-in-cell technique computationally expensive, as a number of calculations are computed for every particle at every time step and the number of time steps required to produce a significant degree of plasma evolution is high. Thus, the domain of the simulated plasma is usually confined to a small region of interest (Dawson, 1983; Forslund, 1985).

To reduce computation time, the domain of the simulation, known as the simulation box (Birdsall and Langdon, 1985), is partitioned into cells of (usually) equal size, Δx. This refinement was introduced to make two-dimensional simulations more practical, by Yu et al. (1965) and Hockney (1965, 1966). The simulation particles are free to move through the grid, depositing charge and current densities to the grid points, located at the center of each cell (Hockney and Eastwood, 1981; Dawson, 1983; Birdsall and Langdon, 1985). Usually, a predefined weighting scheme, such as the nearest-grid-point (NGP) scheme, used by Hockney (1965, 1966), is used to determine how the charge and current densities are assigned to grid points. In the NGP scheme, the charge density is accumulated at a grid point by combining the charge from every particle lying within the associated cell. The charge and current densities at the grid points then provide the sources

for Maxwell's equations, which are solved in discrete form on the grid, as opposed to being calculated directly from the particle positions. This reduces the number of calculations performed, as there are usually fewer grid points than there are number of particles, and the number of calculations computed per time step is reduced from N^2 to $N \log N$ (Dawson, 1983). Since the particle positions no longer coincide with the positions at which the fields are known, a weighting scheme is required to interpolate the electromagnetic fields, at the grid points, back to the particle positions to obtain the electromagnetic force on each particle.

The simulation cells are not required to be of equal size. Berger and Oliger (1984) developed the adaptive mesh refinement technique for particle simulations. Here the spatial grids in the simulation could be redefined and more grid points could be added to regions of interest. This allowed the resolution of the plasma spatial domain to be dynamically defined. Brackbill (1993) created the moving mesh adaptation method which can be used to move grid points to regions of interest, from other regions.

Particles moving in and out of the simulation cells, in the nearest-grid-point scheme, had the effect of producing noisy electromagnetic fields, due to the drastic changes in charge density at the grid points (Forslund, 1985; Birdsall and Langdon, 1985). High levels of noise in a simulation can distort or disguise important physical processes under investigation. To reduce the inherent noise and enhanced fluctuations and collisionality in the simulations, the finite-size macro-particle technique was constructed, independently, by Birdsall and Fuss (1969) and Morse and Nielson (1969). Birdsall and Fuss (1969) introduced the cloud-in-cell (CIC) scheme and Morse and Nielson (1969) introduced the particle-in-cell (PIC) scheme (not to be confused with the particle-in-cell simulation technique which is the name given to a class of simulations). Birdsall and Fuss (1969) assumed the simulation particles were finite sized, tenuous "clouds" of uniform charge density, with an effective particle shape. The charged clouds were allowed to pass freely through each other and the charge assigned to a grid point was taken as the overlap of the cloud with a cell. Coulomb interactions on scales smaller than a particle's size were smoothed out and the assignment of charge to the grid points produced less noisy electromagnetic fields. Okuda and Birdsall (1970) showed that collision cross sections were greatly reduced when using the cloud-in-cell scheme over the nearest-grid-point scheme when the size of the clouds were made comparable to the Debye length. Morse and Nielson (1969) assumed no shape or size for their simulation particles; however,

each particle distributed its charge between the two nearest grid points, in a one dimensional simulation, using linear interpolation. The linear interpolation was also found to reduce noise in the simulation when compared to the nearest-grid-point scheme.

Noise in the simulation is not only attributed to the weighting scheme used, but also arises due to the random loading of particles in the simulation. Randomly loading particles in phase space can produce plasmas with fully developed fluctuation levels which can be enhanced when too few particles are used (Birdsall and Langdon, 1985; Sydora, 1999). In general, the noise in the simulation decreases as $N_p^{-1/2}$, where N_p is the total number of simulation particles (Dawson, 1983). Byers and Grewal (1970) implemented the quiet start technique which attempts to load the plasma particles as smoothly as possible in phase space, reducing the noise produced by the random loading of particles, by imposing an order on their initial conditions. However, quiet starts only reduce noise briefly, as the plasma simulation deteriorates from the quiet start and becomes noisy again (Dawson, 1983; Lapenta, 2012). Aydemir (1994) and Denton and Kotschenreuther (1995) implemented the δf PIC algorithm which greatly reduces noise in the simulation. The δf PIC algorithm separates the total particle distribution into a background part f_0 and perturbed part δf, i.e., the total distribution function is $f = f_0 + \delta f$. The perturbed part of the distribution is represented using the simulation particles and the background part is represented analytically. Charge and current densities are then computed analytically from f_0 and statistically from δf using the usual particle-in-cell techniques. The δf PIC algorithm allows for more accurate determination of growth and saturation of weak kinetic micro-instabilities than the usual PIC technique (Sydora, 1999).

Plasma phenomena usually encompass multiple time scales. Stable particle-in-cell simulations, however, usually require the resolution of the high electron plasma frequency, or cyclotron frequency, and the Debye length (Hockney and Eastwood, 1981; Birdsall and Langdon, 1985). Cohen et al. (1982) analysed implicit time-differencing techniques for particle-in-cell simulations, which solve equations in the simulation implicitly in time and were found to remain stable even when a large time step was used. Implicit time differencing afforded the investigation of plasma phenomena on slower time scales without the need to resort to long simulation runs. Adam et al. (1982) developed the electron sub-cycling technique, due to the disparate dynamics of particles of varying mass. Standard particle updating was used, such as the leap-frog method; however, the lighter electrons were advanced on a time

step that was a fraction of that of the heavier ions. For each complete cycle of time integration there is one cycle for the ions and several sub-cycles for the electrons. Thus, the plasma species are allowed to be resolved at their own natural time scales of motion and computation time is saved as the dynamics of the heavier ion species are not updated as often as the lighter electron species.

Out of the need to run larger scale simulations, using millions of particles without resorting to prohibitively long simulation runs, particle-in-cell simulations were ported to the parallel computing environment. Huff et al. (1982) began early work in parallelisation of particle simulations, which allowed concurrent computation of the simulation equations and resulted in increased execution speeds. Two types of computer memory exists in parallel architectures, these are, shared and distributed memory. In shared memory systems all processors have access to the same memory block and inter-processor communication is usually done via the shared main memory. In distributed memory systems each processor is independently assigned a memory block and inter-processor communication is done via message passing. Horowitz et al. (1989) developed the first parallel particle-in-cell simulation to run on a shared memory system, such as the Cray computer. Jackson and Zaidman (1987) utilised message passing interface (MPI) and developed simulations, in LISP, which could run on distributed memory systems such as the Connection Machine. Due to their high computing power and capability for massive data parallelism, simulation codes were also made to work on graphical processing units (GPUs) by Stanchev et al. (2009), Decyk and Singh (2011) and Abreu et al. (2011). NVIDIA GPUs were used with CUDA (Compute Unified Device Architecture) and simulations could be conducted using many millions of particles.

Generally, in the parallelisation of the simulation code, one of two methods are used (Dawson et al., 1993). In the first method, implemented by Liewer et al. (1988), particles are divided among the processors and all other quantities are replicated on each processor. The distribution of particle calculations among the available processors works well only on a small number of processors (approximately 10) and does not efficiently scale to the use of a larger number of processors (Dawson et al., 1993). In the second method, implemented by Liewer and Decyk (1989), both particles and field quantities are distributed among the available processors. Each processor is assigned a region of the simulation box and all particles and field values associated with that region. The parallelisation scheme used by Liewer and Decyk (1989)

was found to efficiently run very large scale simulations using millions of particles on a large number of processors.

Liewer et al. (1990) increased the parallel efficiency of the simulation code of Liewer and Decyk (1989) by dynamically balancing the work done on each processor. Dynamic load balancing allows spatial boundaries to change during the course of the simulation in order to maintain an equal number of particles on each processor. Increasing the efficiency of the parallelisation scheme allowed simulations to run faster. Bettencourt and Greenwood (2008) investigated the parallel efficiency of particle-in-cell simulations, and observed that not only the performance of the CPU used, but also memory access patterns affected the execution speeds of the simulation.

Chapter 2

Simulation model and basic equations

The particle-in-cell (PIC) simulation code created and described in this thesis was written using the C programming language. The simulation code is one dimensional, i.e., fields and sources vary only in one dimension x and only the x component of the particle position vector is relevant; however, all three components of its velocity are retained and are necessary when a magnetic field, directed at an angle to x, is present. The simulation code is electrostatic but allows for a uniform, static magnetic field $\boldsymbol{B}_0$, which can be directed at arbitrary angles with respect to x. In all simulations carried out and presented in this thesis, periodic boundary conditions were used for the particles and fields.

An overview of our particle-in-cell simulation code is given in the schematic diagram in Figure 2.1. The simulation starts (at time t_0) by loading all plasma particles into the simulation box with a chosen velocity and spatial density distribution [see Figure 2.1 (a)].

During the initialisation phase [Figure 2.1 (b)], the particle velocities are stepped forward from time t_0 to $t_0 + \Delta t/2$, where Δt is the length of the time step used in the simulation. The particle velocities are stepped forward by firstly interpolating the initial particle positions to the discrete grid and accumulating charge density at the grid points [Figure 2.1 (c)]. Second, the electric field is calculated on the discrete grid using the accumulated charge density [Figure 2.1 (d)]. The electric field is then interpolated from the

discrete grid points to the particle positions [Figure 2.1 (e)] and the particle velocities are stepped forward to time $t_0 + \Delta t/2$, using the interpolated electric field [Figure 2.1 (f)]. The particle velocities are then evaluated at half integer time steps, $t_0 + (n + 1/2)\Delta t$, for the remainder of the simulation. This enables the implementation of the leap-frog technique to update the particle positions from the particle velocities during the simulation, i.e., in the particle pusher [Figure 2.1 (f)].

After this initial synchronising call to the simulation cycle in Figures 2.1 (c) to (f), the particle velocities are stepped forward for the full time step Δt for the remainder of the simulation run, i.e., the particle velocities are evaluated at the times $t_0 + (n + 1/2)\Delta t$, where $n = 0, 1, 2, \cdots$. The particle positions are updated using the leap-frog technique and the velocities at the half integer time steps, and the simulation progresses through the repetition of the cycle in Figures 2.1 (c) to (f), solving Newton's and Poisson's equations in discrete form at each time step to the end of the simulation run.

Details for each of the steps in Figure 2.1 (a) and Figures 2.1 (c) to (f) are presented in the subsequent sections.

2.1 Loading particles into the simulation box

The code we developed is designed to simulate multi-species plasmas. Each plasma species used in the simulation is created by reading in, from an input file, its number of particles, its plasma frequency, charge-to-mass ratio, thermal speed and species drift. After all species are formally created, every plasma particle is loaded into the simulation box by allocating to each initial conditions in phase space, i.e., every particle is given an initial position x and velocity $\boldsymbol{v}$ by sampling from a chosen distribution (Hockney and Eastwood, 1981; Dawson, 1983; Birdsall and Langdon, 1985; Tajima, 1989). Although the simulation is one dimensional, all three components of velocity can be used. This type of simulation is known as a one-and-two-halves dimensional simulation, with x being the full dimension and y and z the half dimensions (Dawson, 1983; Tajima, 1989).

In all simulations carried out and presented in this thesis, particle positions are loaded uniformly throughout the simulation box using the C intrinsic function `random()`, provided by the UNIX system. The function `random()` creates a set of pseudo-random numbers, uniformly distributed over the

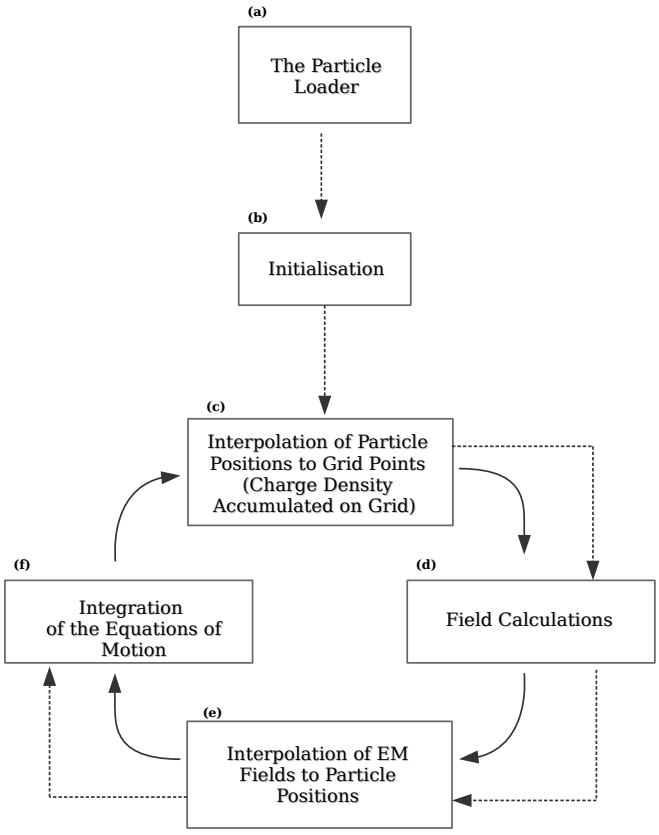

Figure 2.1: Schematic diagram of our one dimensional particle-in-cell simulation. Once (a) all particles are loaded into the simulation box, (b) the initialisation phase is used to step forward the particle velocities by half the time step, enabling the implementation of the leap-frog technique. The velocities are stepped forward using the simulation cycle described by (c) to (f). After the initial call to the simulation cycle (c) to (f) to step the particle velocities to the half time step, the particle velocities will be stepped forward for the full time step. The simulation then reduces to the repetition of the cycle (c) to (f) at each iteration of the simulation until the end of the simulation run.

range $0 \rightarrow 2147483647$, with a period of $16 \times (2^{31} - 1)$. The random numbers are then normalised to 2147483647, giving a uniformly distributed random number with the range $0 \rightarrow 1$. By multiplying these uniformly distributed deviates by the box length L, we allocate to the particle a position on the interval $[0, L]$.

Our simulation allows each species to have one of two initial states. Either the equilibrium state, governed by the Maxwellian distribution, or the metastable state, governed by the kappa distribution, is used. Initial states having such velocity distributions are created by generating random deviates from either the Maxwellian or the kappa distribution using the methods described in the following subsections.

2.1.1 Generating Maxwellian distributed random deviates

The Maxwellian distribution is widely used to model velocity distributions in plasmas which are in, or near, an equilibrium state. The one dimensional, drifting Maxwellian velocity distribution is given by (Ishihara, 1971),

$$f(v_x - v_d) = \left(\frac{1}{2\pi v_{th}^2}\right)^{1/2} \exp\left[-\frac{1}{2}\frac{(v_x - v_d)^2}{v_{th}^2}\right], \tag{2.1}$$

where v_d is the drift velocity of the plasma and $v_{th} = (T/m)^{1/2}$ is the thermal velocity of the particles. We measure particle temperature in energy units, thus, here and throughout this thesis, we omit the Boltzmann constant when temperatures appear.

The Maxwellian particle loader used in our simulation code generates random deviates from the Maxwellian distribution using the Box-Muller transform (Box and Muller, 1958). The Box-Muller transform is a transformation method for generating pairs of standard, normal distributed random deviates, from uniformly distributed random deviates.

To generate Maxwellian distributed random deviates, first, two deviates, a_1 and a_2, uniformly distributed on the interval $[0, 1]$, are transformed into two independent, normal distributed random deviates, b_1 and b_2, using the equations (Press et al., 2007, p. 364),

$$b_1 = \sqrt{-2\ln\, a_1}\,\cos(2\pi a_2), \tag{2.2}$$
$$b_2 = \sqrt{-2\ln\, a_1}\,\sin(2\pi a_2). \tag{2.3}$$

A derivation of Equations (2.2) and (2.3) is given in Appendix A. Appropriate random deviates $v_{1,2}$ from the Maxwellian distribution, with arbitrary mean (drift velocity v_d) and temperature T [thermal velocity $v_{th} = (T/m)^{1/2}$], are then obtained by applying the following linear transformation to each of the standard, normal deviates generated by Equations (2.2) and (2.3) (Press et al., 2007; Walck, 2007)

$$v_{1,2} = v_d + v_{th} b_{1,2}. \tag{2.4}$$

2.1.2 Generating kappa distributed random deviates

The kappa distribution is used to model the non-Maxwellian velocity distributions typically observed in space plasma populations having an over abundance of suprathermal particles (Vasyliunas, 1968; Maksimovic et al., 1997; Schippers et al., 2008). The isotropic one dimensional kappa distribution, in the form given by Summers and Thorne (1991), is

$$f(v_x) = (\pi\kappa\theta^2)^{-1/2}\frac{\Gamma(\kappa)}{\Gamma(\kappa - 1/2)}\left(1 + \frac{v_x^2}{\kappa\theta^2}\right)^{-\kappa}, \tag{2.5}$$

where $\theta^2 = 2[(\kappa - 3/2)/\kappa](T/m) = 2[(\kappa - 3/2)/\kappa]v_{th}^2$ is known as the generalised thermal speed, κ is the spectral index which shapes the tail of the kappa distribution, and Γ is the gamma function. For the kinetic temperature to remain finite, we require $\kappa > 3/2$, as can be seen from the definition of θ above. In the limit as $\kappa \to \infty$ the kappa distribution, Equation (2.5), reduces to the one dimensional Maxwellian distribution, Equation (2.1), with $v_d = 0$.

A plot of the one dimensional kappa distribution, Equation (2.5), for different values of the index κ, i.e., $\kappa = 2; 5; 8$ and 20, as well as the one dimensional Maxwellian distribution, Equation (2.1), is given in Figure 2.2,

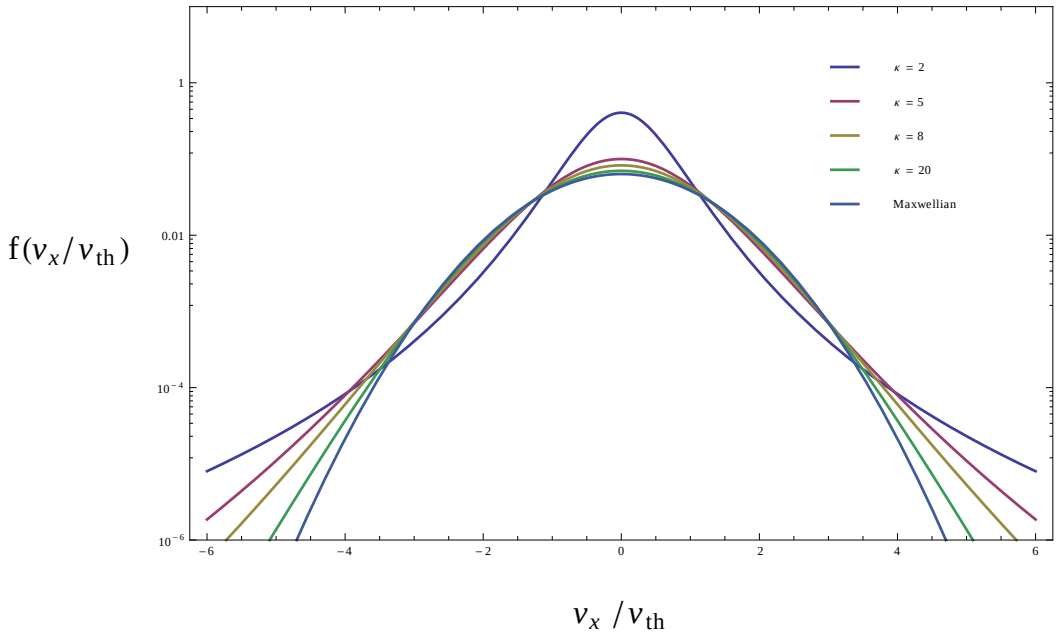

Figure 2.2: The one dimensional kappa distribution, Equation (2.5), shown for different values of the index κ, i.e., $\kappa = 2; 5; 8$ and 20, as well as the one dimensional Maxwellian distribution (corresponding to $\kappa = \infty$), Equation (2.1). Low values of κ give rise to significant power law tails and as the value of κ increases the distribution approaches the Maxwellian distribution, corresponding to $\kappa = \infty$.

each having unit thermal velocity, $v_{th} = 1$, and zero drift. The family of kappa distributions have a Maxwellian-like core at low $|v_x/v_{th}|$, with a high energy tail component which falls off as a power law $\propto v_x^{-2\kappa}$ (see Figure 2.2 for low values of κ). The power law tail of the kappa distribution is unlike the Maxwellian tail which falls off exponentially (compare the tail regions of the Maxwellian and $\kappa = 2$ plots in Figure 2.2). Thus the kappa distribution provides a better fit to observed space plasma velocity distributions exhibiting power law tails (Vasyliunas, 1968; Christon et al., 1988; Gloeckler et al., 1992). As the parameter κ increases, the tail of the distribution progressively decays and the kappa distribution approaches the Maxwellian distribution, as seen in the tail regions of the plots in Figure 2.2 where the number of high velocity particles decrease as κ increases.

Only a few particle-in-cell simulations have used kappa distributions to model particle velocities in phase space, e.g., see Lu et al. (2010, 2011) and Koen et al. (2012b). The majority of PIC simulations use the Maxwellian distribution, or one of its variants such as the bi-Maxwellian or drifting Maxwellian, or sums of these. One of the aims of this research was to create a particle loader using the kappa distribution and to use it to simulate and investigate the behaviour of non-Maxwellian plasmas. The kappa particle loader we devised uses deviates generated from the closely related Student t distribution (Press et al., 2007, p. 323), as opposed to using the rejection method employed by Koen et al. (2012b).

The univariate form of the Student t distribution is given by (Press et al., 2007; Shaw and Lee, 2008)

$$p(t) = \frac{1}{\sqrt{(\nu\pi)}\sigma} \frac{\Gamma\left(\frac{\nu+1}{2}\right)}{\Gamma(\frac{\nu}{2})} \left[1 + \frac{1}{\nu}\left(\frac{t-\mu}{\sigma}\right)^2\right]^{-\frac{1}{2}(\nu+1)}, \tag{2.6}$$

where μ is the mean of the distribution, with the variance given by $\nu\sigma^2/(\nu-2)$, and ν represents the number of degrees of freedom, which shapes the tail of the Student t distribution. Analogous to the kappa distribution, the Student t distribution has a power law distribution at significantly small ν. As ν increases the power-law tail of the Student t distribution decays more rapidly and the distribution approaches the normal distribution (Press et al., 2007, p. 323).

To illustrate the relation between the kappa and Student t distributions, we let the mean $\mu = 0$ in the Student t distribution in Equation (2.6) and define ν and σ^2, respectively, as

$$\nu = 2\kappa - 1, \tag{2.7}$$

$$\sigma^2 = \frac{\kappa\theta^2}{2\kappa - 1}. \tag{2.8}$$

Substituting Equations (2.7) and (2.8) into the equation for the Student t distribution, Equation (2.6), yields

$$
\begin{aligned}
p(t) &= \frac{1}{\sqrt{\pi(2\kappa-1)}}\sqrt{\frac{2\kappa-1}{\kappa\theta^2}}\frac{\Gamma\left(\frac{2\kappa}{2}\right)}{\Gamma\left(\kappa-\frac{1}{2}\right)}\left[1+\frac{t^2}{(2\kappa-1)}\frac{(2\kappa-1)}{\kappa\theta^2}\right]^{-\frac{1}{2}(2\kappa)} \\
&= \frac{1}{\sqrt{\pi\kappa\theta^2}}\frac{\Gamma(\kappa)}{\Gamma\left(\kappa-1/2\right)}\left[1+\frac{t^2}{\kappa\theta^2}\right]^{-\kappa}. \qquad (2.9)
\end{aligned}
$$

Equation (2.9) is equivalent to the definition for the one dimensional kappa distribution, Equation (2.5). Thus, having demonstrated how the Student t distribution, Equation (2.6), reduces to the one dimensional kappa distribution, Equation (2.5), we can use the well known method of generating deviates from the Student t distribution (Press et al., 2007, p. 371) to obtain deviates from the kappa distribution, by using the definitions in Equations (2.7) and (2.8).

The method for generating Student t deviates is similar to the Box-Muller transform described in the previous section. Two uniformly distributed deviates a_1 and a_2 are transformed into a deviate from the Student t distribution by first generating the deviate c, using an equation analogous to the Equations (2.2) and (2.3) (Press et al., 2007, p. 371)

$$c = \sqrt{\nu(a_1^{-2/\nu}-1)}\,\cos(2\pi a_2). \qquad (2.10)$$

In this case, however, only one deviate is generated at a time, unlike the Box-Muller transform which generates two (Bailey, 1994; Press et al., 2007). The appropriate deviate from the Student t distribution v_t, with arbitrary mean and standard deviation, is obtained via (Press et al., 2007, p. 371)

$$v_t = \mu + \sigma c. \qquad (2.11)$$

Using the definitions of ν and σ^2, in Equations (2.7) and (2.8), respectively, Equations (2.10) and (2.11) can be used to generate deviates from the kappa distribution. An arbitrary drift speed can be accounted for by setting $\mu = v_d$, as in the Maxwellian case [see Equation (2.4)]. A derivation of Equation (2.10) is given in Appendix B.

2.2 Particle and field interpolation

To represent the electric field $\boldsymbol{E}$, as well as the charge density ρ, the particle-in-cell technique employs a discrete sampling of the spatial domain (Hockney and Eastwood, 1981; Dawson, 1983; Matsumoto and Omura, 1984; Tajima, 1989). The spatial domain (or box) of the simulation is divided into cells of width Δx and the quantities $\boldsymbol{E}$ and ρ are stored only at the grid points j, located at the centre of each cell. Since the particle positions are not subject to discrete sampling, the particles are able to freely move through the spatial grid, depositing charge density at the grid points (Birdsall and Fuss, 1969; Birdsall and Langdon, 1985; Forslund, 1985). Hence some method must be devised for particles to deposit charge information onto and take field information from the grid.

In the particle-in-cell technique, an interpolation scheme is used to assign charge to the grid points in the vicinity of a particle. Conversely, to determine the force on a particle requires knowledge of the electric field at its position x. Since the electric field is known only at the discrete locations, separated spatially by a distance Δx, to determine the field at an arbitrary location, x, requires a further interpolation step. To avoid self forces, and conserve particle momentum, both particle and field interpolation schemes must be identical (Hockney and Eastwood, 1981; Dawson, 1983).

In the simulation code described in this thesis, we use the first-order weighting scheme, in one dimension, to assign charge from the particles to the grid (Birdsall and Fuss, 1969; Hockney and Eastwood, 1981; Birdsall and Langdon, 1985). The first-order weighting scheme divides the charge q_i of particle i, at position x_i, amongst its two nearest grid points j and $j+1$, at the positions X_j and X_{j+1}, respectively, using linear interpolation. In particular, the charge assigned to grid points j and $j+1$, respectively, by a particle located at x_i is given by (Birdsall and Langdon, 1985, p. 20)

$$Q_j = q_i \left[\frac{X_{j+1} - x_i}{\Delta x} \right], \tag{2.12}$$

$$Q_{j+1} = q_i \left[\frac{x_i - X_j}{\Delta x} \right]. \tag{2.13}$$

Alternatively, the linear interpolation scheme can be viewed as regarding the simulation particles as having finite size. In terms of this scheme, particles

located at x_i, are seen to be equivalent to finite sized, rigid clouds of uniform charge density, Δx wide and centred at x_i, which may pass freely through each other (Birdsall and Fuss, 1969). The assignment of charge to a grid point, in this interpolation scheme, corresponds to the amount of overlap between the cloud of uniform charge density and the grid cell corresponding to that grid point (Birdsall and Fuss, 1969), [see Figure 2.3 (a)].

The linear interpolation scheme can also be seen to produce an effective triangular particle shape function $S(x)$ of width $2\Delta x$ (Hockney and Eastwood, 1981; Dawson, 1983; Forslund, 1985), given as (Ueda et al., 1994)

$$S(x) = \frac{1}{\Delta x} \begin{cases} 1 - |x|/\Delta x, & \text{if } |x| < \Delta x \\ 0, & \text{otherwise} \end{cases} \tag{2.14}$$

The amount of charge density assigned to a grid point X_j, by a particle located at x_i is therefore determined by the value of $S(X_j - x_i)$ [see Figure 2.3 (b)]. In particular, for a total of N_p particles, each having the coordinate x_i, the total contribution to the charge density at X_j is

$$\rho_j = \sum_i q_i S(X_j - x_i). \tag{2.15}$$

The first order weighting scheme comes at some computational expense as two grid points need to be accessed per particle for every time step; however, fluctuations in the charge density, and ultimately the electric field, are reduced (Birdsall and Fuss, 1969; Hockney and Eastwood, 1981; Dawson, 1983; Forslund, 1985; Birdsall and Langdon, 1985).

Once all particles have deposited their charge on the grid, by evaluating Equations (2.12) and (2.13) for each particle, the electric field is calculated, using the accumulated charge density, and is stored in a separate grid.

A second interpolation is then required to map the calculated electric field on the grid back to the position of the particles, enabling a particle's position and velocity to be updated. Our simulation code uses a similar weighting scheme to the one used to interpolate the particle charge to the grid, to interpolate the electric field back to the particle positions, i.e., the electric field at the particle's position x_i is calculated from the electric field stored at the two nearest grid points to that particle.

The linear interpolation scheme used to map the electric field values E_{xj} and $E_{x(j+1)}$, at the grid points, j and $j+1$, corresponding to positions X_j and X_{j+1}, respectively, back to the position of a particle at x_i, is given by (Birdsall and Langdon, 1985, p. 22)

$$E_x(x_i) = E_{xi} = \left[\frac{X_{j+1} - x_i}{\Delta x}\right] E_{xj} + \left[\frac{x_i - X_j}{\Delta x}\right] E_{x(j+1)}. \tag{2.16}$$

Equation (2.16) should be compared with Equations (2.12) and (2.13) for the charge density case. It is this interpolated value of the electric field component E_{xi} that we use to update the particle velocities, which will be discussed later.

In general, a mixed set of particle interpolation and field interpolation schemes may be used, as long as the field interpolation calculations are of a lower order than that of the charge interpolation calculations; however, momentum will not be conserved exactly in this case (Hockney and Eastwood, 1981, p. 128).

2.3 Solutions of the field equations

As mentioned in the previous section, charge density from the particles is accumulated on the grid via linear interpolation. This charge density on the grid then provides the source term in Maxwell's equation which is used to obtain the electric field. Maxwell's equation, for our one dimensional simulation, is

$$\frac{dE_x}{dx} = \frac{\rho}{\epsilon_0}, \tag{2.17}$$

where E_x is the x component of the electric field, ρ is the charge density and ϵ_0 is the permittivity of free space. Particle-in-cell simulations usually employ a system of units such that the value of ϵ_0 can be arbitrarily chosen, while satisfying (Matsumoto and Omura, 1984; Omura, 2007)

$$\frac{1}{\epsilon_0 \mu_0} = c^2,$$

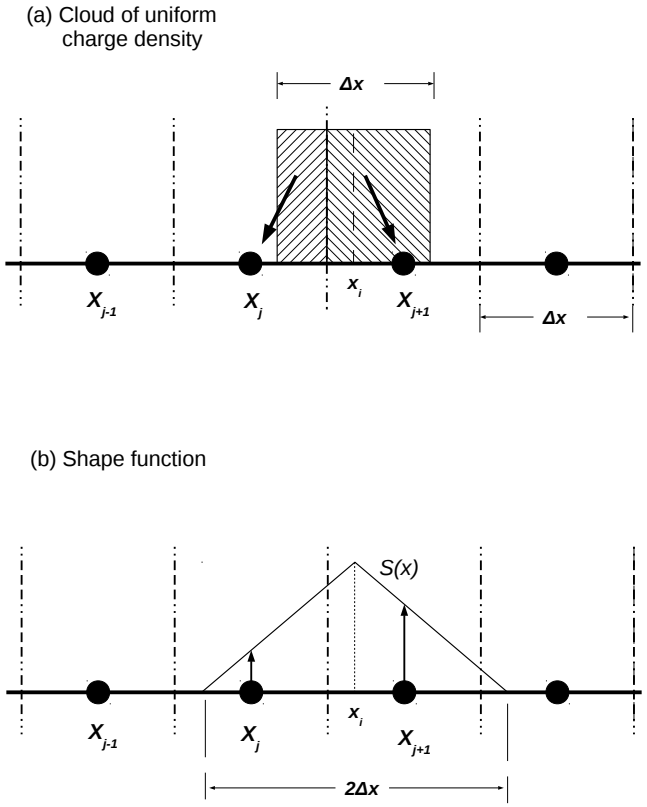

Figure 2.3: In the linear interpolation scheme, point particles take the form of (a) clouds of uniform charge density of width Δx. The charge assigned to a grid point is seen as the amount of the clouds charge density lying within the cell belonging to that grid point. Consequently, this scheme produces (b) an effective triangular shape function S(x) of width $2\Delta x$. The charge assigned to a grid point is thus proportional to the value of the shape function at the location of the grid point.

where μ_0 is the permeability of free space and c is the speed of light. For simplicity we set $\epsilon_0 = 1$ in our simulation code. Further justification for using $\epsilon_0 = 1$ is given in Appendix C, where the value $\epsilon_0 = 1$ arises as a result of using normalised parameters in our simulations.

We now write the variables E_x and ρ, at the grid point j, as $E_x(X_j)$ and $\rho(X_j)$, respectively. We then define, in accordance with the electrostatic approximation,

$$E_x(X_j) = -\frac{d\phi(X_j)}{dx}, \tag{2.18}$$

where $\phi(X_j)$ is a scalar potential. Substituting Equation (2.18) into Equation (2.17) yields

$$\frac{d^2\phi(X_j)}{dx^2} = -\frac{\rho(X_j)}{\epsilon_0}, \tag{2.19}$$

which is Poisson's equation in one dimension.

We employ periodic boundary conditions for the fields and particles in our simulation code and hence Poisson's equation is amenable to solution via Fourier techniques (Cooley and Turkey, 1965). In our simulation code we employ the fast Fourier transform which is based on the discrete Fourier transform. Our code utilises the Fastest Fourier Transform in the West (FFTW) library to compute the Fourier transforms in our simulation code. The FFTW library defines the discrete Fourier transform and inverse Fourier transform as

$$\begin{aligned} F(k) &= \sum_{n=0}^{N-1} f(n) e^{-2\pi i k n/N}, \\ f(n) &= \frac{1}{N} \sum_{k=0}^{N-1} F(k) e^{2\pi i k n/N}, \end{aligned}$$

where $f(n)$ is a function sampled at the discrete points $n\Delta$ and $F(k)$ is its Fourier transform. We now assume the real space grid quantities $E_x(X_j)$,

$\rho(X_j)$ and $\phi(X_j)$ have the Fourier transforms $E_x(k)$, $\rho(k)$ and $\phi(k)$, respectively. Thus the electric field can be calculated in Fourier space using the Fourier space equivalent of Equation (2.18) (Dawson, 1983; Birdsall and Langdon, 1985; Tajima, 1989)

$$E_x(k) = -ik\phi(k), \tag{2.20}$$

where

$$\phi(k) = \frac{\rho(k)}{\epsilon_0 k^2}. \tag{2.21}$$

To illustrate the method for solving Equations (2.20) and (2.21) using finite difference methods we first write the centred difference forms of Equations (2.18) and (2.19) as

$$E_x(X_j) = -\frac{\phi(X_{j+1}) - \phi(X_{j-1})}{2\Delta x}, \tag{2.22}$$

$$\frac{\phi(X_{j+1}) - 2\phi(X_j) + \phi(X_{j-1})}{(\Delta x)^2} = -\frac{\rho(X_j)}{\epsilon_0}. \tag{2.23}$$

We now write

$$X_{j+1} = X_j + \Delta x,$$

and assume all quantities in Equations (2.22) and (2.23) will vary in Fourier space as $\propto f(k)\exp(ikX_j)$, as suggested by Tajima (1989). Thus Equation (2.23) can be written in Fourier space as

$$\begin{aligned}
\frac{\phi(k)\exp[ik(X_j+\Delta x)] - 2\phi(k)\exp(ikX_j) + \phi(k)\exp[ik(X_j-\Delta x)]}{(\Delta x)^2} &= -\frac{\rho(k)\exp(ikX_j)}{\epsilon_0} \\
\phi(k)\exp(ikX_j)\left[\frac{\exp(ik\Delta x) - 2 + \exp(-ik\Delta x)}{(\Delta x)^2}\right] &= -\frac{\rho(k)\exp(ikX_j)}{\epsilon_0} \\
\phi(k)\left[\frac{\exp(ik\Delta x) - 2 + \exp(-ik\Delta x)}{(\Delta x)^2}\right] &= -\frac{\rho(k)}{\epsilon_0}.
\end{aligned} \tag{2.24}$$

Using the identity (Stewart, 2003)

$$\cos(\theta) = \frac{\exp(i\theta) + \exp(-i\theta)}{2},$$

Equation (2.24) can be written as

$$\begin{aligned} \phi(k)\left[\frac{-2 + 2\,\cos(k\Delta x)}{(\Delta x)^2}\right] &= -\frac{\rho(k)}{\epsilon_0} \\ -2\phi(k)\left[\frac{1 - \cos(k\Delta x)}{(\Delta x)^2}\right] &= -\frac{\rho(k)}{\epsilon_0}. \end{aligned} \tag{2.25}$$

Using the half angle formula (Stewart, 2003)

$$\sin^2(\theta) = \frac{1 - \cos(2\theta)}{2},$$

Equation (2.25) becomes

$$4\phi(k)\frac{\sin^2\left(\frac{k\Delta x}{2}\right)}{(\Delta x)^2} = \frac{\rho(k)}{\epsilon_0}. \tag{2.26}$$

Equation (2.26) can be written in the form given by Birdsall and Langdon (1985) and Tajima (1989) by defining

$$\begin{aligned} A^2 &= \frac{4\sin^2\left(\frac{k\Delta x}{2}\right)}{(\Delta x)^2} \\ &= k^2\left[\frac{\sin\left(\frac{k\Delta x}{2}\right)}{\frac{k\Delta x}{2}}\right]^2. \end{aligned} \tag{2.27}$$

Thus Equation (2.26) becomes

$$\phi(k) = \frac{\rho(k)}{\epsilon_0 A^2}. \tag{2.28}$$

Similarly, it can be shown that Equation (2.22) can be written as

$$E_x(k) = -i\alpha\phi(k), \tag{2.29}$$

where we have defined

$$\alpha = k\left[\frac{\sin(k\Delta x)}{k\Delta x}\right]. \tag{2.30}$$

Equations (2.28) and (2.29) are used to calculate the electric field, in Fourier space, in our simulation code. In comparing Equations (2.20) and (2.21) to Equations (2.28) and (2.29), the variables A^2 and α can be seen to represent the centred difference form of the gradient operator in Fourier space (Birdsall and Langdon, 1985; Tajima, 1989).

2.4 Integrating the equations of motion

At every time step in the simulation, the equations of motion governing the dynamics of the particles are integrated in time. The position x_i and velocity $\boldsymbol{v}_i$ of particle i are then updated (Dawson, 1983; Matsumoto and Omura, 1984; Birdsall and Langdon, 1985; Tajima, 1989). Newton's equations are used to model the dynamics of the particles which, in the one-and-two-halves dimensional simulation problem, are given by

$$\frac{d\boldsymbol{v}_i}{dt} = \frac{\boldsymbol{F}_i}{m_i}, \tag{2.31}$$

$$\frac{dx_i}{dt} = v_{xi}, \tag{2.32}$$

where the force $\boldsymbol{F}_i$ in Equation (2.31) on particle i is provided by the electrostatic fields $\boldsymbol{E}(x_i, t)$ and $\boldsymbol{B}_0$, and is calculated using the Lorentz force equation

$$\boldsymbol{F}_i = q_i\left[\boldsymbol{E}(x_i, t) + \boldsymbol{v}_i \times \boldsymbol{B}_0\right], \tag{2.33}$$

where $\boldsymbol{B}_0$ is the constant magnetic field and $\boldsymbol{E}(x_i, t)$ is the electric field at the position of particle i, at time t. The coupled set of differential equations, Equations (2.31) to (2.33), are numerically solved in the simulation using finite difference techniques, which will be described in the subsequent subsections

2.4.1 Updating the particle velocities

To update the particle velocities in our simulation we use the Boris method (Boris, 1970), which evaluates Equations (2.31) and (2.33) in finite difference form. The Boris method (Boris, 1970) is time centred and second order accurate and involves the decoupling of the electric force component and the magnetic force component in Equations (2.31) and (2.33) (Birdsall and Langdon, 1985; Sydora, 1999; Omura, 2007).

The method for solving Equations (2.31) and (2.33) in finite difference form using the Boris method is done as follows. First, using the superscript n to denote the time step $n\Delta t$, we introduce the notation

$$\begin{aligned} \boldsymbol{v}^{n+1/2} &= \boldsymbol{v}((n+1/2)\Delta t), \\ \boldsymbol{E}^{n} &= \boldsymbol{E}(x_i, n\Delta t), \\ \boldsymbol{B}_0^{n} &= \boldsymbol{B}_0(x_i, n\Delta t). \end{aligned}$$

The centred difference form of Equations (2.31) and (2.33) is given by

$$\frac{\boldsymbol{v}^{n+1/2} - \boldsymbol{v}^{n-1/2}}{\Delta t} = \frac{q}{m}\left[\boldsymbol{E}^n + \frac{\boldsymbol{v}^{n+1/2} + \boldsymbol{v}^{n-1/2}}{2} \times \boldsymbol{B}_0^n\right], \tag{2.34}$$

where $\boldsymbol{v}^n$ has been approximated by $(\boldsymbol{v}^{n+1/2} + \boldsymbol{v}^{n-1/2})/2$. Boris (1970) suggested separating the electric and magnetic forces in Equation (2.34) by defining the velocities $\boldsymbol{v}^-$ and $\boldsymbol{v}^+$ via

$$\boldsymbol{v}^{n-1/2} = \boldsymbol{v}^- - \frac{q\boldsymbol{E}^n}{m}\frac{\Delta t}{2}, \tag{2.35}$$

$$\boldsymbol{v}^{n+1/2} = \boldsymbol{v}^+ + \frac{q\boldsymbol{E}^n}{m}\frac{\Delta t}{2}. \tag{2.36}$$

Substituting Equations (2.35) and (2.36) into Equation (2.34) yields

$$\frac{\boldsymbol{v}^{+} - \boldsymbol{v}^{-}}{\Delta t} = \frac{q}{2m}\left(\boldsymbol{v}^{+} + \boldsymbol{v}^{-}\right) \times \boldsymbol{B}_0^n, \tag{2.37}$$

which contains no explicit mention of the electric field. Equations (2.35) and (2.36) and Equation (3.37) therefore decouple the electric and magnetic forces on the charged particle.

The terms containing the electric field, Equations (2.35) and (2.36), describe an acceleration of a charged particle by the electric field. On the other hand, Equation (2.37) describes a rotation of the momentum of a particle about an axis parallel to $\boldsymbol{B}_0$, through an angle of $\varphi = -2\,\tan^{-1}(qB_0\Delta t/2m)$ (Birdsall and Langdon, 1985; Sydora, 1999).

The Boris method can thus be seen as defining a three step procedure to solve Equation (2.34), for $\boldsymbol{v}^{n+1/2}$, using Equations (2.35) to (2.37), and hence update a particle's velocity. These steps are as follows:

1. A particle with velocity $\boldsymbol{v}^{n-1/2}$ is initially accelerated by the electric field $\boldsymbol{E}^n$ for half of the time step, $\Delta t/2$, and a new velocity, $\boldsymbol{v}^{-}$, is obtained using Equation (2.35), i.e., $\boldsymbol{v}^{n-1/2} \rightarrow \boldsymbol{v}^{-}$.

2. The rotation of the new particle velocity, $\boldsymbol{v}^{-}$, by the magnetic field is then calculated using Equation (2.37) for the full time step, Δt, i.e., $\boldsymbol{v}^{-} \rightarrow \boldsymbol{v}^{+}$.

3. Finally the particle is accelerated for another half of the time step using Equation (2.36) and the updated particle velocity is obtained, i.e., $\boldsymbol{v}^{+} \rightarrow \boldsymbol{v}^{n+1/2}$.

To accomplish this sequence of events, specifically to evaluate Equation (2.37), Boris (1970) described a two step method to solve Equation (2.37) for $\boldsymbol{v}^{+}$, using the equations

$$\boldsymbol{v}^{'} = \boldsymbol{v}^{-} + \boldsymbol{v}^{-} \times \boldsymbol{t}, \tag{2.38}$$

$$\boldsymbol{v}^{+} = \boldsymbol{v}^{-} + \boldsymbol{v}^{'} \times \boldsymbol{s}, \tag{2.39}$$

where $\boldsymbol{v}'$ is an intermediate velocity and $\boldsymbol{t}$ and $\boldsymbol{s}$ are respectively given by

$$\boldsymbol{t} = \frac{q\boldsymbol{B}_0^n \Delta t}{2m}, \qquad \text{and} \qquad \boldsymbol{s} = \frac{2\boldsymbol{t}}{(1+t^2)}.$$

As stated before, the magnetic field provides purely a rotation of the velocity vector, from $\boldsymbol{v}^-$ to $\boldsymbol{v}^+$, through an angle specified by $\varphi = -2\ \tan^{-1}(qB_0\Delta t/2m)$ (Sydora, 1999). Thus, the magnitude of the vector should remain unchanged during the rotation defined by Equation (2.37) [or Equations (2.38) and (2.39)]. The parameter $\boldsymbol{s}$ in Equation (2.39) is a scaled version of $\boldsymbol{t}$ (defined above), which is scaled to satisfy the requirement that the magnitudes of $\boldsymbol{v}^-$ and $\boldsymbol{v}^+$ are equal (Birdsall and Langdon, 1985, p. 62). With $\boldsymbol{v}^+$ obtained using Equations (2.38) and (2.39) the updated particle velocity $\boldsymbol{v}^{n+1/2}$ is readily obtained via Equation (2.36). We provide a derivation of the Equations (2.38) and (2.39) in Appendix D.

2.4.2 Updating the particle positions

The standard leapfrog technique is used to update the position of a particle using the velocity of the particle. The leapfrog technique provides a method to numerically integrate Equation (2.32) in time, which is both second order accurate (Hockney and Eastwood, 1981, p. 97) and is as computationally intensive as the first order Euler method (Birdsall and Langdon, 1985, p. 12). Thus, to update the particle positions we use

$$\begin{aligned} \frac{x^{n+1} - x^n}{\Delta t} &= v^{n+1/2} \\ x^{n+1} &= x^n + v_x^{n+1/2}\Delta t \end{aligned} \tag{2.40}$$

2.5 The stability of the numerical techniques

Due to the discretisation of space and time in particle-in-cell simulations as well as the numerical techniques employed to solve the differential equations, numerical artefacts can arise that affect numerical accuracy and stability of the simulation. Unphysical instabilities generally arise due to temporal or

spatial aliasing of the plasma dynamics owing to improper choices of the time step Δt and the cell sizes Δx (Dawson, 1983; Forslund, 1985). Round-off errors, arising due to the finite word-length of numbers stored in a computer are usually not a major source of error in particle-in-cell simulations and can usually be made negligible (Hockney and Eastwood, 1981).

2.5.1 Choice of the cell size

Birdsall and Langdon (1985, ch. 8) analysed in detail the finite grid instability which is a numeric effect arising due to the aliasing of Fourier modes in the simulation. The particle interpolation scheme used in the simulation was found to contribute to the aliasing, where the higher order cloud-in-cell scheme (or first order linear interpolation scheme) was found to reduce this aliasing effect, when compared to using the nearest-grid-point scheme. For the linear interpolation scheme, the growth rate of the finite grid instability was found to be made negligible by restricting the cell size Δx by (Birdsall and Langdon, 1985; Lapenta, 2012)

$$\Delta x < \pi \lambda_{De}, \tag{2.41}$$

where $\lambda_{De} = (\epsilon_0 T_e / n_{0e} e^2)^{1/2}$ is the electron Debye length. The cell size Δx used in our simulations are defined to strictly adhere to this stability condition, Equation (2.41).

2.5.2 Choice of the time step

To illustrate the stability of the leapfrog scheme, Equation (2.40), we follow Birdsall and Langdon (1985) and Verboncoeur (2005) and analyse it using simple harmonic motion as model paradigm. The equation governing the dynamics of a one dimensional simple harmonic oscillator is

$$\frac{d^2 x}{dt^2} = -\omega_0^2 x, \tag{2.42}$$

where x is the displacement of the oscillator from its equilibrium position and ω_0 is the natural frequency of the system. With $x^n \equiv x(n\Delta t)$, the centred difference approximation to Equation (2.42) is given by

$$\frac{x^{n+1} - 2x^n + x^{n-1}}{(\Delta t)^2} = -\omega_0^2 x^n. \tag{2.43}$$

Assuming solutions of the form

$$x^n = Ae^{-i\omega n\Delta t}, \tag{2.44}$$

where ω is an angular frequency, to be determined, and A is an amplitude, Equation (2.43) yields

$$\begin{aligned} \frac{Ae^{-i\omega(n+1)\Delta t} - 2Ae^{-i\omega n\Delta t} + Ae^{-i\omega(n-1)\Delta t}}{\Delta t^2} &= -\omega_0^2 Ae^{-i\omega n\Delta t} \\ \frac{e^{-i\omega\Delta t} - 2 + e^{+i\omega\Delta t}}{\Delta t^2} &= -\omega_0^2. \end{aligned} \tag{2.45}$$

Using the identity (Stewart, 2003)

$$\cos(\theta) = \frac{\exp(i\theta) + \exp(-i\theta)}{2},$$

Equation (2.45) becomes

$$\begin{aligned} \frac{-2 + 2\cos(\omega\Delta t)}{\Delta t^2} &= -\omega_0^2 \\ 1 - \cos(\omega\Delta t) &= \frac{\omega_0^2\Delta t^2}{2}. \end{aligned} \tag{2.46}$$

Using the half angle formula (Stewart, 2003)

$$\sin^2(\theta) = \frac{1 - \cos(2\theta)}{2},$$

Equation (2.46) becomes

$$\begin{aligned} 2\sin^2\left(\frac{\omega\Delta t}{2}\right) &= \frac{\omega_0^2\Delta t^2}{2} \\ \sin\left(\frac{\omega\Delta t}{2}\right) &= \pm\frac{\omega_0\Delta t}{2} \\ \frac{\omega\Delta t}{2} &= \pm\sin^{-1}\left(\frac{\omega_0\Delta t}{2}\right), \end{aligned} \tag{2.47}$$

where $\sin^{-1}(x)$ in Equation (2.47) can be evaluated, for $x^2 < 1$, using (Gradshteyn and Ryzhik, 2007)

$$\sin^{-1}(x) = x + \frac{1}{2\cdot 3}x^3 + \frac{1\cdot 3}{2\cdot 4\cdot 5}x^5 + ..., \tag{2.48}$$

Thus Equation (2.47) becomes,

$$\frac{\omega\Delta t}{2} = \pm\left[\frac{\omega_0\Delta t}{2} + \frac{1}{6}\left(\frac{\omega_0\Delta t}{2}\right)^3 + \frac{3}{40}\left(\frac{\omega_0\Delta t}{2}\right)^5 + ...\right], \tag{2.49}$$

Clearly if $\left|\frac{\omega_0\Delta t}{2}\right| \ll 1$ we can truncate the series, yielding

$$\begin{aligned} \frac{\omega\Delta t}{2} &\simeq \pm\frac{\omega_0\Delta t}{2} \\ \omega &\simeq \pm\omega_0. \end{aligned} \tag{2.50}$$

In this case ω is purely real and $\omega \simeq \pm\omega_0$, as desired. However if $\frac{\omega_0\Delta t}{2} > 1$, then Equation (2.47) clearly predicts complex values of ω. In that case Equation (2.44) will be either growing or decaying exponentially with time, a feature inconsistent with the original simple harmonic model. This is indicative of numerical instability.

Based on the above simplified analysis we infer that for the leapfrog scheme to be stable we require

$$\omega_p\Delta t < 2, \tag{2.51}$$

where ω_p is the highest natural frequency of the plasma (Hockney and Eastwood, 1981; Birdsall and Langdon, 1985). In practice

$$\omega_p \Delta t \leq 0.5 \tag{2.52}$$

is commonly used for reasonable accuracy and stability (Hockney and Eastwood, 1981; Winske and Omidi, 1996). We use a time step Δt in our simulations which is defined to strictly adhere to the stability condition Equation (2.52).

When incorporating electromagnetic fields a further restriction on the time step must be made to maintain stability and accuracy. While not a consideration for the simulation described in this thesis, we nevertheless briefly point out the source of this instability for completeness. This restriction is demonstrated by looking at plane electromagnetic waves propagating in a vacuum (Birdsall and Langdon, 1985; Sydora, 1999). Using Maxwell's equations, the temporal evolution of the transverse component of electromagnetic fields in Fourier space is given, in cgs-units, as (Sydora, 1999)

$$\frac{\partial \boldsymbol{E}_T(\boldsymbol{k},t)}{\partial t} = ic\boldsymbol{k} \times \boldsymbol{B}_T(\boldsymbol{k},t) - 4\pi \boldsymbol{J}_T(\boldsymbol{k},t), \tag{2.53}$$

$$\frac{\partial \boldsymbol{B}_T(\boldsymbol{k},t)}{\partial t} = -ic\boldsymbol{k} \times \boldsymbol{E}_T(\boldsymbol{k},t), \tag{2.54}$$

where the subscript T denotes transverse components. For the vacuum case, $\boldsymbol{J}_T = 0$, the longitudinal component of the electric field $\boldsymbol{E}_L$ is found by solving Poisson's equation and there is no longitudinal component of $\boldsymbol{B}$ due to $\nabla \cdot \boldsymbol{B} = 0$. Equations (2.53) and (2.54) are numerically solved by staggering $\boldsymbol{B}_T$ and $\boldsymbol{E}_T$ in time. Evaluating $\boldsymbol{B}_T$ at times $(n-1/2)\Delta t$ and evaluating $\boldsymbol{E}_T$ at times $n\Delta t$, the time centred finite difference form of Equations (2.53) and (2.54) are given by (Sydora, 1999)

$$\boldsymbol{E}_T^{n+1}(\boldsymbol{k}) = \boldsymbol{E}_T^{n}(\boldsymbol{k}) + ic\Delta t\boldsymbol{k} \times \boldsymbol{B}_T^{n+1/2}(\boldsymbol{k}), \tag{2.55}$$

$$\boldsymbol{B}_T^{n+1/2}(\boldsymbol{k}) = \boldsymbol{B}_T^{n-1/2}(\boldsymbol{k}) - ic\Delta t\boldsymbol{k} \times \boldsymbol{E}_T^{n}(\boldsymbol{k}), \tag{2.56}$$

where we have used

$$\begin{aligned} \boldsymbol{E}_T^n(\boldsymbol{k}) &= \boldsymbol{E}_T(\boldsymbol{k}, n\Delta t), \\ \boldsymbol{B}_T^{n+1/2}(\boldsymbol{k}) &= \boldsymbol{B}_T(\boldsymbol{k}, (n+1/2)\Delta t). \end{aligned}$$

Assuming the fields in Equations (2.55) and (2.56) have the form

$$\boldsymbol{E}_T^n(\boldsymbol{k}) = \boldsymbol{E}_0(\boldsymbol{k}) e^{-i\omega n\Delta t}, \tag{2.57}$$

$$\boldsymbol{B}_T^{n+1/2}(\boldsymbol{k}) = \boldsymbol{B}_0(\boldsymbol{k}) e^{-i\omega (n-1/2)\Delta t}, \tag{2.58}$$

and substituting the field Equations (2.57) to (2.58) into the finite difference Equations (2.55) and (2.56) yields (Sydora, 1999)

$$c^2 k^2 = \frac{\sin^2(\omega \Delta t/2)}{(\Delta t/2)^2}, \tag{2.59}$$

where $k = ||\boldsymbol{k}||$. Equation (2.59) is only satisfied for real ω if (Dawson, 1983; Sydora, 1999)

$$ck\Delta t < 2. \tag{2.60}$$

The inequality in Equation (2.60) is known as the Courant-Friedrichs-Levy (CFL) condition, and the violation of this inequality will produce numerical instability. Equation (2.60) is equivalent to the condition that the time step be small enough to resolve the smallest photon oscillation period (Sydora, 1999).

2.6 Parallelisation of the simulation code

Simulating a plasma with millions of individual charged particles has the drawback of being computationally expensive and can make large scale simulations unfeasible (Dawson et al., 1993). This problem has been somewhat reduced by the advent and ready availability of high performance computing and parallel computing environments. Distributed memory systems, such as that provided by the Centre for High Performance Computing (CHPC) in

South Africa, may be used to run large scale simulations in a parallel environment.

Message Passing Interface (MPI) was utilised to parallelise our simulation code using the particle decomposition technique of PIC parallelisation (Liewer et al., 1988; Dawson et al., 1993; Martino et al., 2001; Qiang and Xiaoye, 2010). The use of Message Passing Interface allowed our simulation code to run on distributed memory systems.

In the particle decomposition technique, the particle data is distributed among the available processors and all other quantities, such as those associated with the fields (typically the state vector), are replicated on each processor. Particle calculations, such as particle position and velocity updating as well as charge deposition onto the grid, are carried out in parallel, independently on each processor, using only the particles assigned to that processor. Inter-processor communication, however, is required at each time step to add the charge density grids from all processors so that the global electric field can be calculated for the entire plasma, i.e., after each processor accumulates a charge density on its allocated local grid, a global operation is performed in the simulation to combine all the charge density grids from each processor, forming the global charge density. Once the global charge density grid is formed, the global electric field is calculated from this, using the methods described in Section 2.3 (p. 21). The global electric field then gets replicated on each processor and it is this global electric field which will be used to update the position and velocity of a particle, as described in Section 2.4 (p. 26).

This method works well in the one dimensional electrostatic case considered here as the particle calculations are more computationally expensive than the field calculations. Thus, field calculation parallelisation is not needed and load balancing algorithms are not required, as processor loads remain balanced due to an equal number of particles being assigned to each processor.

An obstacle we encountered in our simulations when using the particle decomposition scheme, occurred when particle diagnostics needed to be printed. We assigned only one processor to carry out diagnostics using data gathered from all the processors. When computationally demanding particle diagnostics needed to be carried out, the simulation is briefly halted until the processor in charge of gathering the distributed data and printing out the diagnostic has completed its execution. Only then can the global op-

eration, which accumulates the charge density from each grid (as described previously), be performed.

The phase space configuration plots for the plasma particles, which are exported in image format at regular intervals and combined into a movie clip at the end of the simulation, were found to be the most computationally intensive and thus was the biggest obstacle to parallelism. Here computation times for the phase space plots increased with the number of particles being simulated. The incorporation of phase space plots drastically increased the simulation time and was therefore only used occasionally to view the plasma dynamics.

To improve on the parallel efficiency and decrease simulation run times when phase space plots were needed, the Manager-Workers pattern (Ortega-Arjona, 2004) for parallel programming was implemented. The Manager-Workers pattern is a variant of the Master-Slave pattern (Buschmann et al., 1996) and uses the activity parallelism approach, where activities carried out by the processors are grouped and the activities are run in parallel. The Manager-Workers pattern is generally considered as a basic organisation of tasks for parallel computation (Mani et al., 1992; Kleiman et al., 1996).

The Manager-Workers pattern divides the N available processors into a single Manager processor and a group of independent, identical Worker processors. The tasks of the manager and workers in our PIC simulation are as follows:

- **Manager**: The responsibilities of the manager processor (usually processor 0) are to read in the input file, initialise the simulation parameters and to split the particle data evenly among the workers. The manager is also responsible for carrying out all diagnostics using the relevant data provided by the worker processors, at specified time intervals.

- **Workers**: The responsibilities of the worker processors (processors 1 $\rightarrow N-1$) are to carry out all the particle and field calculations. The particle decomposition scheme described above is effectively carried out among the workers only. Diagnostic data such as the particle state vector is sent to the Manager processor, at specified times, for diagnostics to be carried out.

The benefit of this method is that continual computation of particle and field data is achieved concurrently with diagnostic output. The Manager-Workers pattern works best when computation times for the Manager activities and the Worker activities are balanced, i.e., new diagnostic data is sent to the manager as soon as the previous diagnostic has been carried out. Preliminary results from the implementation of the Manager-Workers pattern with the particle decomposition technique showed a decrease in the simulation run times, when compared to using only the particle decomposition technique.

Chapter 3

Simulation of the ion-acoustic instability

As an initial case study, to test the one dimensional particle-in-cell simulation code developed and reported on in this thesis, the current-driven ion-acoustic instability was investigated for an electron-ion plasma. Two simulations of the ion-acoustic instability were run. In the first, the velocity distributions of the plasma ions and electrons were modelled by Maxwellian distributions. In the second, the velocity distributions of the plasma ions and electrons were modelled by kappa distributions with a low value of kappa, $\kappa = 2$.

The results of the simulations are presented in the subsequent sections, starting with the simulation for a plasma having a Maxwellian velocity distribution and followed by the simulation for a plasma having a kappa velocity distribution. The results of both simulations are compared and analysed using kinetic theory, and differences in the behaviour of the ion-acoustic instability for the two simulations are discussed.

3.1 Overview of ion-acoustic waves

As the name suggests, ion-acoustic waves propagate in an analogous manner to acoustic waves in air, i.e., they are dispersionless longitudinal waves.

Contrary to acoustic wave propagation in air, however, the ions in the plasma transmit vibrations to each other through the intermediary of an electric field. The ions provide the inertia for the wave, which is thus a low frequency wave, on the order of the ion plasma frequency ω_{pi} (Chen, 2006, pp. 95-99). On the other hand, the electrons, due to their higher mobility, are able to move to screen out electrostatic potentials formed by the bunching of the ions in the plasma at small wavenumbers $k\lambda_{De} \ll 1$. As a result, the collective mode of the ions is described by the screened plasma frequency (Ichimaru, 1973, p. 72)

$$\omega^2 = \frac{\omega_{pi}^2}{1 + 1/k^2\lambda_{De}^2}, \tag{3.1}$$

where $\omega_{pi} = (n_{0i}e^2/\epsilon_0 m_i)^{1/2}$ is the ion plasma frequency for singly charged ions, k is the wavenumber and $\lambda_{De} = (\epsilon_0 T_e/n_{0e}e^2)^{1/2}$ is the electron Debye length. However, at larger wavenumbers, i.e., where $k\lambda_{De} \gg 1$, the screening is less effective and the ion oscillations are effectively un-shielded (Ichimaru, 1973; Chen, 2006), as can be seen by Equation (3.1), which reduces to $\omega^2 \simeq \omega_{pi}^2$ in this limit.

The ion-acoustic wave can be driven unstable by electron currents or by ion beams flowing through the plasma and are thus observed in a number of space plasma environments where field aligned currents are present (Treumann and Baumjohann, 1997; Swanson, 2003).

Gurnett and Frank (1978), based on earlier work by Gurnett and Anderson (1977), used wavelength measurements provided by the Imp 6 spacecraft to interpret the occurrences of electric field turbulence in the solar wind at frequencies between the electron and ion plasma frequency. These were interpreted as short-wavelength ion-acoustic waves Doppler-shifted up in frequency by the motion of the solar wind.

Ion-acoustic waves occurring simultaneously with ion beams have been observed by ISEE-1 and ISEE-2 and have been associated with energetic particle streams coming from the Earth's bow shock (Anderson et al., 1981).

Cairns et al. (1995) interpreted the solitary structures, involving density depletion, observed in the upper ionosphere by the Freja satellite as ion-acoustic solitons. By showing that the structure of the ion-acoustic solitons were changed by the presence of non-thermal electrons, Cairns et al. (1995)

were able to ascertain the existence of solitary structures similar to those observed in the ionosphere by Freja.

Huba et al. (2000) reported on a model for the generation of ion-acoustic waves in the topside ionosphere. The model of Huba et al. (2000) suggests that waves are excited at sunrise, due to rapid photo-electron heating, producing plasma flow and ultimately ion-acoustic waves, and at sunset, due to rapid cooling of the lower ionosphere.

Satellites often observe plasma instabilities which have already evolved to a non-linear, turbulent state. Due to the analytical difficulties encountered in the study of the non-linear evolution of plasma instabilities, computer simulations have been effectively used to study the non-linear evolution of the ion-acoustic instability.

Dum et al. (1974) investigated ion-acoustic turbulence using particle-in-cell simulations. A constant electric field was applied to drive a current in the plasma and produce instability, which eventually evolved to a turbulent state. The simulations by Dum et al. (1974) illustrated that high energy ion tails were formed by ion-acoustic turbulence. A suggested mechanism for the production of the high energy ion tails was the non-resonant interaction between ions and the wave, bringing enough cold ions up to resonance with the wave. Dum et al. (1974) also suggested that linear Landau damping on the ion tail was sufficient to eventually quench the ion-acoustic instability. Appert and Vaclavik (1981) undertook a numerical investigation, using a one dimensional quasi-linear model, in an effort to reproduce the results of Dum et al. (1974). They confirmed the appearance of hot ions during current driven ion-acoustic turbulence; however, the quenching of the instability by the hot ions was not observed until a model which included two dimensional effects was used.

Sato and Okuda (1980) ran simulations of electron drift driven ion-acoustic double layers in a plasma where the initial electron drift velocity was less than the thermal velocity of the ions. Sato and Okuda (1980) were able to observe double layers, contrary to earlier work by DeGroot et al. (1977) which suggested that the electron drift velocity should exceed the ion thermal velocity for ion-acoustic double layers to occur. Sato and Okuda (1980), using a sufficiently long spatial system, found that no matter how small the anomalous resistivity caused by the ion-acoustic instability, the dc potential buildup associated with the localised resistivity becomes large enough to accelerate electrons. The accelerated electrons, in turn, enhance the original

instability and a new phase of the instability takes place.

Watt et al. (2002) used both a Vlasov simulation and a particle-in-cell simulation to investigate the resistivity due to the current-driven ion-acoustic instability. The simulations of Watt et al. (2002) used ions and electrons with similar temperatures, appropriate for the magnetopause and low-latitude boundary layer. The results from both the Vlasov and PIC simulations gave values for resistivity which were orders of magnitude greater than earlier analytical estimates given by Labelle and Treumann (1988) for the magnetopause. Watt et al. (2002) deduced that the discrepancy in the results from simulation and those from analytical studies arose due to analysis assuming weak non-linearity, i.e., assuming there is little deviation of the distribution from the Maxwellian, as well as due to the assumption $T_e \gg T_i$. That the former assumption is violated could be inferred from the simulation results, which clearly showed the formation of a plateau in the electron velocity distribution. Watt et al. (2002) suggested a revision of the analytical method to adequately account for wave-particle interactions.

In the simulations carried out by the above authors, as well as many other plasma simulations not reported on here, the velocity distributions of the space plasma species are modelled by the Maxwellian distribution. This, despite the fact that non-Maxwellian plasmas are often observed in space, e.g., see Christon et al. (1988), Christon et al. (1989), Maksimovic et al. (1997), Leubner (2004) and Pierrard and Lazar (2010), to name a few. Presented below is an investigation and comparison of the behaviour of the ion-acoustic instability when the plasma velocity distribution is modelled by (1) a Maxwellian distribution and (2) a kappa distribution.

3.2 Dispersion relation for the ion-acoustic wave

3.2.1 Maxwellian case

The well known dispersion relation for the ion-acoustic wave, in an electron-ion plasma where both species have a Maxwellian velocity distribution, is given by (Chen, 2006, p. 98)

$$\omega^2 = k^2 \left(\frac{T_e}{m_i} \frac{1}{1 + k^2 \lambda_{De}^2} + 3 \frac{T_i}{m_i} \right), \tag{3.2}$$

where T_e and T_i are the temperatures for the electron and ion species, respectively, m_e and m_i are the masses of an electron and an ion, respectively, and λ_{De} is the electron Debye length. We have set $\gamma = 3$ for the ion fluid, corresponding to one dimensional compression, as suggested by kinetic theory. Equation (3.2) is a more general version of Equation (3.1), presented earlier, which takes into account finite ion temperature. At small wavenumbers, $k\lambda_{De} \ll 1$, Equation (3.2) reduces to

$$\frac{\omega^2}{k^2} = \frac{T_e}{m_i} + \frac{3T_i}{m_i},$$

where the ion-acoustic speed v_s is defined by

$$v_s = \left(\frac{T_e}{m_i} + \frac{3T_i}{m_i} \right)^{1/2}. \tag{3.3}$$

Since $T_i \ll T_e$ is a requirement for the weakly-damped ion-acoustic wave, which is the case we shall be considering here, the T_i term is usually neglected in the definition of the ion-acoustic speed, Equation (3.3), giving

$$v_s = \left(\frac{T_e}{m_i} \right)^{1/2}. \tag{3.4}$$

Thus Equation (3.2) can often be written in the simplified alternate form, neglecting the T_i term

$$\omega^2 = \frac{k^2 v_s^2}{1 + k^2 \lambda_{De}^2}. \tag{3.5}$$

By dividing the numerator and the denominator by $k^2\lambda_{De}^2$ it is easily seen that Equation (3.5) is equivalent to Equation (3.1) presented earlier.

3.2.2 Kappa case

For an electron-ion plasma where both species have a kappa velocity distribution, the dispersion relation for the ion-acoustic wave is given by (Meng et al., 1992; Mace et al., 1998)

$$\omega^2 = \frac{\omega_{pi}^2}{1 + 1/k^2\lambda_{\kappa e}^2}, \tag{3.6}$$

where

$$\lambda_{\kappa e} = \left[\left(\frac{\kappa_e - 3/2}{\kappa_e - 1/2}\right)\frac{\epsilon_0 T_e}{n_{0e}e^2}\right]^{1/2}, \tag{3.7}$$

is the Debye length for electrons having a kappa velocity distribution (Bryant, 1996; Mace et al., 1998) and κ_e is the kappa index for the electron species. Equation (3.6) can be written in the alternative form as

$$\omega^2 = \frac{k^2\lambda_{\kappa e}^2\omega_{pi}^2}{1 + k^2\lambda_{\kappa e}^2} = \frac{k^2(v_s^\kappa)^2}{1 + k^2\lambda_{\kappa e}^2}, \tag{3.8}$$

where the ion-acoustic speed in a plasma having a kappa velocity distribution is defined by

$$v_s^\kappa = \left[\left(\frac{\kappa_e - 3/2}{\kappa_e - 1/2}\right)\frac{T_e}{m_i}\right]^{1/2}. \tag{3.9}$$

Equation (3.8) for a kappa plasma is of the same form as Equation (3.5) for a Maxwellian plasma. Indeed, the plasma dynamics of the ion-acoustic wave in a kappa plasma are identical to that of a Maxwellian one, except for the modified shielding length which arises in the kappa plasma (Meng et al., 1992; Mace et al., 1998). Note that, in general the ion sound speed in the kappa plasma, Equation (3.9), will be different to Equation (3.4) for a Maxwellian plasma. However, it is seen that as $\kappa_e \to \infty$, Equation (3.7) reduces to the usual Debye length for electrons and Equation (3.9) reduces to Equation (3.4).

3.3 PIC simulation for a Maxwellian plasma

3.3.1 Simulation run parameters

In the first of two simulations of the ion-acoustic instability, the initial state of each plasma species is modelled by a drifting Maxwellian velocity distribution, using the particle loader described in Section 2.1.1 (p. 14). All particle positions are loaded uniformly throughout the simulation box.

In our simulation, all parameters are given with reference to those of the electron species. Times are measured in terms of the reciprocal of the electron plasma frequency and lengths are measured in terms of the electron Debye length, i.e., $t' = \omega_{pe}t$ and $x' = x/\lambda_{De}$, where primed variables are the simulation parameters and unprimed values denote ordinary S.I. values, see Appendix C. Consequently, velocities in our simulation are measured in terms of the electron thermal velocity $v_{the} = \omega_{pe}\lambda_{De}$, i.e., $v' = v/v_{the}$.

For this study we have opted to use a reduced ion-to-electron mass ratio of $m_i/m_e = 100$. This value allows one to fully resolve both plasma species' dynamics without resorting to unnecessarily long simulation run times (Hockney and Eastwood, 1981; Dawson, 1983; Birdsall and Langdon, 1985). Qualitatively similar behaviour of the ion-acoustic instability is, however, expected when a realistic ion-to-electron mass ratio is used (Biskamp and Chodura, 1971; Okuda and Ashour-Abdulla, 1988).

In our simulation, no external fields are applied to the plasma. The ion-acoustic instability is excited by creating an initial state where the hot electrons drift through a background of stationary cool ions. The temperature ratio between the electrons and ions was set to $T_e/T_i = 100$ to reduce ion Landau damping. Detailed theoretical kinetic studies show that the ion-acoustic wave can be destabilised when the electrons have a drift speed v_d in excess of the ion-acoustic speed v_s (or v_s^κ for a kappa plasma) (Krall and Trivelpiece, 1973; Treumann and Baumjohann, 1997). Thus, in our simulation run for the ion-acoustic instability, we use a supersonic electron drift. With our choice of parameters, the ion-acoustic speed, Equation (3.4), is $v_s = 0.1v_{the}$. The chosen drift velocity for the electron species was $v_d = 6v_s = 0.6v_{the}$. This choice of electron drift allows the ion-acoustic speed to coincide with the positive slope of the electron velocity distribution and thus the ion-acoustic wave is unstable (Meng et al., 1992; Treumann and Baumjohann, 1997; Chen, 2006). It also produces a growth rate sufficiently

Electron species	Ion species
9437184 particles	9437184 particles
$\omega_{pe} = 1$	$\omega_{pi} = 0.1$
$q/m_e = -1$	$q/m_i = 0.01$
$v_{the} = 1$	$v_{thi} = 0.01$
$v_{drift} = 0.6$	$v_{drift} = 0$

Table 3.1: The species parameters for the simulation of the ion-acoustic instability.

high that the nonlinear phase of the instability can be observed without the need for an unusually large number of time steps. A summary of the species parameters used in the simulation run is given in Table 3.1.

The simulation run used a box length of $L = 512\lambda_{De}$ with a cell size of $\Delta x = 0.25\lambda_{De}$, corresponding to a total of 2048 cells. The evolution of the simulation run was tracked to $\omega_{pe}t = 5000$, using a time step Δt satisfying $\omega_{pe}\Delta t = 0.1$. Periodic boundary conditions were used for both fields and particles.

3.3.2 Results of the simulation run

Figures 3.1 (a) and (b) compare (in green) the initial velocity distributions obtained for the electron and ion species, respectively, via our numerical loading algorithm [Section 2.1.1 (p. 14)], with the Maxwellian distribution, Equation (2.1), using our simulation run parameters, which is superimposed in black. The numerical approximation to the velocity distribution is obtained from each discrete plasma species using the method of "particle binning" described in Appendix E. Figures 3.1 (a) and (b) demonstrate very good agreement between the loaded velocity distributions of the plasma species and the Maxwellian distribution defined by Equation (2.1), which confirms the correctness of our particle loading algorithm.

An important check on the validity of the simulation run results is the conservation of total energy (Hockney and Eastwood, 1981; Dawson, 1983; Birdsall and Langdon, 1985; Forslund, 1985). In our simulation of the ion-acoustic instability, the plasma system is isolated from any external forces and periodic boundary conditions were used; thus, the total energy in the system should remain constant.

(a)

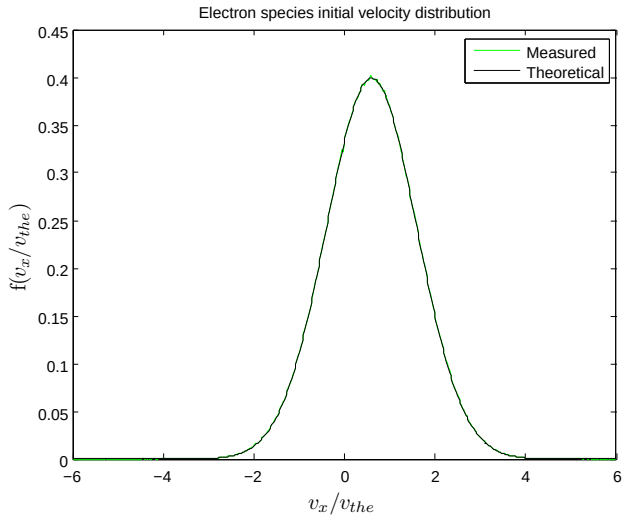

(b)

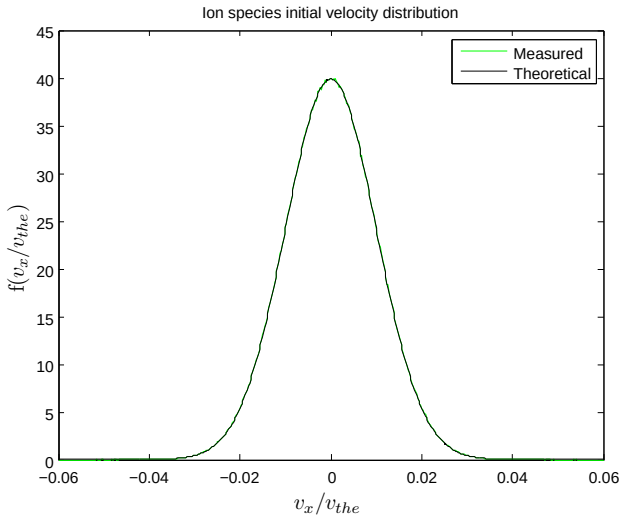

Figure 3.1: The measured initial velocity distribution (in green) for (a) the electron species and (b) the ion species along with the drifting Maxwellian distribution, Equation (2.1) (in black), for the parameters listed in Table 3.1. The agreement between the measured velocity distributions and the drifting Maxwellian for both the electron and ion species confirms the correctness of our particle loading.

Figure 3.2 illustrates the time evolution of the electric field energy E_f/T_e [Figure 3.2 (a)], the kinetic energy of the electron species E_e/T_e [Figure 3.2 (b)], the kinetic energy of the ion species E_i/T_e [Figure 3.2 (c)] and the total energy E_{tot}/T_e in the plasma [Figure 3.2 (d)], all expressed in terms of the initial thermal energy of the electrons. It is observed that, indeed, the total energy does remain approximately constant throughout the simulation, as seen in Figure 3.2 (d), to within the errors of the simulation techniques and fluctuations arising due to using discrete particles. This gives us a high degree of confidence in the validity of our results for this simulation.

Inspection of the electric field energy shown in Figure 3.2 (a), and the kinetic energies of the electron and ion species, Figures 3.2 (b) and (c), respectively, suggests that the ion-acoustic instability evolves in three phases, which we shall elaborate on below. That the waves observed in the simulation are of the ion-acoustic type will be verified through analysis of the electric field intensity spectra, which will be presented later in Figure 3.6.

In the first phase, seen on the interval $0 < \omega_{pe}t < 1230$ in Figure 3.2, the electric field energy, in Figure 3.2 (a), increases exponentially in time. This corresponds to exponential growth of the ion-acoustic wave out of the background of random thermal fluctuations (Treumann and Baumjohann, 1997; Crumley et al., 2001), to a level equivalent to the initial electron thermal energy T_e. The excited ion-acoustic waves gain energy and grow through the process of inverse Landau damping of the electron species (Treumann and Baumjohann, 1997), i.e., electrons with velocities close to the ion-acoustic phase speed are able to resonantly interact with the ion-acoustic wave, feeding energy into it, which will be shown later. As a result, during the wave growth phase there is a corresponding exponential decrease in the energy of the electron species, as seen in Figure 3.2 (b) on the interval $0 < \omega_{pe}t < 1230$. The ion species is observed to be accelerated by the growing wave and thus there is a gain in the kinetic energy of the ion species, as seen in Figure 3.2 (c) on the interval $0 < \omega_{pe}t < 1230$. Towards the end of this phase, signs of ion trapping are evident, signalling the onset of significant nonlinear effects, which will be discussed later.

In the second phase, defined on the interval $1230 < \omega_{pe}t < 1700$ in Figure 3.2, the instability is saturated through the depletion of the free energy source (Hellinger et al., 2004). The beginning of this phase is marked by the point, $\omega_{pe}t \approx 1230$, at which the electric field energy ceases to grow. Immediately after this the electric field energy exhibits a decreasing trend

which ends at $\omega_{pe}t \approx 1700$. During the interval $1230 < \omega_{pe}t < 1700$, the kinetic energies of the ions and electrons and the electric field energy are redistributed. This occurs prior to the onset of a quasi-equilibrium state, phase 3, discussed below.

Finally, in the third phase, at times $\omega_{pe}t > 1700$ in Figure 3.2, the system settles into a quasi-equilibrium state, marked by relative constancy of the individual energies. The electric field energy, Figure 3.2 (a), as well as the kinetic energies of the electron and ion species, Figures 3.2 (b) and (c), respectively, remain approximately constant during this phase. The small fluctuations observed in the energies, at time $\omega_{pe}t > 1700$ in Figures 3.2 (a) to (c), are consistent with what is to be expected of a system comprised of discrete particles. These small fluctuations also occur due to the acceleration and deceleration of trapped particles in the electrostatic potential of the wave structures observed in the electric field (Treumann and Baumjohann, 1997). These wave structures will be discussed later.

In comparing the energies at $\omega_{pe}t = 0$ and $\omega_{pe}t = 5000$ (averaged by its peak-to-peak fluctuation level), it should be noted that during the evolution of the instability, the kinetic energy of the electron species exhibits a net decrease of $\Delta(E_e/T_e) \approx 7$, as seen in Figure 3.2 (b). While the energy in the electric field and the kinetic energy of the ion species exhibit a net increase of $\Delta(E_f/T_e) \approx 0.4$ and $\Delta(E_i/T_e) \approx 6.6$, respectively, as seen in Figures 3.2 (a) and (c), respectively. Thus the net loss in kinetic energy of the electron species is compensated for by a gain in kinetic energy of the ion species, plus a relatively small gain in the electric field energy. It is noteworthy that the loss or gain of particle kinetic energy greatly exceeds the increase in the overall electric field energy. Therefore, the ion-acoustic instability can be viewed as the facilitating mechanism to redistribute energy in the plasma, by transferring energy from one species to another.

Figure 3.3 illustrates the phase space configuration plots, generated during the simulation, at the times $\omega_{pe}t = 0$; 684; 1203 and 4899, respectively. The top panel (blue colour) in each of the diagrams in Figures 3.3 (a) to (d), respectively, represents the electron phase space. The middle panel (green colour) in each diagram in Figures 3.3 (a) to (d) represents the ion phase space and the lower panel illustrates the electric field as a function of x/λ_{De}. Due to the normalisation scheme used, the electric field in the simulation $E^{'}$ is expressed as $E^{'} = E_x/(n_{0e}T_e/\epsilon_0)^{1/2}$, where E_x is the x component of the electric field in S.I. units, see Appendix C.

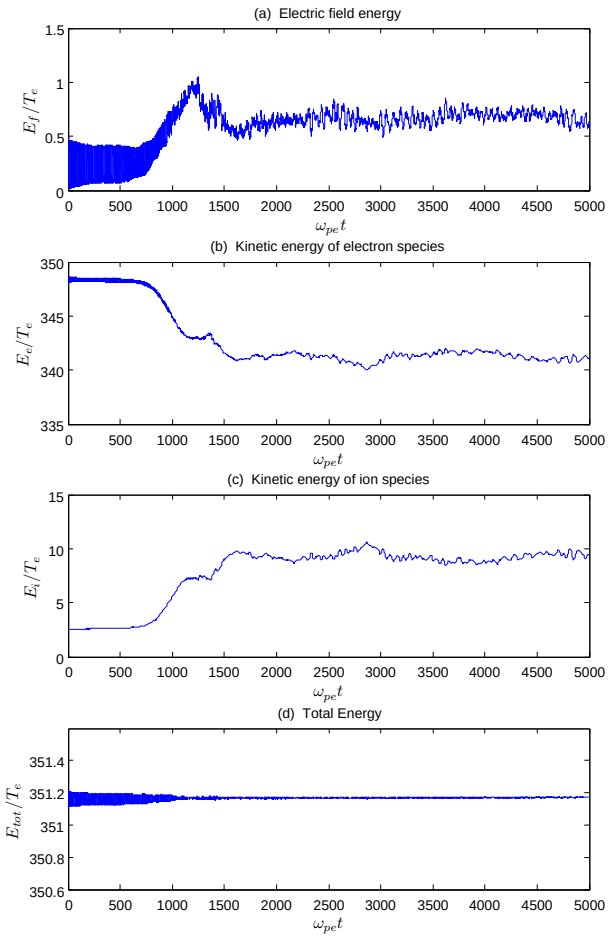

Figure 3.2: The time evolution of (a) the electric field energy E_f/T_e, (b) the kinetic energy of the electron species E_e/T_e, (c) the kinetic energy of the ion species E_i/T_e and (d) the total energy E_{tot}/T_e in the Maxwellian plasma. Three phases in the evolution of the ion-acoustic wave are observed. In the first phase, at times $0 < \omega_{pe}t < 1230$, the wave energy, (a), grows through resonant interaction with the electron velocity distribution. In the second phase, at times $1230 < \omega_{pe}t < 1700$, the wave energy saturates, stops growing and begins to decrease, seen in (a) at times $1230 < \omega_{pe}t < 1700$. In the final phase, at times $\omega_{pe}t > 1700$, the system settles to a quasi-equilibrium state and wave energy remains approximately constant.

During this simulation, a number of these phase space plots for each species along with plots of the electric field were exported in image format. These were then combined into the movie clip named *ion-acoustic-maxwellian.mpg*, which is supplied with this thesis. This movie clip enables a time-lapsed viewing of the plasma dynamics as well as the evolution to the electric field.

Figure 3.3 (a) illustrates the initial phase space configuration of the electron and ion species (the top and middle panels, respectively) as well as the initial electric field present in the plasma (lower panel). Figure 3.3 (a) serves as a reference plot and aids in the observation of the changes to the plasma system.

The plots of Figure 3.3 (b) were generated at $\omega_{pe}t = 684$, corresponding to a time during the growth phase of the ion-acoustic wave. Ion-acoustic wave packets are observed in the electric field, e.g., at $x/\lambda_{De} \approx 310$, compare the lower panels of Figures 3.3 (a) and (b). At the location of the forming wave packets, ion acceleration is also observed, as can be seen by the "fingers" evident in the ion phase space, the middle panel of Figure 3.3 (b), at $x/\lambda_{De} \approx 310$. This ion acceleration by the electric field is responsible for the increase in the kinetic energy of the ion species observed earlier in Figure 3.2 (c).

The ion-acoustic wave packet amplitudes grow in time and eventually the wave amplitude becomes large enough, through the deepening of the potential well and the widening of the wave resonance, to trap the ions in the electrostatic potential. This is evident in the ion phase space plot, seen in the middle panel of Figure 3.3 (c), generated at time $\omega_{pe}t = 1203$, where a phase space vortex structure emerges at $x/\lambda_{De} \approx 330$. This vortex structure corresponds to ions oscillating in the well of an ion-acoustic solitary wave. The vortex structure leads to ion mixing in phase space, which will reduce wave coherence and hence the effect of trapping. The emergence of the soliton-like structures in the electric field, with accompanying ion trapping is a sign of significant nonlinearity.

The concomitant heating of the ion species gives rise to a broadening of the velocity distribution in the phase space of the ions (Lu et al., 2005), as can be seen by comparing the ion phase space (middle panel) of Figure 3.3 (c), generated at $\omega_{pe}t = 1203$, with that of Figure 3.3 (d), generated at the time $\omega_{pe}t = 4899$ (corresponding to the quasi-equilibrium phase). At this later time, the amplitude of the solitary wave structures are observed to have decreased, as seen by comparing the electric fields (lower panels) in Figures 3.3 (c) and (d) around $x/\lambda_{De} \approx 330$.

Although it is difficult to observe changes in the electron velocity distribution in the electron phase space plots [top panels in Figures 3.3 (a) to (d)], the electron velocity distribution does undergo changes. In the vicinity of the ion-acoustic speed a significant amount of plateau formation in the electron velocity distribution, arises, which will be discussed later.

Figures 3.4 (a) illustrates the evolution of the electron velocity distribution during the initial growth phase of the instability, up to times just after maximum electric field energy is attained, i.e., during $0 \leq \omega_{pe}t \leq 1250$. The ion-acoustic speed, predicted by our parameters to be $v_s = 0.1v_{the}$ and indicated by the dashed vertical line, initially coincides with the positive slope of the initial electron velocity distribution [see velocity distribution plot at $\omega_{pe}t = 0$ in Figure 3.4 (a)]. Thus, resonant electrons will supply energy to the wave through the process of inverse Landau damping (Treumann and Baumjohann, 1997; Chen, 2006). As a result, a depletion in particle numbers around the ion-acoustic speed is observed in the electron velocity distribution, as seen in the velocity distribution plots in Figure 3.4 (a) for the times $250 \leq \omega_{pe}t \leq 1250$, where a visible plateau develops. At the same time, the number of particles travelling slower than the wave is observed to gradually increase as electrons lose energy to the waves. This redistribution of electron energies eventually leads to a state, as seen at $\omega_{pe}t = 1250$, where the slope of the the electron velocity distribution, at the ion-acoustic speed $v_s = 0.1v_{the}$, is negative. This causes the onset of Landau damping, causing the dissipation of the wave energy and leads to saturation of the instability.

Figure 3.4 (b) illustrates the evolution of the electron velocity distribution during a time corresponding to the quasi-equilibrium phase of the simulation, i.e., at times $\omega_{pe}t \geq 2000$. The electron velocity distribution is now flat topped with a shoulder in the distribution, formed near $v_x/v_{the} \approx 2$. The source of instability, a positive value of df/dv at v_s, is now removed and the electron velocity distribution is observed to remain approximately constant during this time, consistent with the quasi-equilibrium phase.

Figure 3.5 illustrates the evolution of the ion velocity distribution throughout the duration of the simulation. The increase in the spread of the velocity distribution as the simulation progresses indicates bulk heating of the ion species (Lu et al., 2005). This spread was also observed in the ion phase space in Figure 3.3 (d). One also observes a shift in the mean velocity towards a positive value in Figure 3.5, indicating that the ions develop a net drift velocity, $v_d \approx 0.01v_{the}$, in the direction of the electron drift, after

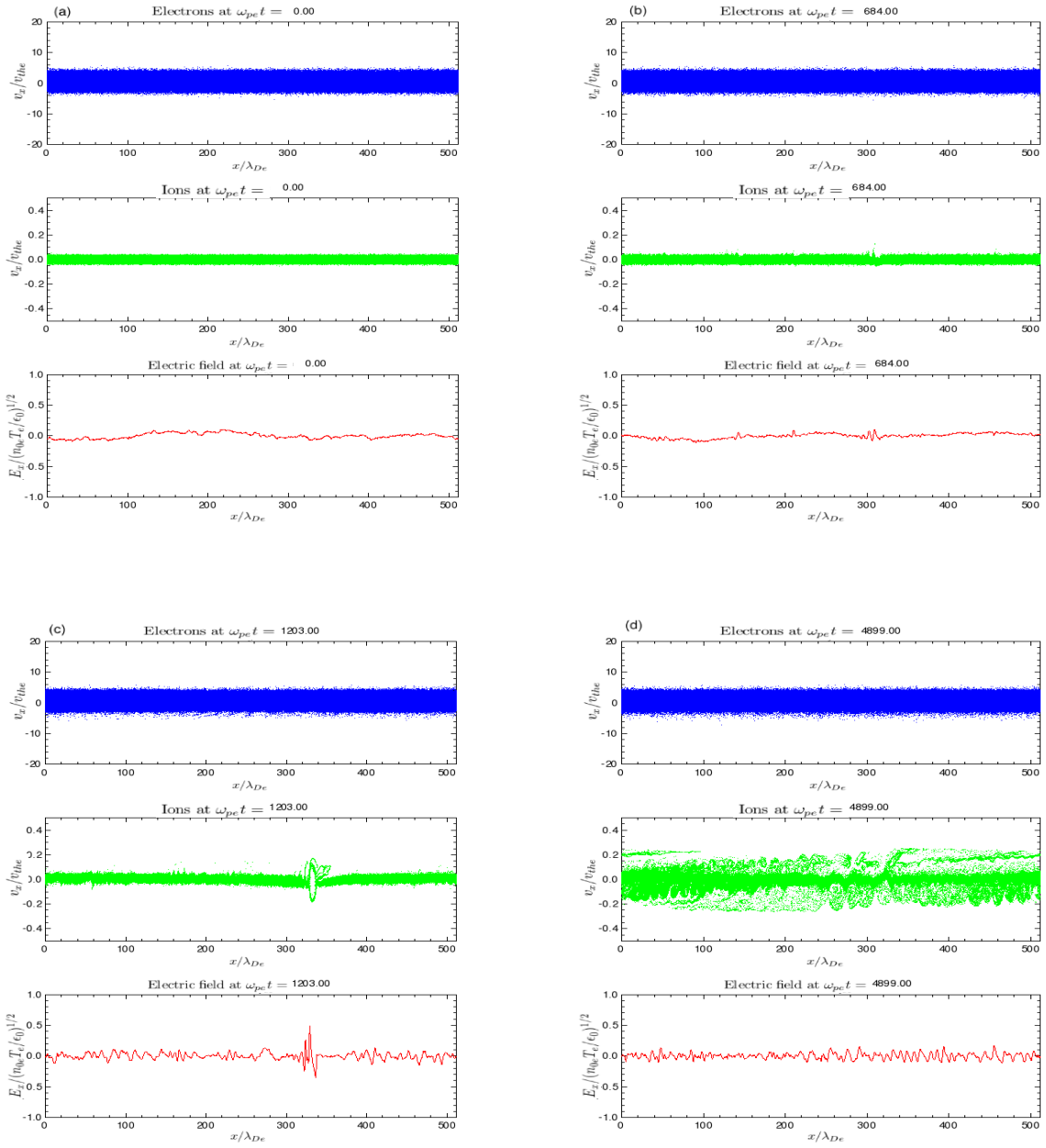

Figure 3.3: The electron phase space [top panel in each plot (a) to (d)], ion phase space [middle panel in each plot (a) to (d)] and electric field as a function of x/λ_{De} [lower panel in each plot (a) to (d)] for the Maxwellian plasma, generated at the times $\omega_{pe}t = 0$; 684; 1203 and 4899, respectively.

saturation of the ion-acoustic instability.

A series of plots are presented in Figure 3.6. The plots on the left hand side of Figure 3.6 represent the electric field (wave) intensity during the simulation run. The plots on the right hand side of Figure 3.6 are those with the analytic dispersion relation for the ion-acoustic wave, Equation (3.5), superimposed.

The electric field intensity, as a function of ω and k, in the simulation is given in Figure 3.6 (a) for the time interval $0 \leq \omega_{pe}t \leq 800$, corresponding to wave growth. The theoretical dispersion relation for ion-acoustic waves, Equation (3.5), is superimposed on the plot in the right-hand panel. The maximum wave intensities, $\epsilon_0 E^2 \approx 10^8 n_{0e} T_e$, seen as darker red regions in the plots of Figure 3.6 (a), coincide with the linear dispersion relation, Equation (3.5). This indicates that the maximum wave energy during this phase is concentrated in the ion-acoustic wave.

The right-hand panel of Figure 3.6 (a) shows that at $0 < k\lambda_{De} < 0.5$, the dominant wave energy density lies where the wave is essentially acoustic in nature, having $\omega/k \simeq v_s$, as seen in the right hand plot of Figure 3.6 (a) where this line is superimposed. However, Figure 3.6 (a) also indicates significant levels of wave activity at wavenumbers up to $k\lambda_{De} \approx 3$ and at frequencies approaching the ion plasma frequency, $\omega_{pi} \equiv \omega/\omega_{pe} = 0.1$.

Figure 3.6 (b) illustrates the electric field intensity over the interval $800 \leq \omega_{pe}t \leq 1600$, i.e., just prior to the simulation progressing to the quasi-equilibrium phase. Areas of high electric field intensity are seen to be present over a larger frequency range as well as over a larger range of $k\lambda_{De}$ values, than seen in Figure 3.6 (a). While some of the strongest wave activity still occurs along the branches of the ion-acoustic wave, Equation (3.5), the maximum electric field intensity is no longer concentrated just in the ion-acoustic mode, as other modes, not described by the linear dispersion relation receive energy. The enhanced levels of fluctuations that do not follow this linear relation are indicative of the presence of nonlinear effects. Significant wave energy is observed to lie also around a beam-like mode, as can be seen in the right-hand panel of Figure 3.6 (b), where we have overplotted the relation $\omega = v_b k$, where $v_b = 2v_{the}$. This corresponds to the shoulder observed in the velocity distribution of the electron species seen in Figure 3.4.

Figure 3.6 (c) illustrates the electric field intensity over the interval $4000 \leq$

(a)

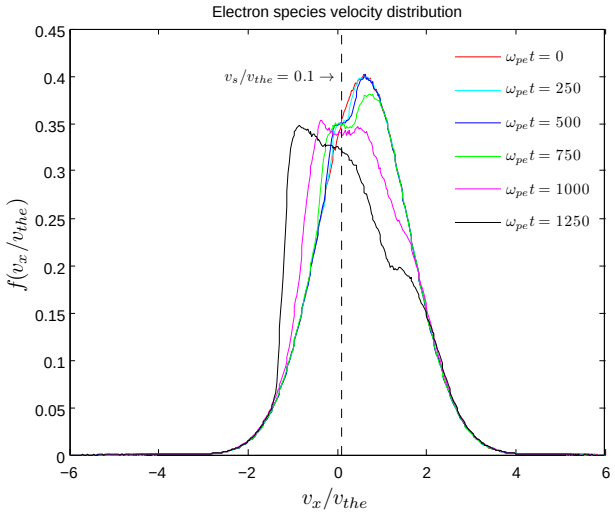

(b)

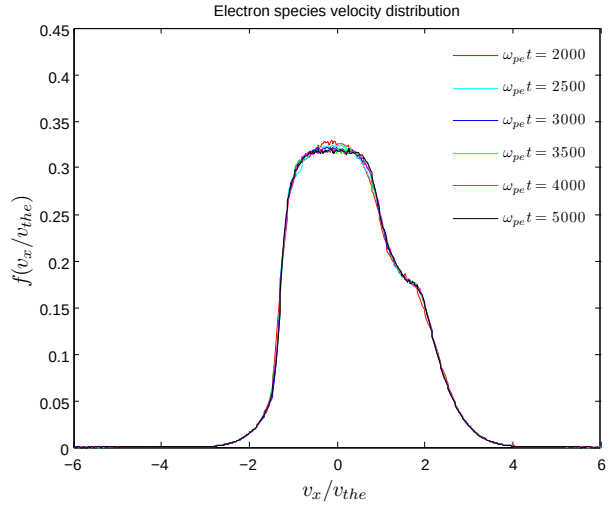

Figure 3.4: The evolution of the electron velocity distribution (a) over the growth and saturation phase of the ion-acoustic instability, illustrating the resonant interaction between the electron species and the wave, at the ion-acoustic speed (indicated by the dashed vertical line), and (b) over the quasi-equilibrium phase of the simulation, for the Maxwellian plasma.

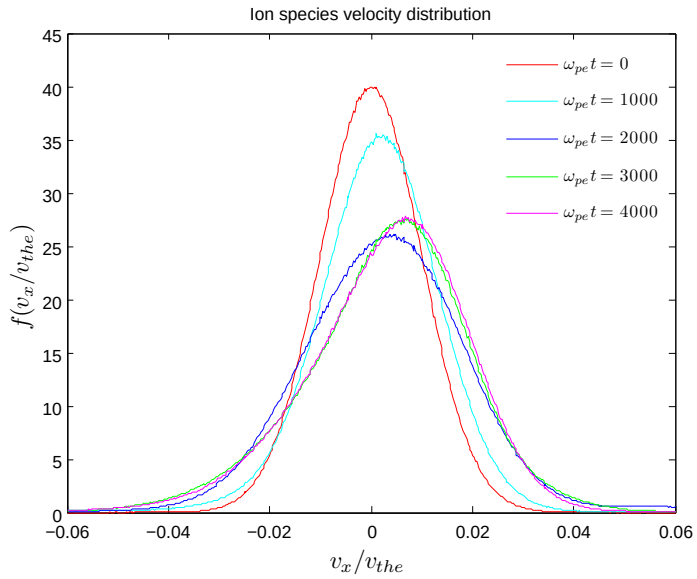

Figure 3.5: The evolution of the ion velocity distribution throughout the simulation for the Maxwellian plasma. The spread of the velocity distribution indicates bulk heating of the ion species and the shift in the mean velocity indicates that the ion species gains a net positive drift after saturation of the ion-acoustic instability.

$\omega_{pe}t \leq 4800$, corresponding to the quasi-equilibrium phase. During this period the wave intensity distribution narrows in frequency and wavenumber as sources of instability are quenched and the plasma settles to a quasi-equilibrium state. As is seen in the right-hand panel of Figure 3.6 (c), the dark red regions of the electric field intensity coincide with the linear dispersion relation, Equation (3.5). A weak beam-like mode having $\omega = v_b k$ is also visible in the right-hand panel of Figure 3.6 (c), where $v_b = 2v_{the}$, corresponding to the velocity at the shoulder of the electron velocity distribution [see Figure 3.4 (b)]. While the cause of this beam mode is uncertain at present, we do note that the overall electron velocity distribution in Figure 3.4 (b) can be thought of as arising from a drifting Maxwellian beam, $v_d \approx 2v_{the}$, superimposed on a flat-topped core of stationary electrons.

3.4 PIC simulation for a kappa plasma

3.4.1 Simulation run parameters

The simulation runs carried out and described in this chapter were aimed at investigating the ion-acoustic instability under two conditions. In the first, the velocity distributions of the plasma electrons and ions were modelled by Maxwellian distributions (corresponding $\kappa = \infty$). In the second, the velocity distributions of the electrons and ions were modelled by kappa distributions (with equal kappa indices $\kappa_e = \kappa_i = 2$).

Presented here are the results of the simulation run for the plasma in which the initial state for each plasma species, electrons and ions, was modelled by kappa velocity distributions. The particle loader described in Section 2.1.2 (p. 15) was used to load plasma particles in phase space having an initial kappa velocity distribution, with drift if necessary. All particle positions were loaded uniformly throughout the simulation box, akin to the Maxwellian simulation run.

To investigate the effects of the kappa distribution on the ion-acoustic instability, all run parameters in the present simulation were made identical to those of the Maxwellian simulation run described in Section 3.3 (p. 45). A box length of $L = 512\lambda_{De}$ was used with a total of 2048 cells. The simulation employed a time step Δt satisfying $\omega_{pe}\Delta t = 0.1$, and the simulation was evolved up to time $\omega_{pe}t = 5000$.

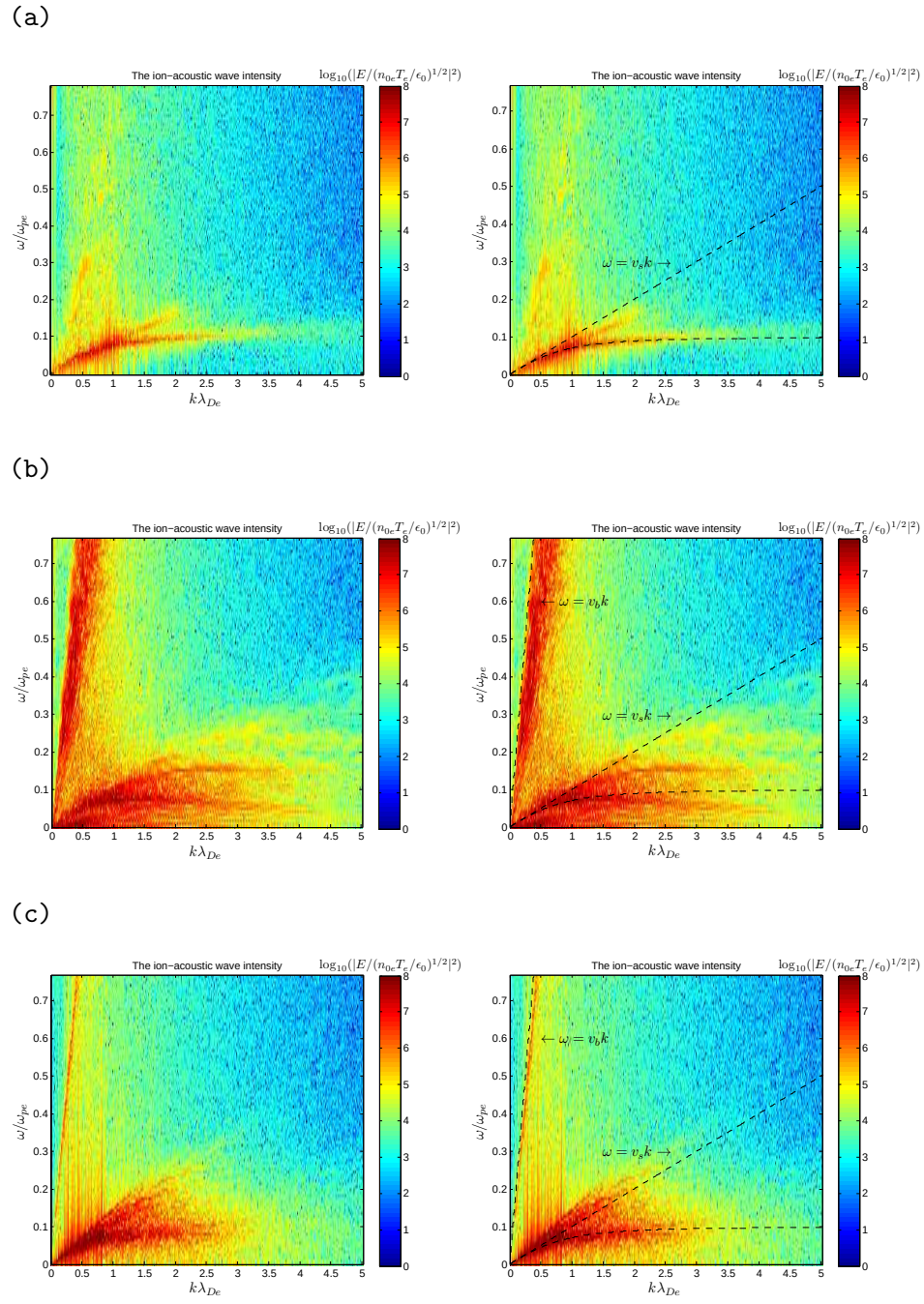

Figure 3.6: The electric field intensity of the ion-acoustic wave in the Maxwellian plasma for the time interval corresponding to (a) the ion-acoustic wave growth phase $0 \leq \omega_{pe}t \leq 800$, (b) the wave saturation phase $800 \leq \omega_{pe}t \leq 1600$ and (c) the quasi-equilibrium phase $4000 \leq \omega_{pe}t \leq 4800$. The linear dispersion relation is superimposed on the adjacent diagrams in (a) to (c) and is found to agree with the maximum intensities of the wave. Beam modes are also visible in (b) and (c).

The plasma species parameters were also kept identical to those of the Maxwellian simulation run, i.e., a stationary ion species and drifting electron species was used, see Table 3.1 (p. 46). However, to destabilise the ion-acoustic wave in an analogous manner to the Maxwellian simulation run, which used an initial electron drift velocity of $v_d = 6v_s = 0.6v_{the}$, the initial electron drift velocity used in the kappa plasma was $v_d = 6v_s^\kappa$. With our choice of species parameters and the definition of the ion-acoustic speed v_s^κ in Equation (3.9), $v_s^\kappa = 0.058v_{the}$. Thus the present simulation employed the initial electron drift velocity of $v_d = 6v_s^\kappa = 0.348v_{the}$.

3.4.2 Results of the simulation run

Figures 3.7 (a) and (b) compare (in green) the initial velocity distributions obtained for the electron and ion species, respectively, via our numerical loading algorithm [Section 2.1.2 (p. 15)] with the kappa distribution, Equation (2.5), using our simulation run parameters, which is superimposed in black. As with the Maxwellian simulation, the numerical approximation to the velocity distribution is obtained from each discrete plasma species using the method of "particle binning" described in Appendix E. Figures 3.7 (a) and (b) demonstrate very good agreement between the loaded velocity distributions of the plasma species and the kappa distribution, Equation (2.5), which confirms the correctness of our particle loading algorithm.

The dynamics of the plasma during the evolution of the ion-acoustic instability in the kappa plasma are expected to be similar to those of the Maxwellian plasma. Thus, as in the Maxwellian case, the ion-acoustic instability in the kappa plasma is expected to evolve over three distinct phases.

Figure 3.8 illustrates the time evolution of the electric field energy E_f/T_e [Figure 3.8 (a)], the kinetic energy of the electron species E_e/T_e [Figure 3.8 (b)], the kinetic energy of the ion species E_i/T_e [Figure 3.8 (c)] and the total energy E_{tot}/T_e in the plasma [Figure 3.8 (d)]. As with the Maxwellian simulation run described in Section 3.3 (p. 45), all energies for this, the kappa simulation run, are expressed in terms of the initial electron thermal energy T_e.

Characteristics of the initial phase of ion-acoustic wave growth are clearly observed, during the interval $0 < \omega_{pe}t < 860$, in the evolution of the kinetic energies of both the electron and ion species, as seen in Figures 3.8 (b) and

(a)

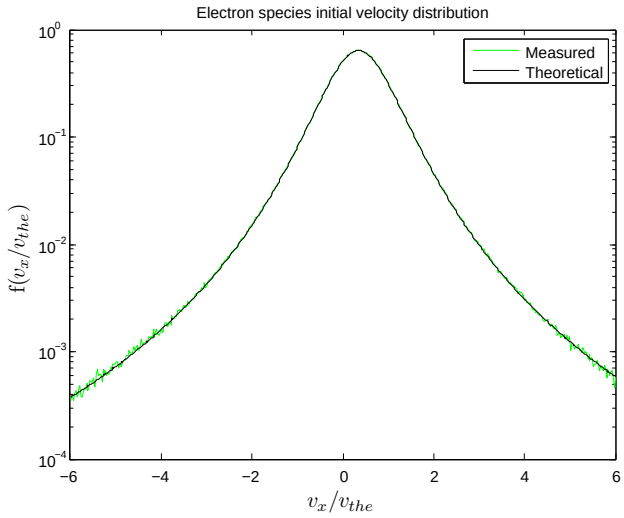

(b)

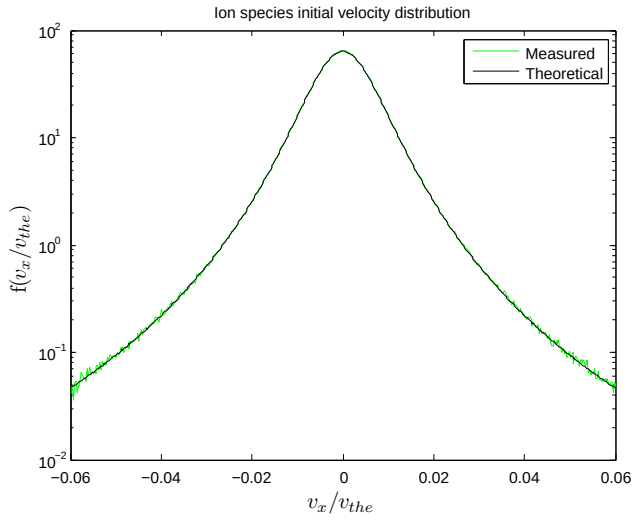

Figure 3.7: The measured initial velocity distribution (in green) for (a) the electron species and (b) the ion species along with the kappa distribution, Equation (2.5) (in black), for the parameters listed in Table 3.1. The agreement between the measured velocity distributions and the kappa for both the electron and ion species confirms the correctness of our particle loading.

(c). There is an exponential decrease in the kinetic energy of the electron species E_e/T_e [as seen in Figure 3.8 (b)] and a corresponding exponential increase in the kinetic energy of the ion species E_i/T_e [as seen in Figure 3.8 (c)]. That the forming waves here are also of the ion acoustic type will be verified through analysis of the electric field intensity spectra, which will be presented later in Figure 3.12.

Large amplitude fluctuations are, however, seen to dominate the electric field energy E_f/T_e during the initial stages $0 < \omega_{pe}t < 570$, as seen in Figure 3.8 (a). These fluctuations obscure the exponential growth of the electric field energy with time, which was so clearly evident in the Maxwellian case, seen in Figure 3.2 (a) (p. 50). The amplitudes of the fluctuations in the electric field energy are also observed to be approximately the same size as those observed in the kinetic energy of the electron species during this period [compare Figures 3.8 (a) and (b) during $0 < \omega_{pe}t < 570$]. The amplitude of fluctuation in both the electric field energy as well as the kinetic energy of the electron species start out with a peak-to-peak amplitude of $E/T_e \approx 0.9$ and decrease as the simulation progresses. This level of fluctuations was not observed in the Maxwellian simulation run [see Figure 3.2 (a) (p. 50)]. It is noteworthy pointing out that Mace et al. (1998) investigated electrostatic fluctuations in plasmas with particles modelled by kappa velocity distributions and found that thermal fluctuations were enhanced, relative to the equivalent Maxwellian case, for low values of κ.

In other simulation runs of the ion-acoustic instability (not presented here), the use of a smaller number of particles, 2097152 and 4194304 particles per species, was found to increase the level of noise and fluctuations in the simulation. This is likely due to the inequality $n\lambda_D \gg 1$ (or $n\lambda_D^3 \gg 1$ in 3-D) being poorly satisfied in these cases, where n is the number of particles. The enhanced importance of discreteness effects in this case raises the level of thermal fluctuations. On the other hand, increasing the number of particles to over 2^{12} particles per cell sufficiently decreased the noise levels in our Maxwellian simulations; however, noise was still present in the simulation for the kappa plasma, during the interval $0 < \omega_{pe}t < 570$, when the same number of particles was used [compare Figure 3.2 (a) (p. 50) with that of Figure 3.8 (a)]. A further increase to 2^{13} particles per cell had little effect on reducing the fluctuation levels in the kappa case. This is due to λ_{De}, in the Maxwellian plasma, being larger than its appropriate generalisation, $\lambda_{\kappa e}$, in the kappa plasma. Thus, for the same n, the inequality $n\lambda_{\kappa e}^3 \gg 1$ is more poorly satisfied for the kappa plasma, compared to the equivalent

Maxwellian plasma. Thus, single particle behaviour is expected to play an enhanced role in the kappa plasma, and will lead to the enhancement of thermal fluctuations and higher levels of noise, as suggested by Mace et al. (1998).

The amplitude of the fluctuations seen in the electric field energy in Figure 3.8 (a) decreases with time and a local maximum in the electric field energy is attained at $\omega_{pe}t \approx 860$, corresponding to the end of the growth phase of the ion-acoustic instability. This local peak in the energy of the electric field, followed by a downward trend during $860 < \omega_{pe}t < 1200$, corresponds to saturation of the instability. It should be noted that the peak in the electric field energy at $\omega_{pe}t \approx 860$ in the kappa plasma, occurred earlier than it did in the Maxwellian plasma, which occurred at time $\omega_{pe}t \approx 1230$. Also, the peak in the electric field energy corresponded $E_f/T_e \approx 0.5$, in the kappa plasma, and $E_f/T_e \approx 1$ in the Maxwellian plasma [see Figure 3.2 (a) (p. 50)]. This suggests that the free energy in the kappa plasma becomes depleted and redistributed faster than it did in the Maxwellian plasma, perhaps due to faster instability growth rate. This is due to the kappa plasma having more resonant particles to interact with the wave than the Maxwellian had, which will be shown later. Thus more energy is given to the wave through the process of inverse Landau damping. This more rapid energy transfer between the particles and the wave, produces a spectrum of waves which are able to react back on the electron velocity distribution and erase the source of instability by plateau formation, which will be shown later.

Consequently, the kappa plasma settles to a quasi-equilibrium phase earlier, at times $\omega_{pe}t > 1200$, than it did in the Maxwellian plasma, which occurred at times $\omega_{pe}t > 1700$. The amplitudes of the fluctuations observed in the electric field energy during the quasi-equilibrium phase are observed to be smaller in the kappa plasma than they were in the Maxwellian plasma [compare Figure 3.8 (a) with that of Figure 3.2 (a) during their respective quasi-equilibrium phases]. This is likely due to the wave structures in the electric field having a relatively smaller amplitude in the kappa plasma, which will be shown later. A comparison of the saturation electric field energy in Figure 3.2 (a) and Figure 3.8 (a) shows that $E_f/T_e \approx 0.65$ in the Maxwellian case, whereas $E_f/T_e \approx 0.1$ in the kappa case, in agreement with the previous statement.

Figure 3.8 (d) shows that the total energy in the kappa plasma, during

the simulation run, was conserved, i.e., the energy remained approximately constant to within the errors of the simulation techniques and fluctuations arising due to using discrete particles. This gives us a high degree of confidence in the results obtained in this simulation run.

Figure 3.9 illustrates the electron and ion phase space configurations [top and middle panels of Figures 3.9 (a) to (d)] and the electric field [lower panels of Figures 3.9 (a) to (d)], at various times during the kappa simulation run. As with the Maxwellian simulation run, the electric field, due to our choice of normalisation scheme, is $E_x^{'} = E_x/(n_{0eT_e}/\epsilon_0)^{1/2}$, see Appendix C.

A movie clip named *ion-acoustic-kappa.mpg* was generated by combining a number of these plots produced during the simulation and is provided on the accompanying compact disk.

Figure 3.9 (a) shows the state of the electron and ion phase space, as well as the electric field at time $\omega_{pe}t = 0$. The larger number of high energy particles modelled by the kappa distribution is seen as a wider spread of the electrons and ions in the velocity range, than they were in the Maxwellian plasma [compare the top two panels of Figure 3.3 (p. 53) with those of Figure 3.9].

Ion-acoustic wave packets in the electric field can be seen at $x/\lambda_{De} \approx 80$ and $x/\lambda_{De} \approx 380$ in the lower panel of Figure 3.9 (b), which was generated at $\omega_{pe}t = 450$. Owing to the faster growth rate of the ion-acoustic instability in the present case, ion-acoustic wave packets in the electric field were observed to occur sooner, at $\omega_{pe}t \approx 450$, compared with $\omega_{pe}t \approx 684$ as observed in the Maxwellian plasma [see Figure 3.3 (b) (p. 53)].

As in the Maxwellian case, the ion acoustic wave packets grow in amplitude over time, as can be seen by comparing the lower panels of Figures 3.9 (b) and (c) at $x/\lambda_{De} \approx 100$ and $x/\lambda_{De} \approx 390$, which were generated at $\omega_{pe}t = 684$ and $\omega_{pe}t = 804$, respectively. However, the amplitudes of these growing waves, during the time just prior to saturation, are smaller in the kappa plasma than they were in the Maxwellian plasma. In the former the fluctuating electric field satisfied $-0.3 \lesssim E_x/(n_{0e}T_e/\epsilon_0)^{1/2} \lesssim 0.3$, whereas in the latter (Maxwellian) it satisfied $-0.5 \lesssim E_x/(n_{0e}T_e/\epsilon_0)^{1/2} \lesssim 0.5$. Visual confirmation of this difference can be gained by comparing the lower panels of the plots generated just prior to the onset of the saturation phase of the ion-acoustic instability in the kappa plasma [see Figure 3.9 (c) at $x/\lambda_{De} \approx$ 100 and 390] and in the Maxwellian plasma [see Figure 3.3 (c) at $x/\lambda_{De} \approx$

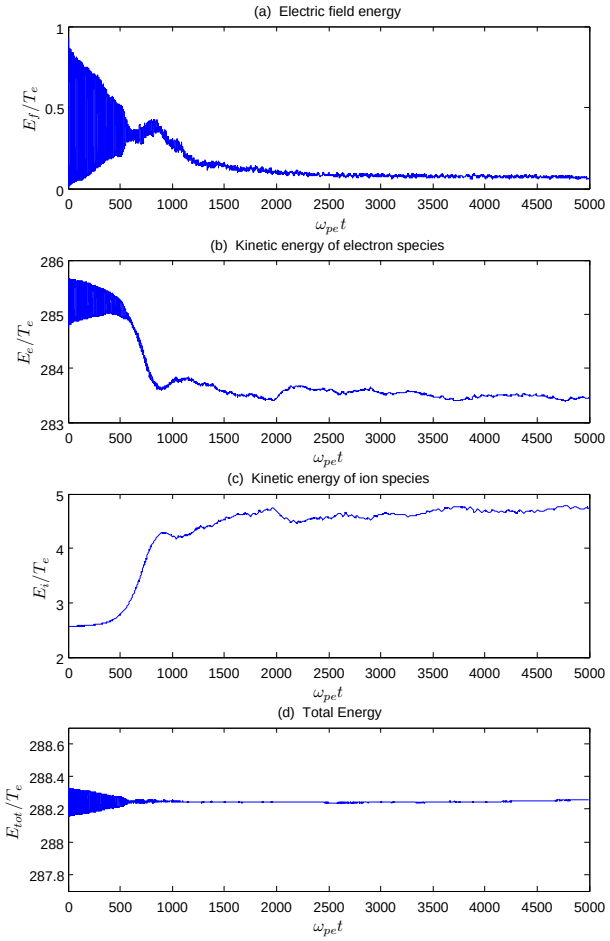

Figure 3.8: The time evolution of (a) the electric field energy E_f/T_e, (b) the kinetic energy of the electron species E_e/T_e, (c) kinetic energy of the ion species E_i/T_e and (d) the total energy E_{tot}/T_e in the kappa plasma. Three phases of the evolution of the ion-acoustic instability are observed, i.e., wave growth during the interval $0 < \omega_{pe}t < 860$, saturation of the instability during the interval $860 < \omega_{pe}t < 1200$ and a settling of the plasma to a quasi-equilibrium state at times $\omega_{pe}t > 1200$.

300], respectively. Ion trapping by these growing ion-acoustic wave packets is now less likely due to the larger number of energetic particles provided by the tail of the kappa distribution. Thus the same level of ion trapping by the growing waves was not observed in the ion phase space of the kappa plasma, as it was in the Maxwellian plasma, i.e., no vortex like structures were observed to form in the ion phase space of the kappa plasma whereas they did in the Maxwellian plasma [see Figure 3.3 (c) (p. 53), centre panel].

As in the Maxwellian case, when the kappa plasma settles to a quasi-equilibrium state, the amplitude of the ion acoustic wave packets decreases due to the depletion and redistribution of free energy in the plasma [compare the lower panels of Figure 3.9 (c) (generated at $\omega_{pe} = 804$) and Figure 3.9 (d) (generated at $\omega_{pe} = 4986$)]. The amplitude of the ion acoustic wave packets during the equilibrium phase are also smaller than they were in the Maxwellian plasma, as can be seen when comparing Figure 3.9 (d) with that of Figure 3.3 (d) during their respective quasi-equilibrium phases.

A slight broadening of the ion phase space with time is observed when comparing the middle panels of Figures 3.9 (c) and (d). Similar to the Maxwellian simulation run, we speculate that this is due to the acceleration of the ion species by the excited waves in the kappa plasma and is the reason for the increase in the kinetic energy of the ion species observed earlier in Figure 3.8 (c).

Figures 3.10 (a) and (b) illustrate the evolution of the electron velocity distribution during the simulation run. Figure 3.10 (a) illustrates the evolution of the electron velocity distribution during the growth phase and up to times just after maximum field energy is attained, i.e., during $0 \leq \omega_{pe}t \leq 1000$. The ion-acoustic speed for the kappa plasma, predicted by our choice of run parameters to be $v_s^{\kappa} = 0.058 v_{the}$, is indicated by the dashed vertical line. The ion-acoustic speed is observed to coincide with the positive slope of the initial electron velocity distribution, as seen on the curve in Figure 3.10 (a) for the plot at $\omega_{pe}t = 0$. Thus, wave growth occurs due to inverse Landau damping in the same way as it did in the Maxwellian case.

The ion-acoustic speed in the kappa plasma now, however, coincides with a steeper slope on the electron velocity distribution than it did in the Maxwellian plasma. This can be seen by comparing the slope of the initial electron velocity distribution at the ion-acoustic speeds, in the Maxwellian plasma [the plot at $\omega_{pe}t = 0$ in Figure 3.4 (a) (p. 55)] with that of the kappa plasma [the plot at $\omega_{pe}t = 0$ in Figure 3.10 (a)]. Thus, there are more

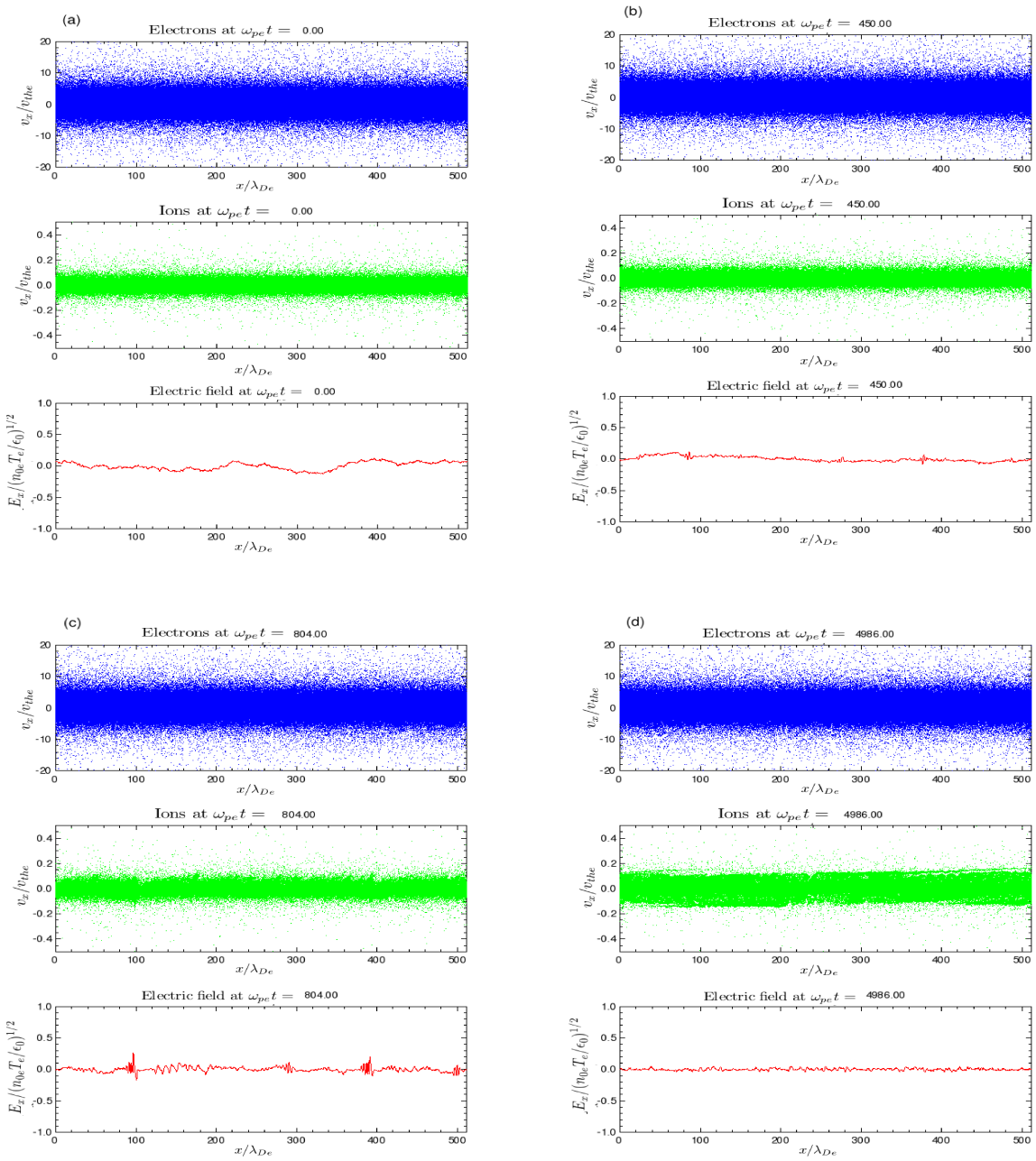

Figure 3.9: The electron phase space [top panel in each plot (a) to (d)], ion phase space [middle panel in each plot (a) to (d)] and electric field as a function of x/λ_{De} [lower panel in each plot (a) to (d)] for the kappa plasma, generated at the times $\omega_{pe}t = 0$; 450; 804 and 4986 respectively.

particles available to resonantly interact with the wave in the kappa plasma and the effects of wave-particle interactions are enhanced. The resonant wave-particle interaction results in amplified waves whose back-reaction on the electron species results in the formation of a plateau in the electron velocity distribution, seen in Figure 3.10 (a). At the same time, the number of particles travelling slower than the wave is observed to gradually increase as the electrons lose energy to the wave. The redistribution of energy leads to a state, as seen at $\omega_{pe}t = 1000$ in Figure 3.10 (a), where the slope of the electron velocity distribution at the ion-acoustic speed, is negative. This causes the onset of Landau damping and dissipation of free energy in the plasma.

Figure 3.10 (b) illustrates the evolution of the electron velocity distribution during $1500 \leq \omega_{pe}t \leq 5000$, i.e., a time interval corresponding to the quasi-equilibrium phase of the ion-acoustic instability. Here the source of instability, i.e., the positive slope at the ion-acoustic speed, has been effectively removed by wave-particle interaction resulting in an electron velocity distribution that is flat topped with a shoulder in the distribution at the velocity $v/v_{the} \approx 1$. This shoulder in the electron velocity distribution was also observed in the Maxwellian simulation run; however, it occurred at the velocity $v/v_{the} \approx 2$ in that case. The electron velocity distribution remains approximately constant during the time interval $1500 \leq \omega_{pe}t \leq 5000$, consistent with the quasi-equilibrium phase.

Figure 3.11 illustrates the evolution of the ion velocity distribution throughout the simulation run. Similar to the Maxwellian simulation run, bulk heating of the ion species in the kappa plasma occurs as the instability evolves, seen as the spread of the ion velocity distribution with time. Also, the ions in the kappa plasma gain a small net drift of $v/v_{the} \approx 0.0025$, as seen by the shift in the mean value of the ion velocity distribution at time $\omega_{pe}t \approx 5000$.

A series of plots of electric field (wave) intensity, generated during the simulation run, are presented in Figure 3.12. The plots on the left hand side represent the raw data, while those on the right-hand side have the analytic dispersion relation, Equation (3.8), superimposed.

Figure 3.12 (a) illustrates the electric field intensity, as a function of ω and k, during $0 \leq \omega_{pe}t \leq 500$, i.e., a time interval corresponding to wave growth. In the right hand panel of Figure 3.12 (a), the dispersion relation for ion-acoustic waves, Equation (3.8) is superimposed. The maximum electric

(a)

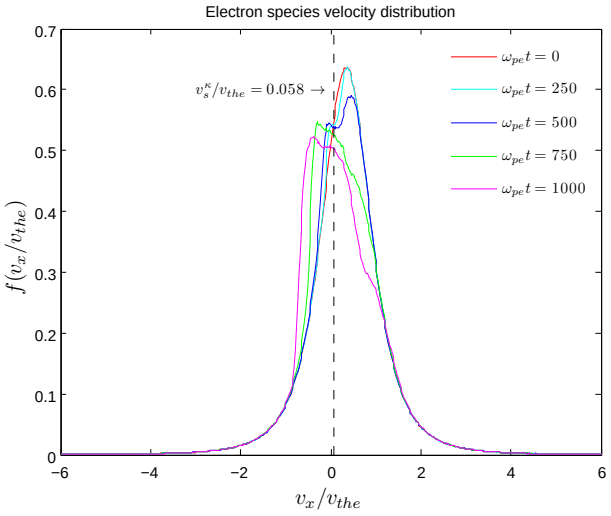

(b)

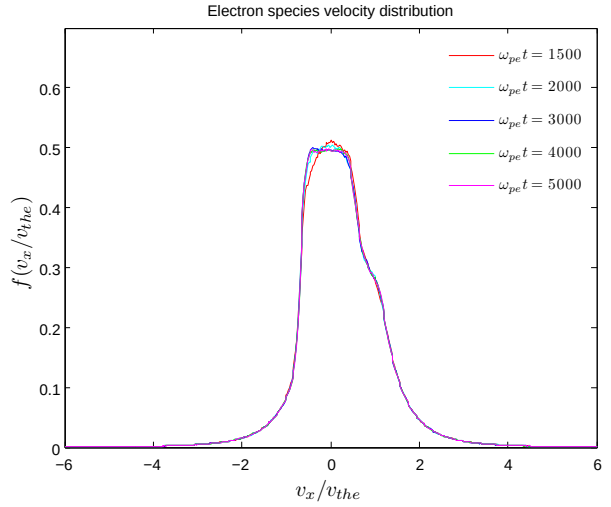

Figure 3.10: The evolution of the measured electron velocity distribution in the kappa plasma for (a) the growth and saturation phase of the ion-acoustic instability, showing resonant interaction and plateau formation at the ion-acoustic speed (indicated by the dashed vertical line) and (b) the quasi-equilibrium phase of the simulation.

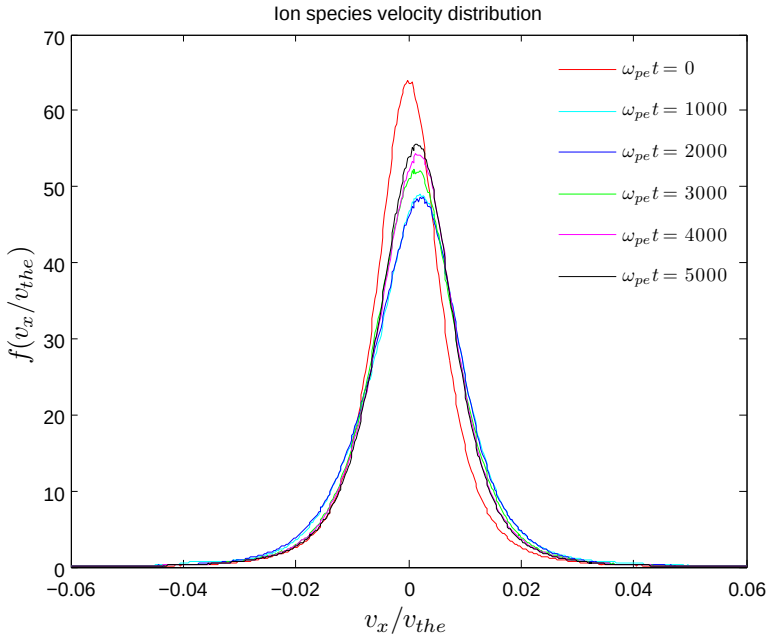

Figure 3.11: The evolution of ion velocity distribution throughout the simulation of the kappa plasma. Bulk ion heating is evident from the spread in the ion velocity distribution. The ions also attain a positive drift after the ion-acoustic instability saturates, indicated by the shift in the mean velocity to a positive value.

field intensities, $\epsilon_0 E^2 \approx 10^8 n_{0e} T_e$, seen as the dark red regions in the plots of Figure 3.12 (a), are observed to agree fairly well with the linear dispersion relation given by Equation (3.8). This indicates that the maximum wave energy is concentrated in the ion-acoustic modes during this time interval.

As with the Maxwellian plasma case presented in Section 3.3 (p. 45), enhanced fluctuations in wave energy density during this time interval are observed to lie in the small wavenumber regime, $0 < k\lambda_{De} < 2.5$. Significantly, we observe that enhanced levels of fluctuations occur at $k\lambda_{De} < 1$, where the ion-acoustic wave is truly acoustic. The acoustic regime of the wave now, however, satisfies $\omega \simeq v_s^\kappa k$, with v_s^κ the ion sound speed in a kappa plasma, Equation (3.9), as seen in the right hand plot of Figure 3.12 (a) where this line is superimposed. In the Maxwellian plasma, the acoustic regime of the wave satisfied $\omega \simeq v_s k$, where v_s is defined in Equation (3.4). In this initial phase of the instability, significant levels of wave intensity are also observed to occur at frequencies approaching the ion plasma frequency $\omega_{pi} = 0.1\omega_{pe}$.

Figure 3.12 (b) illustrates the electric field intensity during the interval $500 \leq \omega_{pe}t \leq 1000$, i.e., during the phase of the instability just prior to saturation. The areas of high electric field intensity are observed to be present over a larger frequency range, as well as over a larger range of $k\lambda_{De}$ values [compare the plots of Figures 3.12 (a) and (b)]. Some of the strongest wave activity still occurs along the linear ion-acoustic wave mode, as seen in the right hand plot of Figure 3.12 (b), where the dispersion relation defined by Equation (3.8) is superimposed. However, widespread levels of enhanced fluctuations that do not follow this linear dispersion relation are present and indicate non-linear effects. Significant wave energy is observed to also lie in the region around the beam-like mode defined by $\omega = v_b k$, where $v_b \approx 1 v_{the}$, corresponding to the shoulder observed in the electron velocity distribution in Figure 3.10. This can be seen in the right hand plot of Figure 3.12 (b) where the relation $\omega = v_b k$ is overplotted.

Figure 3.12 (c) illustrates the electric field intensity during $4000 \leq \omega_{pe}t \leq 4500$, i.e., a time interval corresponding to the quasi-equilibrium phase of the ion-acoustic instability. During this period, the wave intensity distribution narrows in frequency and wavenumber as sources of instability are quenched and the plasma settles to a quasi-equilibrium state. As seen in the right hand plot of Figure 3.12 (c), the dark red regions of maximum electric field intensity once again follow the ω and k values predicted by the linear

dispersion relation, Equation (3.8). Traces of the beam-like mode, observed earlier, are also visible in Figure 3.12 (c), where the relation $\omega = v_b k$ is overplotted in the right-hand panel, showing good agreement with the wave intensity distribution. However, this mode is no longer as intense as it was in Figure 3.12 (b), and occurs in a much narrower band of ω and k. As in the Maxwellian simulation run, the cause of this beam mode is uncertain at present, but we speculate that its presence has to do with the shoulder at $v \approx v_{the}$ observed on the electron velocity distribution, post saturation.

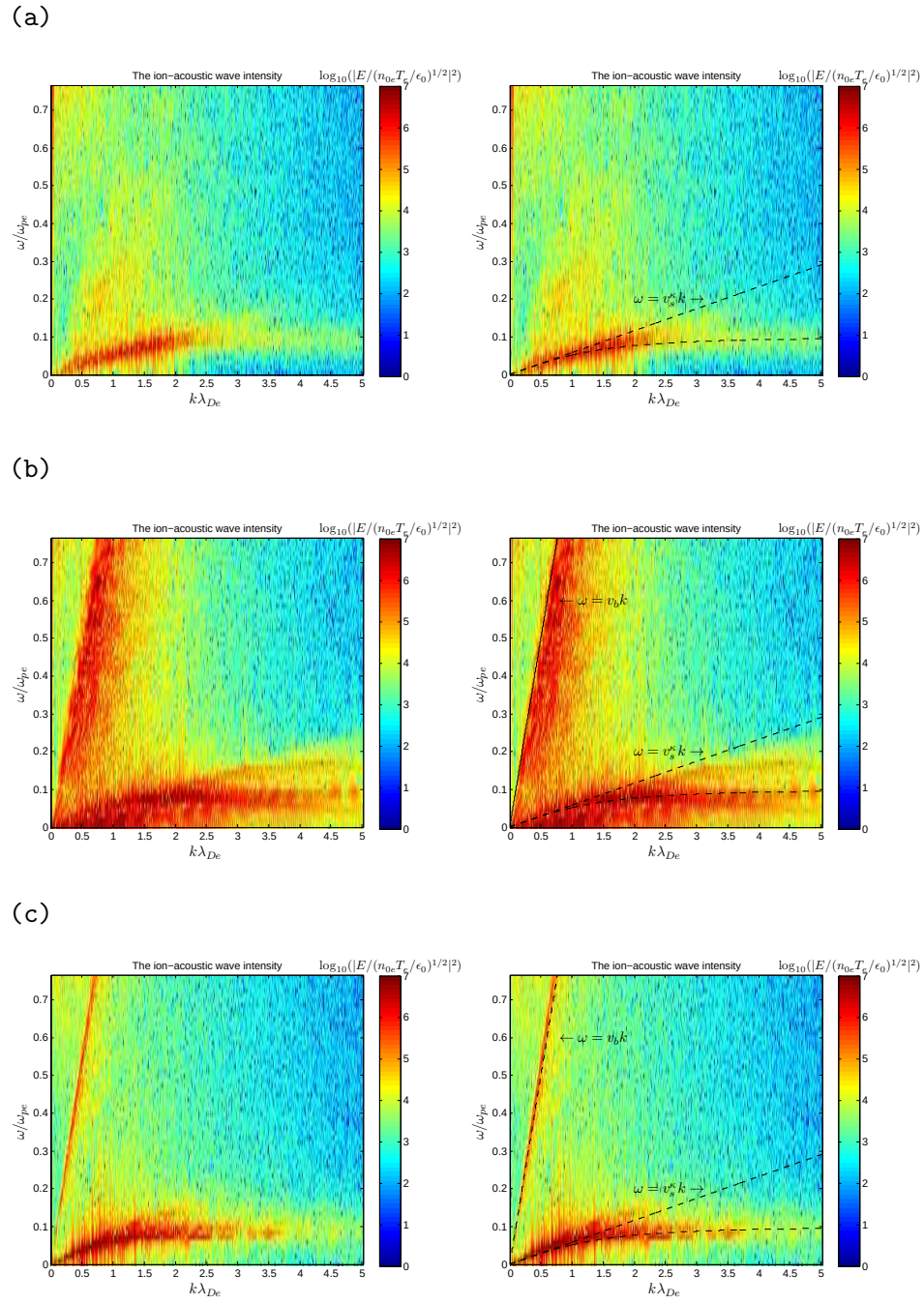

Figure 3.12: The electric field intensity of the ion-acoustic wave in the kappa plasma during the time interval corresponding to (a) the ion-acoustic wave growth phase $0 \leq \omega_{pe}t \leq 500$, (b) the wave saturation phase $500 \leq \omega_{pe}t \leq 1000$ and (c) the quasi-equilibrium phase $4000 \leq \omega_{pe}t \leq 4500$. The linear dispersion relation for the ion-acoustic wave is superimposed on the right hand panels in (a) to (c) and is found to agree with the maximum intensities of the wave. The beam modes are also visible in (b) and (c).

Chapter 4

Simulation of electrostatic Bernstein waves

As a further case study, electrostatic waves propagating perpendicular to a static magnetic field $\boldsymbol{B}_0$, directed along the z axis, were investigated. The incorporation of a finite $\boldsymbol{B}_0$ necessitates a one-and-two-halves dimensional simulation to adequately describe the dynamics of the plasma. That is, although only the x component of the particle position vector is relevant, owing to the presence of the magnetic field, both its v_x and v_y are dynamically essential. The one-and-two-halves dimensional simulations carried out and presented in this chapter were, as before, for a plasma in which the electrons and ions were modelled by either an isotropic Maxwellian, or an isotropic kappa velocity distribution. The electric field (wave) intensities, as a function of ω and k, were computed through taking the Fourier transform of the electric field in space and time, and were found to agree well with the analytic linear dispersion curves for electrostatic Bernstein waves derived by Mace (2003, 2004). The dispersion characteristics of the Bernstein waves and their relationship to the observed field fluctuations will be discussed in this chapter.

4.1 Overview of electrostatic Bernstein waves

The motion of a charged particle in a uniform magnetic field, projected onto a plane perpendicular to the magnetic field, is circular motion with an angular frequency $\omega_c = qB/m$ and Larmor radius $R_L = v_\perp/\omega_c$. Thus, the introduction of a magnetic field in a plasma will produce finite Larmor orbit effects (Swanson, 2003). When the plasma particles perform orbits strictly perpendicular to the magnetic field, a class of longitudinal waves known as electrostatic Bernstein waves are produced (Bernstein, 1958).

Due to the disparate masses and mobility of the electrons and ions, two types of Bernstein waves can propagate in electron-ion plasmas. The first type is governed by electron dynamics and is called the electron Bernstein wave. These waves have frequencies in excess of the electron cyclotron frequency ω_{ce} and wavelengths short compared to the Debye length (Crawford, 1965). Electron Bernstein waves propagate between harmonics of the electron cyclotron frequency.

The second type is governed primarily by ion dynamics and is called the ion Bernstein wave. However, in the ion Bernstein wave, the electrons contribute a small first order effect in the form of an additional screening (Ichimaru, 1973). These waves have frequencies in excess of the ion cyclotron frequency and propagate between the harmonics of the ion cyclotron frequency ω_{ci}.

The electron and ion Bernstein waves coexist in an electron-ion plasma, when $1 \lesssim \omega_{pe}^2/\omega_{ce}^2 \lesssim 10$ (Fredricks, 1968), and the behaviour of both the electrostatic electron and ion Bernstein waves are qualitatively similar (Crawford, 1965; Fredricks, 1968).

Electrostatic waves propagating exactly perpendicularly to a static magnetic field are generally undamped in non-relativistic Maxwellian theory; however, in the presence of a vanishing magnetic field, wave solutions indicating damping may be observed (Bernstein, 1958). This phenomenon has been analytically investigated by Baldwin and Rowlands (1966) and computationally investigated by Kamimura et al. (1978). Baldwin and Rowlands (1966) investigated the damping mechanism for electron Bernstein waves. The results of Baldwin and Rowlands (1966) illustrated that the individual electron Bernstein waves are not themselves damped; however, in the limit as the magnetic field approaches zero, the Bernstein modes collectively act as a single quasi-mode. It is this quasi-mode which damps according to

the usual damping rate for electrostatic waves in the absence of an applied magnetic field. The damping arises due to phase mixing of an infinite set of closely spaced real frequencies, which are nearly all harmonics of the electron cyclotron frequency. Kamimura et al. (1978) investigated the transport of heat across a plasma caused by the emission and damping of waves propagating perpendicularly to a uniform magnetic field, using two dimensional electrostatic particle-in-cell simulations. Kamimura et al. (1978) computed the autocorrelation function for the electric field spectrum and observed early phase mixing damping, occurring on a time interval small compared to $2\pi/\omega_{ce}$. Phase coherence was found to be re-established each cyclotron period, in the form of a recurrence peak in the autocorrelation function, in agreement with the work carried out by Baldwin and Rowlands (1966).

In the simulations of Kamimura et al. (1978) a single electron species was used with ions forming a neutralising background. Toida et al. (2003), Yoshiya et al. (2004) and Toida et al. (2004) extended the work of Kamimura et al. (1978) and employed particle-in-cell simulations to investigate the damping of ion Bernstein waves in a single and multi-ion species plasma. For the single ion species case, Toida et al. (2003) computed the autocorrelation function, which displayed periodic behaviour on the order of the ion cyclotron period. The recurrence peaks in the autocorrelation function were observed to re-establish and almost return to their initial values, indicating the re-establishment of phase coherence. When multiple ion species were used, however, the recurrence peaks did not return to their initial values (Toida et al., 2003; Yoshiya et al., 2004; Toida et al., 2004).

Being a purely kinetic wave, i.e., Bernstein type waves do not exist in a plasma modelled as a fluid, the dispersion relations of the individual Bernstein modes are sensitive to the plasma particle velocity distributions (Swanson, 2003). Tataronis and Crawford (1970) explored the dispersion characteristics of perpendicularly propagating electron Bernstein waves for a set of electron velocity distributions, including the Maxwellian, ring and spherical velocity distributions. The ring and spherical distributions were found to contain enough free energy to destabilise the electron Bernstein modes under certain conditions. No instability, however, was found for the Maxwellian distribution. The necessary condition to destabilise cyclotron harmonic waves is $\partial f_0/\partial v_\perp > 0$, over some range of $v_\perp$, for the equilibrium velocity distribution f_0 (Tataronis and Crawford, 1970).

Gary et al. (2010) studied the properties of the ion Bernstein instability,

driven by a proton velocity distribution modelled as the difference of two isotropic Maxwellian distributions with different densities and temperatures, i.e., they used a subtracted Maxwellian distribution $f_p(\boldsymbol{v}) = f_1(v) - f_2(v)$, where f_p satisfied the condition for instability, $\partial f_p(v_\perp)/\partial v_\perp > 0$. However, it is important to note that propagation close to 90°, with respect to the magnetic field, was used in their calculations, instead of exactly 90° . This work was motivated by observations in the terrestrial magnetosphere, near the plasma sheet boundary layer, of enhanced field fluctuation spectra (Denton et al., 2010). These fluctuation spectra are believed to be produced by ion Bernstein waves. Lui et al. (2011) performed fully electromagnetic particle-in-cell simulations to study the temporal development of an ion Bernstein instability driven by a proton velocity distribution, with a positive slope in the perpendicular velocity distribution. The subtracted Maxwellian distribution was first used to produce the positive slope, in accordance with earlier work by Gary et al. (2010), to compare simulation results with that from kinetic theory. Good agreement between the simulation results and theory was achieved. Furthermore, the ion shell distribution was used, with finite thermal spread and a cold ion background. The results of the simulations conducted by Lui et al. (2011) resembled the observed fast magnetosonic waves found in different regions of the magnetosphere, consistent with their theoretical model.

Banded emissions, which are naturally occurring electrostatic plasma emissions, are frequently observed in the Earth's magnetosphere [see Kennel and Ashour-Abdalla (1982)]. These emissions occur at frequencies between harmonics of the electron cyclotron frequency and are observed to be most intense near the magnetic equator, suggestive of near perpendicular propagation. Thus, banded emissions are generally attributed to electron Bernstein waves, although alternative interpretations exist (Benson et al., 2001). Enhanced magnetic and electric field fluctuations at frequencies between the ion cyclotron and lower hybrid frequencies, at propagation nearly perpendicular to the magnetic field, are also observed near the equatorial plane of the terrestrial magnetosphere. These enhanced fluctuations were initially referred to as equatorial noise (Russel et al., 1970), but more recently have been termed magnetosonic waves (Perraut et al., 1982; Horne et al., 2000) or more appropriately, for low proton beta $\beta_p \ll 1$, are described by the ion Bernstein instability (Janhunen et al., 2003; Gary et al., 2010).

Crary et al. (2001) carried out large scale, massively parallel, two dimensional electrostatic particle-in-cell simulations, producing bipolar electro-

static structures and, at later times, ion Bernstein waves with peak intensities at frequencies between multiples of the ion cyclotron frequency. The simulations were found to agree with observations made by the FAST spacecraft of such bipolar structures as well as of waves with frequencies between ion cyclotron harmonics (Carlson et al., 1998; Ergun et al., 1998), which were identified as ion Bernstein modes.

Absorption studies of particles in cyclotron motion have shown that plasmas can absorb energy at its cyclotron harmonics. Support for this came when satellite studies of the ionosphere, using pulsed transmitters of variable frequencies, induced resonance phenomena in the plasma, at its cyclotron frequencies, with ringing persisting for many periods after the end of the transmitter pulse. Such sounding experiments were carried out in the ionosphere by sounder space craft such as Alouette (Dougherty and Monaghan, 1966) and analogous experiments were carried out in the magnetosphere by the Radio Plasma Imager (RPI) aboard the IMAGE satellite (Benson et al., 2003). These experiments use an electromagnetic impulse to stimulate short-range plasma wave echoes and plasma emissions known as plasma resonances. The resonances measured by the space craft are believed to be produced by, among other things, a vanishing group velocity Bernstein wave packet, excited by the electromagnetic impulses (Dougherty and Monaghan, 1966). The stimulated electromagnetic resonances have been found to depend on a number of plasma parameters, as well as those of the pump. Thus, they can be used as a diagnostic tool and may provide the local electron density n_e and the magnetic field strength $|\boldsymbol{B}|$. Scales et al. (1997) conducted one dimensional electromagnetic particle-in-cell simulations to investigate the stimulated electromagnetic emission (SEE) produced during ionospheric heating experiments. Scales et al. (1997) used an external oscillating magnetic field to represent the long wavelength electromagnetic pump field in the simulations. The oscillating magnetic field was then varied in frequency and amplitude and the resulting stimulated power spectrum was analysed. Qualitatively similar behaviour between the frequency spectrum from the simulation results and the behaviour of stimulated electromagnetic emission in the ionosphere was observed.

Analytic studies of Bernstein waves have been carried out for plasmas having kappa velocity distributions, e.g., see Mace (2003, 2004) and Henning et al. (2011). However, the works involving simulations mentioned above, and many others not mentioned here, have used either the Maxwellian velocity distribution, loss cone, ring or spherical shell distributions. Presented

below are the results of simulations of electrostatic Bernstein waves of both electron and ion types, where the electron and ion species are modelled by (a) Maxwellian and (b) kappa velocity distributions.

4.2 Dispersion relation for Bernstein waves

4.2.1 The Maxwellian case

The dispersion relation for electrostatic Bernstein waves in a multi-species plasma, where each species is modelled by a Maxwellian velocity distribution, is given by, using the form derived by Mace (2003),

$$1 + \sum_{\alpha} \frac{1}{k^2 \lambda_{D\alpha}^2} \left\{ 1 - {}_2F_2 \left[\frac{1}{2}, 1; 1 + \frac{\omega}{\omega_{c\alpha}}, 1 - \frac{\omega}{\omega_{c\alpha}}; -2\lambda_\alpha \right] \right\} = 0, \tag{4.1}$$

where the sum is over each particle species represented by α, k is the wavenumber, ${}_2F_2[\cdots]$ is the generalised hypergeometric function, $\omega_{c\alpha} = q_\alpha B/m_\alpha$ is the cyclotron frequency for species α and

$$\lambda_\alpha = \frac{k_\perp^2 v_{th\alpha}^2}{\omega_{c\alpha}^2}. \tag{4.2}$$

The alternate, and more familiar, form of the dispersion relation for electrostatic Bernstein waves in a Maxwellian plasma is given by (Krall and Trivelpiece, 1973)

$$1 - 2 \sum_{\alpha} \frac{1}{k^2 \lambda_{D\alpha}^2} \sum_{n=1}^{\infty} \exp(-\lambda_\alpha) I_n(\lambda_\alpha) \frac{n^2 \omega_{c\alpha}^2}{\omega^2 - n^2 \omega_{c\alpha}^2} = 0, \tag{4.3}$$

where $I_n()$ is the modified Bessel function of order n. Stix (1992, p. 295) defined the function $\varphi(q, \lambda)$ such that

$$\varphi(q, \lambda) = 2 \sum_{n=1}^{\infty} \exp(-\lambda) I_n(\lambda) \frac{n^2}{q^2 - n^2}, \tag{4.4}$$

where $q = \omega/\omega_c$, whose expansion in ascending powers of λ is given by (Stix, 1992, p. 295)

$$\varphi(q,\lambda) = \frac{\lambda}{(q^2-1^2)} + \frac{1\cdot 3\lambda^2}{(q^2-1^2)(q^2-2^2)} + \frac{1\cdot 3\cdot 5\lambda^3}{(q^2-1^2)(q^2-2^2)(q^2-3^2)} + \cdots . \tag{4.5}$$

In terms of $\varphi(q,\lambda)$, Equation (4.3) can be written as

$$1 - \sum_\alpha \frac{1}{k^2\lambda_{D\alpha}^2}\varphi(q_\alpha,\lambda_\alpha) = 0. \tag{4.6}$$

It is easily shown that the function defined by Stix (1992), $\varphi(q,\lambda)$ in Equation (4.4), is precisely ${}_2F_2[1/2,1;1+q,1-q;-2\lambda]-1$, thus illustrating the equivalence of the dispersion relations Equations (4.1) and (4.6) [or Equation (4.3)]. That is, recalling the definition of ${}_2F_2$ (Mace, 2003)

$${}_2F_2\left[\frac{1}{2},1;1+q,1-q;-2\lambda\right] = \sum_{n=0}^{\infty}\frac{(1/2)_n(1)_n}{(1+q)_n(1-q)_n}\frac{(-2\lambda)^n}{n!},$$

where the Pochhammer symbol $(a)_n$ is given by (Mace, 2003)

$$(a)_0 = 1, \qquad (a)_n = a(a+1)(a+2)\cdots(a+n-1) = \frac{\Gamma(a+n)}{\Gamma(a)},$$

and as shown in Mace (2003)

$$(1+x)_n(1-x)_n = \begin{cases} 1, & n=0 \\ (1^2-x^2)(2^2-x^2)(3^2-x^2)\cdots(n^2-x^2), & n>0. \end{cases}$$

Using the last three equations it is an easy exercise to show that

$$
\begin{aligned}
&{}_2F_2\left[\frac{1}{2},1;1+q,1-q;-2\lambda\right] \\
&\quad = 1+\frac{\lambda}{(q^2-1^2)}+\frac{1\cdot 3\lambda^2}{(q^2-1^2)(q^2-2^2)}+\frac{1\cdot 3\cdot 5\lambda^3}{(q^2-1^2)(q^2-2^2)(q^2-3^2)},
\end{aligned}
$$

which should be compared to the expansion of $\varphi(q,\lambda)$, Equation (4.5) above. We thus deduce that

$$
\varphi(q,\lambda) =_2 F_2\left[\frac{1}{2},1;1+q,1-q;-2\lambda\right]-1,
$$

and the equivalence of Equations (4.1) and (4.6) is established.

Now, the cold plasma approximation to the dispersion relation in Equation (4.6) is obtained by letting $v_{th\alpha}\to 0$, and keeping the lowest order term in the expansion of $\varphi(q_\alpha,\lambda_\alpha)$, Equation(4.5), where λ_α is given in Equation (4.2). The higher order terms in the expansion, Equation (4.5), vanish because $v_{th\alpha}\to 0$. Thus, for an electron-ion plasma, Equation (4.6), in the limit $v_{th\alpha}\to 0$, becomes

$$
\begin{aligned}
1-\frac{1}{k^2\lambda_{De}^2}\frac{\lambda_e}{(\omega^2/\omega_{ce}^2-1)}-\frac{1}{k^2\lambda_{Di}^2}\frac{\lambda_i}{(\omega^2/\omega_{ci}^2-1)} &= 0 \\
1-\frac{\omega_{pe}^2}{\omega^2-\omega_{ce}^2}-\frac{\omega_{pi}^2}{\omega^2-\omega_{ci}^2} &= 0, \qquad (4.7)
\end{aligned}
$$

where we have used Equation (4.2) and $v_{th\alpha}=\lambda_{D\alpha}\omega_{p\alpha}$ in the last step of Equation (4.7). The solutions to Equation (4.7) are the lower and upper hybrid frequencies. The upper hybrid frequency is well in excess of ω_{ci} and ω_{pi}. Hence, neglecting the contribution from the ions in Equation (4.7) we obtain

$$
\omega_{uh}^2=\omega_{pe}^2+\omega_{ce}^2, \qquad (4.8)
$$

where ω_{uh} denotes the upper hybrid frequency. On the other hand, assuming $\omega_{ci}^2 \ll \omega^2 \ll \omega_{ce}^2$, we obtain the lower hybrid frequency solution ω_{lh}, given via

$$\frac{1}{\omega_{lh}^2} = \frac{1}{\omega_{ce}\omega_{ci}} + \frac{1}{\omega_{pi}^2}. \tag{4.9}$$

The hybrid frequencies are important to the analysis of the dispersion characteristics of the electron and ion Bernstein waves, as they provide a dividing line that separates regions in which the Bernstein waves show qualitatively different dispersion relations (Puri et al., 1973). This will be shown later.

4.2.2 The kappa case

The dispersion relation for electrostatic Bernstein waves in a multi-species plasma, where each plasma species is modelled by a kappa velocity distribution is given by (Mace, 2003)

$$\begin{aligned} 1 + \sum_{\alpha} \frac{1}{k^2 \lambda_{\kappa\alpha}^2} \Bigg\{ & 1 - {}_2F_3\left[1, \frac{1}{2}; \frac{1}{2} - \kappa_\alpha, 1 + \frac{\omega}{\omega_{c\alpha}}, 1 - \frac{\omega}{\omega_{c\alpha}}; 2\lambda_\alpha^{'}\right] \\ & + \pi^{1/2} \frac{\omega}{\omega_{c\alpha}} \csc\left(\pi \frac{\omega}{\omega_{c\alpha}}\right) \frac{\Gamma(\kappa_\alpha + 1)\Gamma(1/2 - \kappa_\alpha)}{\Gamma(\kappa_\alpha + 3/2 + \omega/\omega_{c\alpha})\Gamma(\kappa_\alpha + 3/2 - \omega/\omega_{c\alpha})} \\ & \times (2\lambda_\alpha^{'})^{\kappa_\alpha + 1/2} {}_1F_2\left[\kappa_\alpha + 1; \kappa_\alpha + \frac{3}{2} + \frac{\omega}{\omega_{c\alpha}}, \kappa_\alpha + \frac{3}{2} - \frac{\omega}{\omega_{c\alpha}}; 2\lambda_\alpha^{'}\right] \Bigg\} = 0, \end{aligned} \tag{4.10}$$

where the sum is over each plasma species represented by α, ${}_2F_3[\cdots]$ and ${}_1F_2[\cdots]$ are the generalised hypergeometric functions and

$$\lambda_\alpha^{'} = \left(\kappa_\alpha - \frac{3}{2}\right)\lambda_\alpha = \left(\kappa_\alpha - \frac{3}{2}\right) k_\perp^2 \frac{v_{th\alpha}^2}{\omega_{c\alpha}^2}. \tag{4.11}$$

Mace (2003) demonstrated that the expansion of the dispersion relation, Equation (4.10), to $O[(2\lambda^{'})^2]$, when both plasma species, in an electron-ion

plasma, are modelled by kappa velocity distributions with $\kappa > 5/2$, results in the simplified approximate form of the dispersion relation, Equation (4.10),

$$1 + \sum_{\alpha} \frac{1}{k^2 \lambda_{\kappa\alpha}^2} \left\{ 1 - {}_2F_3 \left[1, \frac{1}{2}; \frac{1}{2} - \kappa_\alpha, 1 + \frac{\omega}{\omega_{c\alpha}}, 1 - \frac{\omega}{\omega_{c\alpha}}; 2\lambda_\alpha^{'} \right] \right\} = 0, \quad (4.12)$$

where (Mace, 2003)

$$\begin{aligned} &{}_2F_3 \left[1, \frac{1}{2}; \frac{1}{2} - \kappa_\alpha, 1 + \frac{\omega}{\omega_{c\alpha}}, 1 - \frac{\omega}{\omega_{c\alpha}}; 2\lambda_\alpha^{'} \right] \\ &= 1 + \left(\frac{\kappa_\alpha - 3/2}{\kappa_\alpha - 1/2} \right) \frac{k^2 v_{th\alpha}^2}{\omega^2 - \omega_{c\alpha}^2} + 3 \left(\frac{\kappa_\alpha - 3/2}{\kappa_\alpha - 1/2} \right) \frac{k^4 v_{th\alpha}^4}{(\omega^2 - \omega_{c\alpha}^2)(\omega^2 - 4\omega_{c\alpha}^2)} + O[(2\lambda_\alpha^{'})^3]. \end{aligned} \quad (4.13)$$

Substituting Equation (4.13) into Equation (4.12) and ignoring thermal effects, i.e., letting $v_{th\alpha} \to 0$, leads to

$$1 - \frac{\omega_{pe}^2}{\omega^2 - \omega_{ce}^2} - \frac{\omega_{pi}^2}{\omega^2 - \omega_{ci}^2} = 0. \quad (4.14)$$

Equation (4.14) is identical to Equation (4.7). Thus, Equation (4.14) has the upper and lower hybrid solutions, Equations (4.8) and (4.9), respectively. This illustrates that the hybrid frequencies are unaffected by the kappa distribution, i.e., the hybrid frequencies are identical in Maxwellian and kappa plasmas. Since qualitatively similar general behaviour of the Bernstein waves in Maxwellian and kappa plasmas is expected (Bernstein, 1958; Crawford, 1965; Fredricks, 1968; Mace, 2004), the hybrid frequencies again separate different types of Bernstein wave dispersion behaviour in the kappa plasma.

4.3 PIC simulation for a Maxwellian plasma

4.3.1 Simulation run parameters

As in the simulations carried out for the ion-acoustic instability, described in Chapter 3 (p. 39), all simulation run parameters considered in this chapter are given with reference to those for the electron species. Times are given with reference to the reciprocal of the electron plasma frequency, $t' = \omega_{pe}t$, lengths are given with reference to the electron Debye length, $x' = x/\lambda_{De}$ and velocities are given with reference to the electron thermal velocity, $v' = v/v_{the}$ (where primed variables denote simulation values and unprimed variables denote ordinary S.I. values).

The aim of this chapter is to investigate electrostatic Bernstein waves produced in a plasma containing no free energy sources. The simulation results presented in this section are those which used run parameters describing a plasma consisting of two stationary species, electrons and ions, both modelled by Maxwellian velocity distributions, and in thermal equilibrium, i.e., with equal temperatures $T_e = T_i$. A uniform, static magnetic field with magnitude specified by $B_0 = \omega_{ce}m_e/e$ is present and is directed perpendicular to the direction of the x axis.

In our simulation, we use the reduced ion-to-electron mass ratio of $m_i/m_e = 100$. This allows sufficient separation of the electron and ion time scales, while still allowing the dynamics of both plasma species to be tracked without resorting to prohibitively long simulation runs. A summary of the plasma species run parameters are given in Table 4.1.

In our simulations we use $\omega_{pe}/\omega_{ce} = 2$. With our choice of normalisation scheme, see Appendix C, the magnitude of the magnetic field present in the plasma is $B_0/(\omega_{pe}m_e/e) = 0.5$. The simulation was run for a time long enough, up to the time $\omega_{pe}t = 16000$, to allow ion Bernstein waves to be resolved. This simulation run duration enables the ions to perform about 13 cyclotron orbits. In a statistical investigation of banded magnetospheric emissions, conducted by Labelle et al. (1999), the ratio $\omega_{pe}/\omega_{ce} = 2$ is, however, given as the lower limit in a number of sampled observations of banded magnetospheric emission data, observed by the Active Magnetospheric Particle Tracer Experiment/Ion Release Module (AMPTE/IRM) [see Figure 6 of Labelle et al. (1999)].

Electron species	Ion species
4194304 particles	4194304 particles
$\omega_{pe} = 1$	$\omega_{pi} = 0.1$
$\omega_{ce} = 0.5$	$\omega_{ci} = 0.005$
$q/m_e = -1$	$q/m_i = 0.01$
$v_{the} = 1$	$v_{thi} = 0.1$
$v_{drift} = 0$	$v_{drift} = 0$

Table 4.1: The electrostatic Bernstein wave simulation run parameters.

The simulation employs a box length of $L = 512\lambda_{De}$ with a cell size of $\Delta x = 0.125\lambda_{De}$, corresponding to a total of 4096 cells. The time step Δt used in the simulation was chosen to satisfy $\omega_{pe}\Delta t = 0.1$ and the simulation was run for a total of 160000 time steps, corresponding to the time $\omega_{pe}t = 16000$.

4.3.2 Results of the simulation run

Figure 4.1 illustrates the electric field (wave) intensity as a function of ω and k, over the range $0 \leq \omega/\omega_{ce} \leq 5.5$ and $0 \leq k\lambda_{De} \leq 4.5$. As before, the electric field, due to our choice of normalisation scheme, is $E^{'} = E_x/(n_{0e}T_e/\epsilon_0)^{1/2}$, see Appendix C. The dispersion relation for Bernstein waves, generated by evaluating Equation (4.1) using the software package MATHEMATICA, is superimposed and displayed in Figure 4.1 (b). The maximum electric field intensities, $10^7 < \epsilon_0 E^2/n_{0e}T_e < 10^{12}$ (corresponding to the red, orange and yellow areas) are observed to agree well with the linear dispersion relation, Equation (4.1). The regions of enhanced levels of wave activity are observed to occur between frequency bands bound by harmonics of the electron cyclotron frequency, as seen in Figure 4.1. Thus, these waves are of the electron Bernstein type.

While a plot of ω/ω_{ce} versus kR_{Le} may provide a physically more revealing view of Bernstein wave behaviour, our choice to plot ω/ω_{ce} versus $k\lambda_{De}$ is one of convenience and for consistency with the other dispersion curves in this thesis. Since $kR_{Le} = (\omega_{pe}/\omega_{ce})k\lambda_{De}$ and $\omega_{pe}/\omega_{ce} = 2$ in our case, the kR_{Le} dependence can be gleaned by multiplying the $x-$axis values by 2. When this is done it is seen that the peak frequency of the Bernstein wave in the upper hybrid frequency band occurs at $kR_{Le} \approx 1$.

As $k\lambda_{De}$ increases, the regions of strongest wave activity in Figure 4.1 are

observed to trace out five distinct paths in $\omega - k$ space. These correspond to the first five electron Bernstein modes, with the lowest order electron Bernstein mode having a frequency $\omega/\omega_{ce} = 2$ at vanishing $k\lambda_{De}$. The broad area of enhanced wave activity levels with $10^7 < \epsilon_0 E^2/n_{0e}T_e < 10^{11}$ below the lowest order electron Bernstein wave is attributed to waves of the ion Bernstein type, which will be discussed later.

Distinctly different electrostatic electron Bernstein wave behaviour is known to occur for waves with frequencies, respectively, below and above the upper hybrid frequency, Equation (4.8), (Bernstein, 1958; Crawford, 1965; Tataronis and Crawford, 1970; Puri et al., 1973). Given our choice of run parameters, see Table 4.1, the upper hybrid frequency for the current simulation is $\omega_{uh}/\omega_{ce} = 2.23$.

The strongest wave activity below the upper hybrid frequency is observed to agree well with the Bernstein mode having the frequency $\omega/\omega_{ce} = 2$ at vanishing $k\lambda_{De}$. As $k\lambda_{De}$ increases, the intensity gradually decreases while the frequency asymptotically approaches the first electron cyclotron harmonic. This decrease in frequency of enhanced wave activity levels, from $\omega = 2\omega_{ce} \rightarrow \omega_{ce}$ is monotonic, i.e., no frequency peaks are observed over the whole $k\lambda_{De}$ range, and the entire intraharmonic range is covered in an asymptotic sense, i.e., enhanced wave activity occurs at all frequencies between harmonics of the electron cyclotron frequency, over the range of $k\lambda_{De}$.

The strongest wave activity having frequencies above the upper hybrid frequency is also seen to agree well with the linear Bernstein mode dispersion relation, Equation (4.1), as seen in Figure 4.1 (b). Each mode is observed to approach a harmonic of the electron cyclotron frequency, $\omega = n\omega_{ce}$, at vanishing $k\lambda_{De}$. Enhanced levels of wave activity here are observed to occur at frequencies increasing to a local maximum within the intraharmonic range, at an intermediate $k\lambda_{De}$ value. Beyond this maximum, the regions of enhanced wave activity are observed to occur at frequencies asymptotically approaching the harmonic on which the mode started, i.e., $\omega = n\omega_{ce}$. The frequencies spanned by the strongest wave activity here do not cover the entire intraharmonic range and are also observed to occupy a diminishing range of frequencies as the order n of the wave increases [compare the frequency range spanned by the wave with $\omega/\omega_{ce} = 3$, with that of the wave with $\omega/\omega_{ce} = 5$, at vanishing $k\lambda_{De}$, in Figure 4.1]. The maximum frequency attained between each electron cyclotron harmonic corresponds to the con-

dition of vanishing group velocity, i.e., $\mathrm{d}\omega/\ \mathrm{d}k = 0$. The significance of this will be discussed later in Section 4.4.2.

For the mode lying within the upper hybrid frequency band, i.e., the wave with frequencies between $2 < \omega/\omega_{ce} < 3$ in Figure 4.1, the strongest wave activity is observed to have the frequency $\omega_{uh}/\omega_{ce} = 2.23$ at vanishing $k\lambda_{De}$. Enhanced levels of wave activity are then observed to occur at frequencies increasing to $\omega/\omega_{ce} \approx 2.5$ at $k\lambda_{De} \approx 0.25$, and thereafter for $k\lambda_{De} > 0.25$, at frequencies decreasing asymptotically to the harmonic of the electron cyclotron frequency directly below the upper hybrid frequency, i.e., $\omega/\omega_{ce} = 2$.

Also evident in Figure 4.1 are weaker excitations at approximately twice the frequency of the main (stronger) Bernstein modes. We believe these to arise due to nonlinear effects that produce harmonics of the original wave frequency. However, whether these are of physical origin or are as a result of some nonlinearity or aliasing in the numerical techniques is unknown at present.

Figure 4.2 illustrates the electric field intensity, as a function of ω and k, over the range $0 \leq \omega/\omega_{ce} \leq 0.18$ and $0 \leq k\lambda_{De} \leq 1.05$, i.e., the region below the lowest order electron Bernstein wave. The dispersion relation for Bernstein waves, generated again by evaluating Equation (4.1), over this range, using the software package MATHEMATICA, is superimposed and displayed in Figure 4.2 (b). The maximum intensities, $10^7 < \epsilon_0 E^2/n_{0e}T_e < 10^{11}$ (corresponding to the red and orange areas) are seen to agree well with the dispersion relation, Equation (4.1), as well, in this low frequency range [see Figure 4.2 (b)].

In our simulation run we employed the ion-to-electron mass ratio $m_i/m_e = 100$, resulting in an ion cyclotron frequency of $\omega_{ci} = 0.01\omega_{ce}$. In Figure 4.2, the regions of strongest wave activity are observed to occur at frequencies between harmonics of $\omega_{ci} \equiv 0.01\omega_{ce}$, indicative of ion Bernstein waves.

The enhanced levels of wave activity are observed to trace out seventeen separate paths in $\omega - k$ space as $k\lambda_{De}$ increases, as seen in Figure 4.2. These are the first seventeen ion Bernstein waves, with the lowest order wave having $\omega = 0.02\omega_{ce} \equiv 2\omega_{ci}$ at vanishing $k\lambda_{De}$.

Detailed kinetic theory suggests that the behaviour of the ion Bernstein waves are qualitatively similar to the electron Bernstein waves (Crawford,

(a)

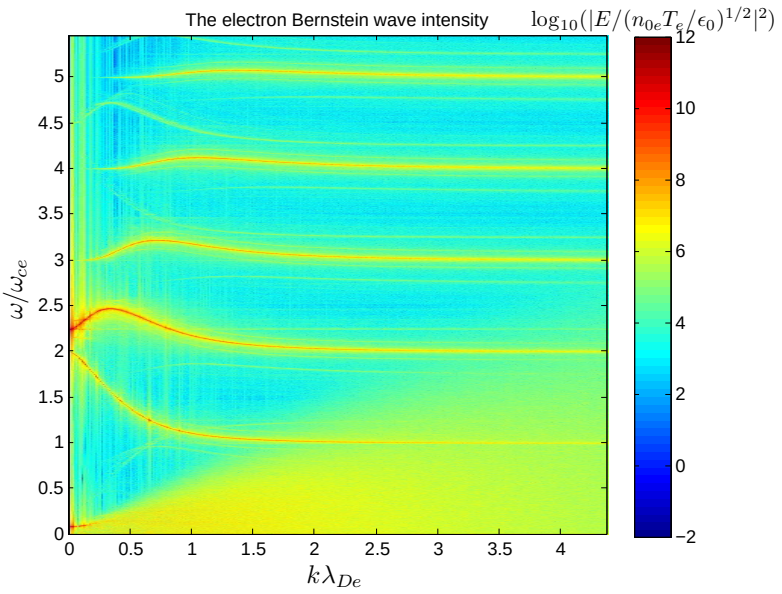

(b)

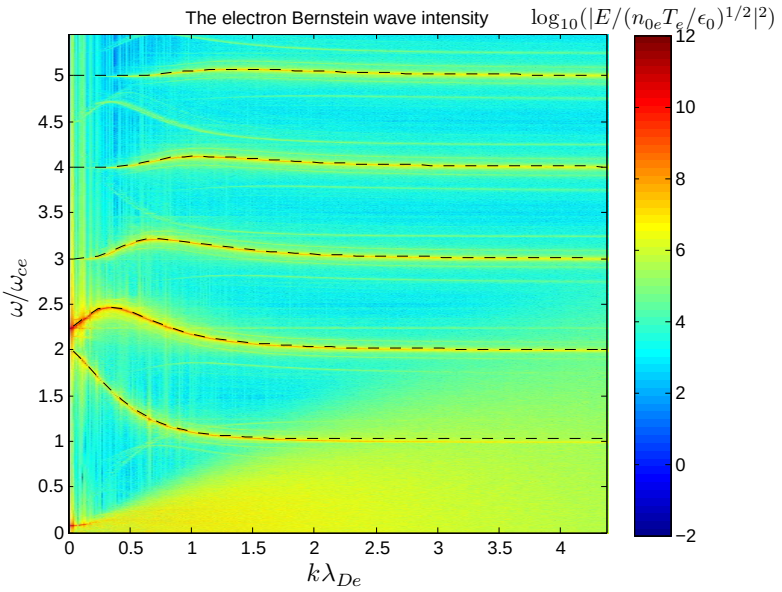

Figure 4.1: (a) The electron Bernstein wave intensity for a Maxwellian plasmas with (b) the dispersion relation for electron Bernstein waves, Equation (4.1), superimposed.

1965; Fredricks, 1968). Thus, as with the electrostatic electron Bernstein waves, described above, qualitatively different electrostatic ion Bernstein wave behaviour is expected to occur above and below the dividing line which now lies at the lower hybrid frequency, Equation (4.9). With our choice of simulation run parameters the value of the lower hybrid frequency is $\omega_{lh}/\omega_{ce} = 0.09$.

For the ion Bernstein waves with frequencies below the lower hybrid frequency, seen in Figure 4.2, the areas of strongest wave activity are observed to approach frequencies equal to a harmonic of the ion cyclotron frequency $\omega = n\omega_{ci}$ (where $n = 2, 3, \cdots, 8$), at vanishing $k\lambda_{De}$. As $k\lambda_{De}$ is increased, enhanced levels of wave activity are observed at frequencies decreasing monotonically to the ion cyclotron harmonic below the one at which it started, i.e., $\omega = (n-1)\omega_{ci}$.

In Figure 4.2, the areas of strongest wave activity at frequencies in excess of the lower hybrid frequency are observed to agree well with the ion Bernstein modes. These modes approach a harmonic of the ion cyclotron frequency $\omega = n\omega_{ci}$ (where $n = 9, 10, \cdots, 17$), at vanishing $k\lambda_{De}$. As $k\lambda_{De}$ increases, the frequencies of enhanced wave activity increase to a maximum value within the intraharmonic band, at an intermediate $k\lambda_{De}$ value, after which they decrease to the harmonic at which they started, $\omega = n\omega_{ci}$, at large $k\lambda_{De}$.

Figure 4.3 illustrates the time evolution of the the electric field energy E_f/T_e [Figure 4.3 (a)], kinetic energy of the electron species E_e/T_e [Figure 4.3 (b)], kinetic energy of the ion species E_i/T_e [Figure 4.3 (c)] and the sum of these energies E_{tot}/T_e [Figure 4.3 (d)], for the Maxwellian plasma. Energies here are given with reference to the initial electron thermal energy, as they were in the simulations carried out in Chapter 3 (p. 39).

The simulation run carried out and presented in this section was for a plasma with no externally perturbing forces or free energy to drive an instability. By virtue of the thermal fluctuations of the plasma particles, stable electrostatic Bernstein waves were produced [see Figure 4.3 (a)].

As expected, the electric field energy as well as the kinetic energies of the ion and electron species remain appropriately level during the simulation run, as seen in Figures 4.3 (a) to (c), respectively. This is indicative of a plasma in equilibrium. The observed fluctuations in the energies are produced by the natural random thermal fluctuations of the discrete simulation particles.

(a) (b)

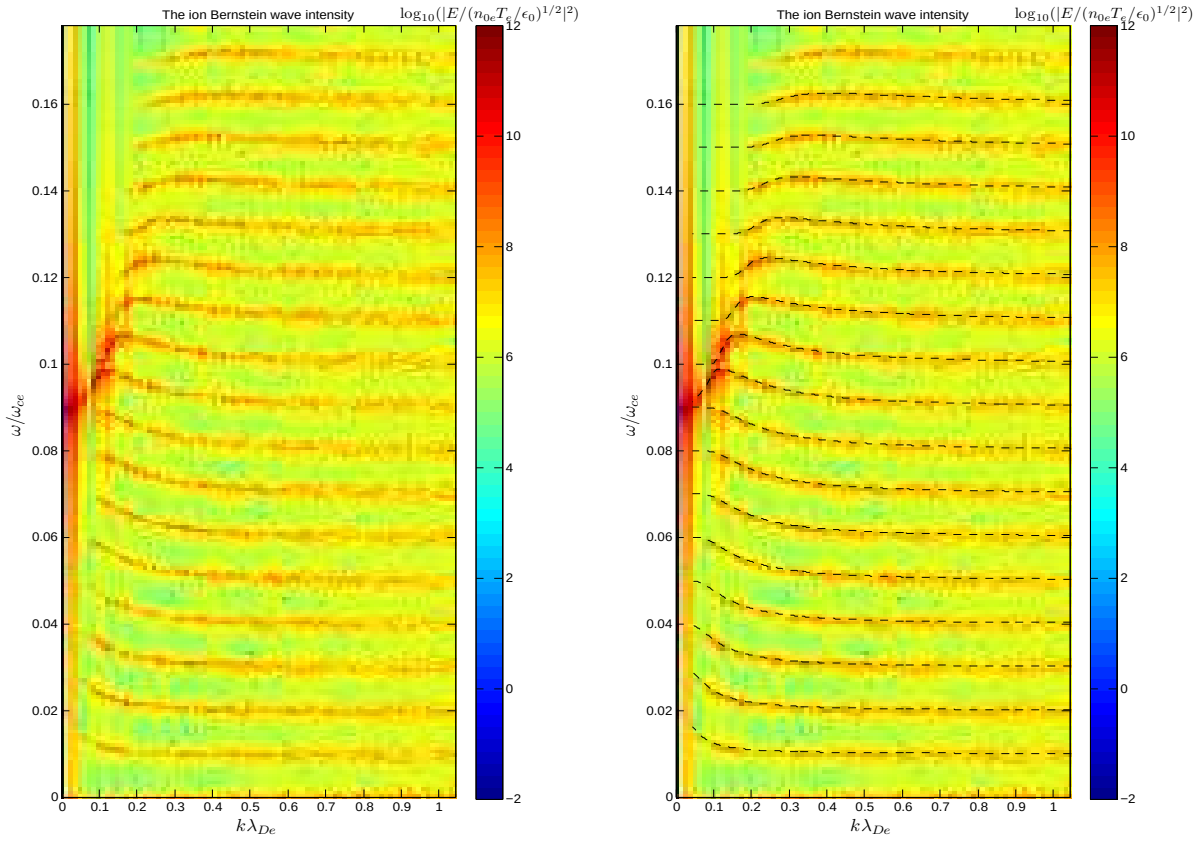

Figure 4.2: (a) The ion Bernstein wave intensity for a Maxwellian plasma with (b) the dispersion relation for ion Bernstein waves, Equation (4.1), superimposed.

Importantly, the total energy is conserved throughout the simulation run to within the error of the simulation techniques, as seen in Figure 4.3 (d), assuring the validity of the simulation results.

4.4 PIC simulation for a kappa plasma

4.4.1 Simulation run parameters

Presented in this section are the results of the simulation run for the plasma where the plasma electrons and ions are modelled by kappa velocity distributions, having equal kappa indices $\kappa_e = \kappa_i = 2$. To investigate the effects the kappa distribution has on the dispersion behaviour of the Bernstein waves, we use identical species parameters to those used in the Maxwellian simulation run, see Table 4.1 (p. 84).

The simulation uses a box length of $L = 512\lambda_{De}$ with 4096 cells, as well as a time step Δt satisfying $\omega_{pe}\Delta t = 0.1$, for 160000 time steps, identical to the Maxwellian simulation run parameters.

4.4.2 Results of the simulation run

Figure 4.4 illustrates the electric field (wave) intensity for the kappa simulation run, over the range $0 \leq \omega/\omega_{ce} \leq 5.5$ and $0 \leq k\lambda_{De} \leq 4.5$. The dispersion curves for Bernstein waves, generated by evaluating Equation (4.10) using the software package MATHEMATICA, is superimposed and displayed Figure 4.4 (b). The maximum electric field intensities here, $10^7 < \epsilon_0 E^2/n_{0e}T_e < 10^{12}$, i.e., areas of red, orange and yellow in Figure 4.4, are observed to agree well with the analytical dispersion curves, Equation (4.10), [see Figure 4.4 (b)]. Since the maximum intensities are observed to occur between frequencies bounded by harmonics of ω_{ce}, we identify these as electron Bernstein waves.

The behaviour of the electron Bernstein waves here are observed to be qualitatively similar to those in the Maxwellian plasma, as expected (Mace, 2003, 2004), compare Figure 4.4 with that of Figure 4.1 (p. 87). As $k\lambda_{De}$ increases, the regions of strongest wave activity are observed to trace out five separate paths, in $\omega - k$ space, corresponding to the first five electron

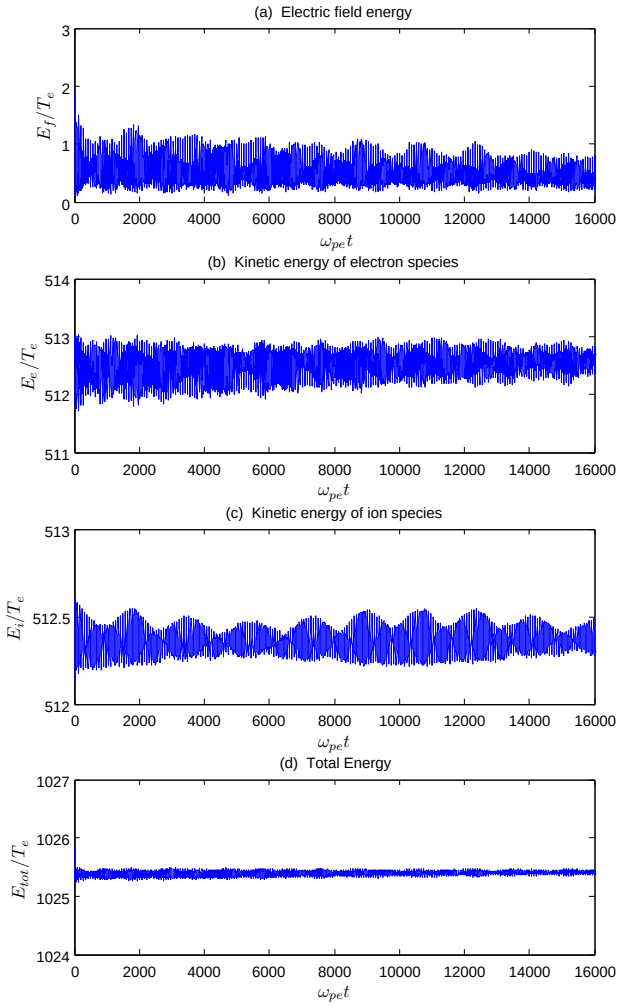

Figure 4.3: The time evolution of (a) the electric field energy E_f/T_e, (b) kinetic energy of the electron species E_e/T_e, (c) kinetic energy of the ion species E_i/T_e and (d) the sum of these energies $E_{\rm tot}/T_e$, for the Maxwellian plasma.

Bernstein waves. The distinction between the different types of behaviour of electrostatic electron Bernstein wave, here, is also defined at the upper hybrid frequency, where the value of the upper hybrid frequency is equivalent to that for the Maxwellian plasma described previously, i.e., $\omega_{uh}/\omega_{ce} = 2.23$. Similar to the Maxwellian simulation run described in Section 4.3 (p. 83), the high intensity region, with $10^7 < \epsilon_0 E^2/n_{0e}T_e < 10^{11}$, below the lowest order electron Bernstein wave in Figure 4.4, is attributed to ion Bernstein waves, which will be discussed later.

For the electron Bernstein wave propagating below the upper hybrid frequency in Figure 4.4, the areas of strongest wave activity are observed at $\omega/\omega_{ce} = 2$, for vanishing $k\lambda_{De}$. The intensity levels of the wave gradually decrease as $k\lambda_{De}$ increases, with the frequencies decreasing monotonically to $\omega/\omega_{ce} = 1$.

Strong wave activity in the upper hybrid frequency band occurs at the upper hybrid frequency, $\omega_{uh}/\omega_{ce} = 2.23$, at vanishing $k\lambda_{De}$, and increases to $\omega/\omega_{ce} \approx 2.4$ at $k\lambda_{De} \approx 0.5$. As $k\lambda_{De}$ increases further, $k\lambda_{De} > 0.5$, the intensity of the wave gradually decreases and the frequencies decrease to $\omega/\omega_{ce} = 2$, as seen in Figure 4.4.

For the electron Bernstein waves propagating above the upper hybrid frequency in Figure 4.4, the regions of strongest wave activity are observed to agree well with the electron Bernstein modes. These approach a harmonic of the electron cyclotron frequency $\omega = n\omega_{ce}$ (where $n = 3, 4, 5$), for vanishing $k\lambda_{De}$. The frequencies then rise to a local maximum between the electron cyclotron harmonics, at an intermediate $k\lambda_{De}$ value, after which they decrease to the cyclotron harmonic on which the mode started, $\omega = n\omega_{ce}$, at large $k\lambda_{De}$.

Figure 4.5 illustrates the dispersion relations for electron Bernstein waves in the Maxwellian plasma, Equation (4.1), and the kappa plasma, Equation (4.10). Although the electron Bernstein waves exhibited similar qualitative dispersion behaviour, differences in their dispersion characteristics are observed.

For the electron Bernstein wave below the upper hybrid frequency, the low value of kappa gives rise to a weak dependence on wavenumber and a slower frequency fall off to the harmonic below, compared to the Maxwellian. All frequencies in the entire intraharmonic band are still, however, occupied in both cases, compare the bottom curves in Figure 4.5.

(a)

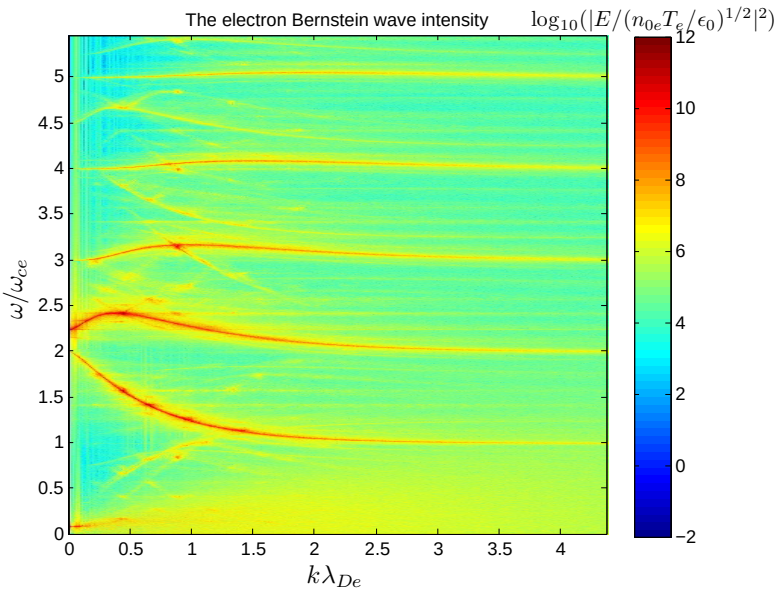

(b)

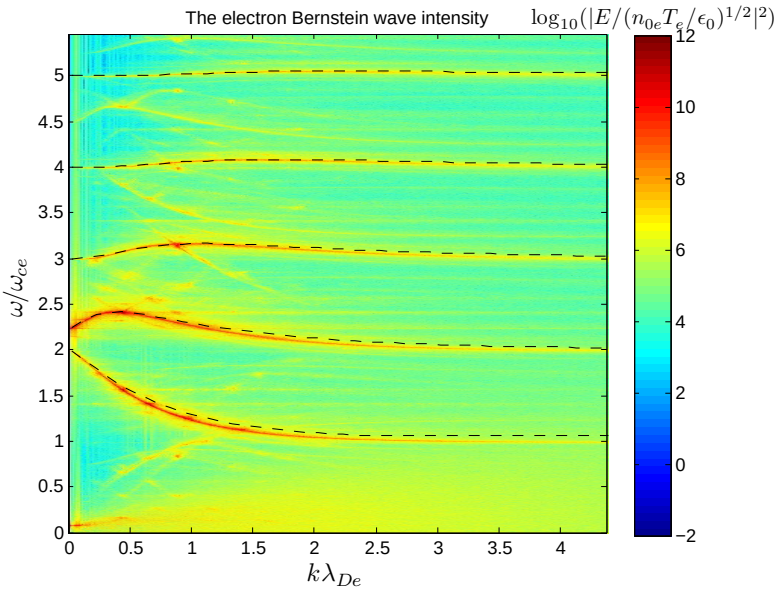

Figure 4.4: (a) The electron Bernstein wave intensity in the kappa plasma with (b) the dispersion relation for Bernstein waves, Equation (4.10), superimposed.

The frequencies spanned by the waves propagating at, and above, the upper hybrid frequency, are observed to occupy a diminished range above the nearest electron cyclotron harmonic for the kappa plasma, compared to the Maxwellian [see the top four curves in Figure 4.5]. The frequency peaks for these waves are also observed to shift to higher $k\lambda_{De}$ values in the kappa plasma. This is clearly seen for the wave in the upper hybrid frequency band, which had its peak frequency at $k\lambda_{De} \approx 0.5$ in the kappa plasma and $k\lambda_{De} \approx 0.25$ in the Maxwellian plasma [see Figure 4.5].

Figure 4.6 illustrates the electric field intensity, as a function of ω and k, over the range $0 \leq \omega/\omega_{ce} \leq 0.18$ and $0 \leq k\lambda_{De} \leq 1.05$. The dispersion relation for Bernstein waves, generated again by evaluating Equation (4.10) using the software package MATHEMATICA, is superimposed and displayed in Figure 4.6 (b). Due to the evaluation of the dispersion relation, Equation (4.10), for this frequency range, at $k\lambda_{De} > 0.6$, producing results which were in error, i.e., fluctuating dispersion curves, even when using a precision of up to 500 digits, the dispersion relation was only evaluated up to $k\lambda_{De} = 0.6$.

The maximum intensities in this frequency range, $10^7 < \epsilon_0 E^2/n_{0e}T_e < 10^{11}$, i.e., the red, orange and yellow regions, are seen to agree well with the dispersion relation, Equation (4.10), as seen in Figure 4.6 (b) and we identify these as the ion Bernstein modes.

The first seventeen ion Bernstein waves are displayed in Figure 4.6, where the lowest order ion Bernstein wave is observed to occur at $\omega = 0.02\omega_{ce} = 2\omega_{ci}$, at vanishing $k\lambda_{De}$. The ion Bernstein wave behaviour here is qualitatively similar to that of the Maxwellian plasma, compare Figure 4.2 (p. 89) with that of Figure 4.6, and the lower hybrid frequency for the kappa plasma equals that for the Maxwellian plasma, i.e., $\omega_{lh}/\omega_{ce} = 0.09$.

As with the Maxwellian plasma, the ion Bernstein waves below the lower hybrid frequency exhibit regions of strongest wave activity at frequencies equal to a harmonic of the ion cyclotron frequency $\omega = n\omega_{ci}$ (where $n = 2, 3, \cdots, 8$) at vanishing $k\lambda_{De}$ [see Figure 4.6]. The frequencies are then observed to decrease monotonically to the ion cyclotron directly below, i.e., $\omega = (n-1)\omega_{ci}$, as $k\lambda_{De}$ increases.

The strongest wave activity above the lower hybrid frequency is observed to agree well with the ion Bernstein modes approaching a harmonic of the ion cyclotron frequency, $\omega = n\omega_{ci}$ (where $n = 9, 10, \cdots, 17$), at vanishing $k\lambda_{De}$. High levels of wave activity then increase to a local maximum between

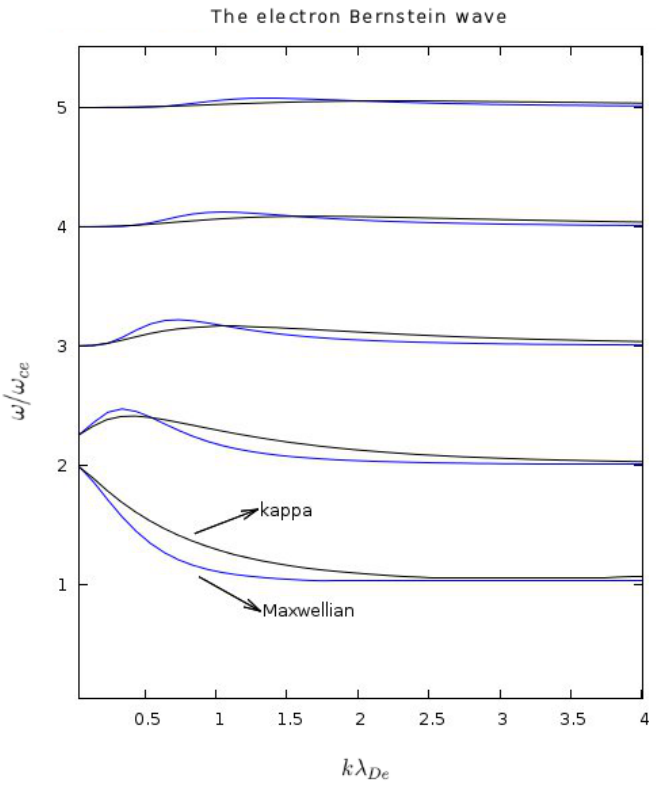

Figure 4.5: Comparison of the electron Bernstein dispersion relations for waves in Maxwellian and kappa plasmas, Equations (4.1) and (4.10), respectively.

ion cyclotron harmonics, at an intermediate $k\lambda_{De}$ value. After attaining the local maximum, the frequencies decrease to the harmonic on which it started $\omega = n\omega_{ci}$, for large $k\lambda_{De}$.

Figure 4.7 illustrates the dispersion relations for the ion Bernstein waves in the Maxwellian plasma, Equation (4.1), and the kappa plasma, Equation (4.10). Differences in the dispersion characteristics of the ion Bernstein modes are observed when comparing each case. These differences in the ion Bernstein mode behaviours are qualitatively similar to the differences observed for the electron Bernstein modes, compare Figures 4.5 and 4.7.

Below the lower hybrid frequency, $\omega_{lh}/\omega_{ce} = 0.09$, the waves are observed to have a slower frequency fall off to the ion cyclotron harmonic directly below it in the kappa plasma (compare the bottom eight curves in Figure 4.7). This trend is also observed for the wave at the lower hybrid frequency. The frequency range spanned by the waves above the lower hybrid frequency is observed to be condensed for the kappa plasma, and the location of the points of vanishing group velocity are observed to move to higher $k\lambda_{De}$ values compared to the Maxwellian plasma.

The points of zero Bernstein wave group velocity, have been cited as being important to the long time echoes observed in ionospheric topside sounder experiments (Dougherty and Monaghan, 1966). Since we observed a shift in $k\lambda_{De}$ of the points of zero group velocity, the interpretations of the plasma echoes may potentially be exploited to provide a reverse diagnostic, providing insights into the particle velocity distributions (Mace, 2004; Viñas et al., 2005), i.e., interpretations of the plasma echoes my establish that the particle velocity distributions are of the kappa type.

Figure 4.8 illustrates the time evolution of the electric field energy E_f/T_e [Figure 4.8 (a)], kinetic energy of the electron species E_e/T_e [Figure 4.8 (b)], kinetic energy of the ion species E_i/T_e [Figure 4.8 (c)] and the sum of these energies E_{tot}/T_e, for the kappa plasma [Figure 4.8 (d)].

No free energy sources, in the form of drifting plasma species, temperature anisotropy or an externally perturbing field, was present in the simulation run. Thus, stable Bernstein waves were expected to form in the kappa plasma.

However, unlike the (approximately) level energy plots produced in the Maxwellian simulation run [see Figure 4.3 (p. 91)], a decrease in the kinetic

(a) (b)

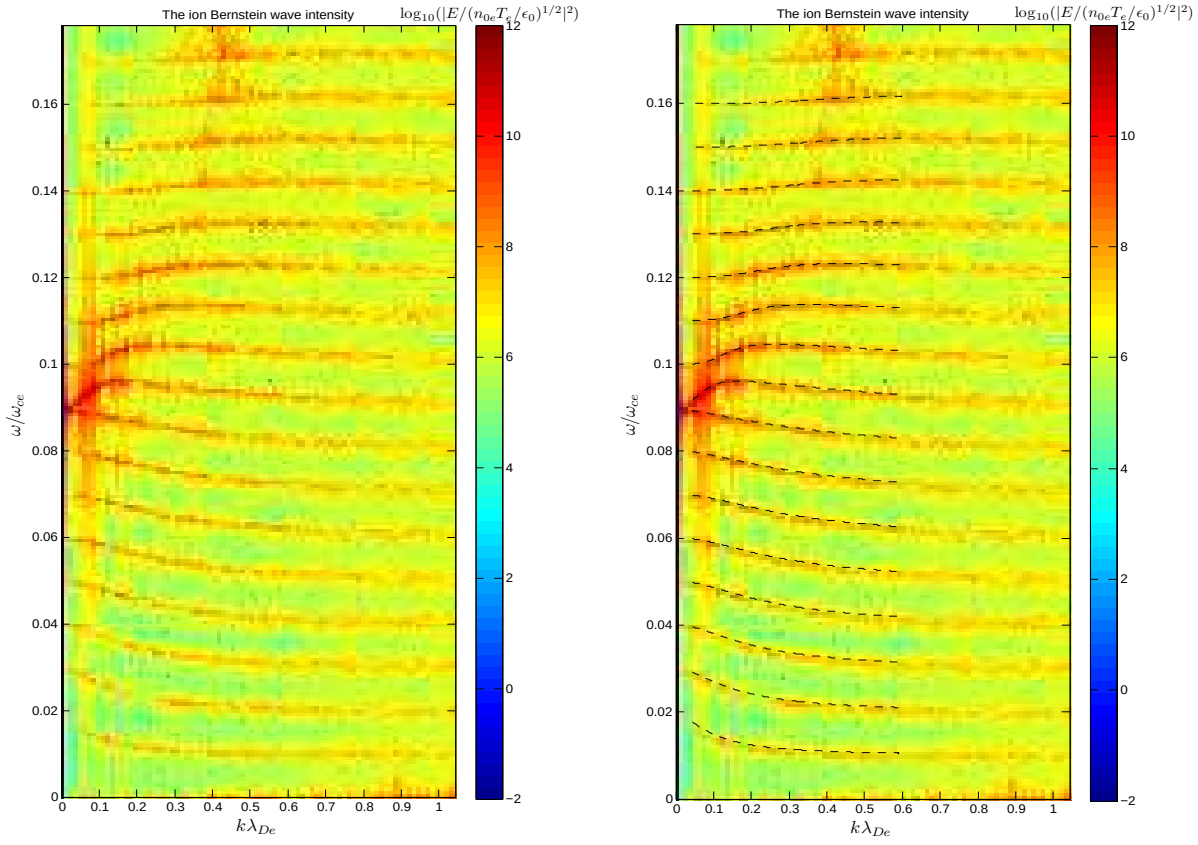

Figure 4.6: (a) The ion Bernstein wave intensity for a kappa plasma, along with (b) the ion Bernstein dispersion relation, Equation (4.10), superimposed

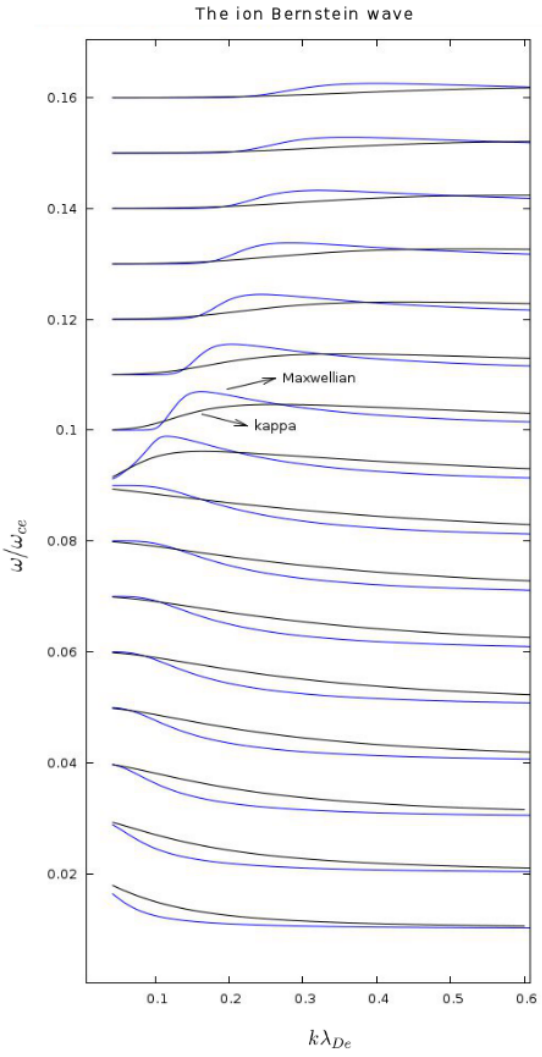

Figure 4.7: Comparison of the ion Bernstein dispersion relations for waves in Maxwellian and kappa plasmas, Equations (4.1) and (4.10), respectively.

energy of the electron species E_e/T_e is observed, during $0 < \omega_{pe}t < 1000$, with a corresponding increase in the electric field energy E_f/T_e, as seen in Figures 4.8 (a) and (b), respectively. During the times $1000 < \omega_{pe}t < 2000$ a downward trend is observed in the electric field energy, with an upward trend in the kinetic energy of the electron species [see Figures 4.8 (a) and (b)]. At $\omega_{pe}t > 2000$ the kinetic energy of the electron species remains approximately constant, to within the natural fluctuation levels arising due to using discrete simulation particles, and a gradual decrease in the electric field energy is observed.

The ion species, on the other hand, is observed to increase in kinetic energy over the period $1000 < \omega_{pe}t < 6000$, after which the energy remains approximately constant, to within expected levels [see Figure 4.8 (c)]. The exact cause of the energy transfer observed in the kappa simulation run is uncertain at present, as plasma instability was not expected.

It is well known that the Bernstein waves are purely kinetic waves (Swanson, 2003), i.e., they arise due to the discrete particle nature of the plasma. We speculate that the enhanced discreteness effects and fluctuations in the kappa plasma, demonstrated in the simulations of Chapter 3 (p. 39), could be a possible influence on this energy transfer.

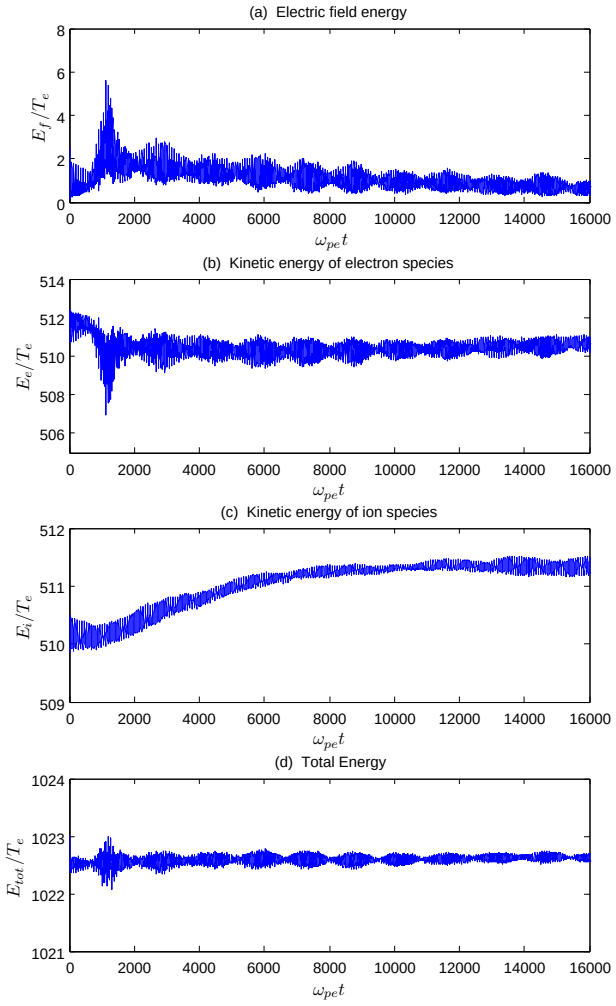

Figure 4.8: The time evolution of (a) the electric field energy E_f/T_e, (b) kinetic energy of the electron species E_e/T_e, (c) kinetic energy of the ion species E_i/T_i and (d) the sum of these energies $E_{\rm tot}/T_e$.

Chapter 5

Summary and conclusions

The aim of this research project was to develop a particle-in-cell simulation code, using the C programming language, and to use it to investigate space plasma wave phenomena. The simulation code we developed is one dimensional, allowing parameters to vary only along the x axis. It is electrostatic, but allows for a uniform ambient magnetic field which may be directed at arbitrary angles with respect to the x axis.

Message Passing Interface (MPI) was utilised to parallelise our simulation code for a distributed memory system using the particle decomposition technique (Liewer et al., 1988; Dawson et al., 1993; Martino et al., 2001; Qiang and Xiaoye, 2010). This allowed large scale simulations to be run using millions of plasma particles. To further increase the efficiency of our parallelisation scheme, we employed the Manager-Workers pattern (Ortega-Arjona, 2004), described in Section 2.6 (p. 34). The Manager-Workers pattern was used to organise the simulation computations on an activity basis, i.e., processors were assigned different tasks in the simulation run [see Section 2.6 (p. 34)]. Preliminary results showed a decrease in the simulation run times when using the Manager-Workers pattern, compared to using only the particle decomposition technique, when a large number of computationally intensive diagnostics were carried out.

Our particle-in-cell simulation code incorporated a kappa distributed velocity loader, which we devised [see Section 2.1.2 (p. 15)]. Although not many particle-in-cell simulations model their plasma particles using kappa velocity distributions, the kappa distribution has, however, been generally found to

provide a more realistic representation of observed particle distributions in space (Gloeckler and Hamilton, 1987; Christon et al., 1988; Leubner, 2004; Pierrard and Lazar, 2010). Our kappa velocity loader relies on the closely related Student t distribution (Press et al., 2007), which was found to reduce to the one dimensional kappa distribution, Equation (2.5), by making the substitutions in Equations (2.7) and (2.8). Thus we were able to employ the known method for generating deviates from the Student t distribution (Press et al., 2007, p. 371) to obtain deviates from the kappa distribution [see Section 2.1.2 (p. 15)]. Good agreement between the measured particle velocity distributions, loaded using the method described in Section 2.1.2 (p. 15), and the kappa distribution, Equation (2.5), was obtained, as seen in Figure 3.7 (p. 60).

We mention parenthetically that Koen et al. (2012a,b) have undertaken studies of electron-acoustic and electron plasma waves in kappa plasmas. While those studies have little bearing on the results of this thesis, we point out that the main difference between the code of Koen et al. (2012a,b) and the code developed for this thesis is that we developed a kappa loader which relies on the Student t distribution, while Koen et al. (2012a,b) used the more complicated rejection method for their kappa loader. Also, our code was parallelised using MPI and employed the Manager-Workers pattern, while Koen et al. (2012a,b) used OpenMP to parallelise their code.

The developed particle-in-cell simulation code and kappa particle loader were first used to investigate the ion-acoustic instability, excited by a drifting electron species [see Chapter 3 (p. 39)]. Simulations were run for (a) an electron-ion plasma modelled by Maxwellian velocity distributions and (b) an electron-ion plasma modelled by kappa velocity distributions (having equal kappa indices $\kappa_e = \kappa_i = 2$). Both simulations employed identical run parameters. However, to provide the same destabilising influence to the ion-acoustic wave in both simulations, a super sonic electron drift v_d of $v_d = 6v_s = 0.6v_{the}$ was used for the Maxwellian simulation run and $v = 6v_s^\kappa = 0.35v_{the}$ was used for the kappa simulation run. This electron drift speed also provided an ion-acoustic growth rate sufficiently high so that the non-linear phase of the ion-acoustic instability could be observed without resorting to an unreasonable number of time steps. The simulation results were compared to kinetic theory and the behaviour of the ion-acoustic instability in each of the plasmas was discussed.

The electric field intensity spectrum, as a function of ω and k, was analysed

in each simulation run to establish the existence of waves of the ion-acoustic type in the plasma. Confirmation of ion-acoustic waves is given in Figures 3.6 (p. 58) and 3.12 (p. 72) for the Maxwellian and kappa plasmas, respectively. Areas of strong wave activity, in these figures, were found to agree well with the linear dispersion relations for ion-acoustic waves, Equation (3.5) for the Maxwellian plasma, and Equation (3.8) for the kappa plasma. The behaviour of the ion-acoustic waves were found to be generally similar in both the Maxwellian and kappa plasmas; however, enhanced discreteness effects and thermal fluctuations were observed in the kappa plasma, as predicted by (Mace et al., 1998). Thus, higher levels of noise were observed in the kappa simulation run, described Section 3.4 (p. 57).

In both the kappa and Maxwellian simulations runs, the total energy was conserved, to within the expected errors in the simulation techniques, confirming the validity of the simulation runs.

Analysis of the energy plots for both the Maxwellian and kappa simulation runs, Figures 3.2 (p. 50) and 3.8 (p. 64), respectively, indicated that the ion-acoustic instability evolved in three phases. During the first phase, the ion-acoustic waves grew out of the background of random thermal fluctuations. This was seen as an exponential increase in the electric field energy in the Maxwellian plasma [see Figure 3.2 (a) during $0 < \omega_{pe}t < 1230$]. However, enhanced levels of fluctuations were observed to obscure the exponential growth of electric field energy in the kappa plasma [see Figure 3.8 (a) during $0 < \omega_{pe}t < 860$]. Examination of the the kinetic energy of the electron species, Figures 3.2 (b) and 3.8 (b), respectively, as well as the electron velocity distributions, Figures 3.4 (p. 55) and 3.10 (p. 68), respectively, indicated that the waves grew as a result of electrons resonantly feeding energy into them. Thus, the kinetic energy of the electron species decreased and plateau formation occurred in the electron velocity distributions, for both the Maxwellian and kappa plasmas, during the initial phase. For our choice of simulation run parameters, the kappa distribution was found to have a steeper positive slope, at a velocity corresponding to the ion-acoustic speed than the Maxwellian (compare the positive slopes of Figures 3.4 (p. 55) and 3.10 (p. 68) at their respective ion-acoustic speeds). Thus the kappa distribution provided more electrons to resonantly interact with the wave. Vortex structures, arising due to ion trapping by the growing ion-acoustic waves, was observed in the ion phase space of the Maxwellian plasma [see Figure 3.3 (p. 53)]; however, this degree of particle trapping was not observed in the kappa plasma [see Figure 3.9 (p. 66)].

The second phase was defined on the interval $1230 < \omega_{pe}t < 1700$ for the Maxwellian plasma and $860 < \omega_{pe}t < 1200$ for the kappa plasma. The electric field energy, Figures 3.2 (a) (p. 50) and 3.8 (a) (p. 64) for the Maxwellian and kappa plasmas, respectively, during this phase, stopped growing, due to a depletion of the free energy source in the electron velocity distributions via plateau formation [see Figures 3.4 (p. 55) and 3.10 (68), respectively]. This occurred sooner in the kappa plasma, at the time $\omega_{pe}t \approx 860$, than it did in the Maxwellian plasma, where it occurred at the time $\omega_{pe}t \approx 1230$. This is likely due to a faster instability growth rate in the kappa plasma.

The final phase of each instability was defined on the interval $\omega_{pe}t > 1700$ for the Maxwellian plasma and $\omega_{pe}t > 1200$ for the kappa plasma. During this phase, the kinetic energies of both the electron and ion species, as well as the electric field energy, remained approximately constant, as seen in Figures 3.2 (p. 50) and 3.8 (64), indicative of plasmas in equilibrium. Fluctuations in the energies, arising as a consequence of using discrete simulation particles, were, however, observed. In both the Maxwellian and kappa plasmas, a shoulder was observed in the post-saturation electron velocity distribution, at $v/v_{the} \approx 2$ and $v/v_{the} \approx 1$ in the Maxwellian and kappa plasmas, respectively. Beam-like modes were observed in the wave intensity plots for the Maxwellian and kappa plasmas, Figures 3.6 (p. 58) and 3.12 (p. 72), respectively. We speculate that these beam-like modes are associated with the shoulders observed in the electron velocity distributions; however, the source of these shoulders is uncertain at present. As time progressed, the ion velocity distributions were observed to become broader, indicating particle heating, and developed a small net drift of $v/v_{the} \approx 0.01$ and $v/v_{the} \approx 0.0025$ in the Maxwellian and kappa plasmas, Figures 3.5 (p. 56) and 3.11 (p. 69), respectively.

Another noteworthy observation was that the net gain or loss in the particle kinetic energies were found to greatly exceed the overall increase in the field energy. This suggests that the ion-acoustic instability provides a means to transfer energy from one plasma species to another.

As a further case study, electrostatic Bernstein waves were investigated in a stable electron-ion plasma. A static magnetic field, directed perpendicularly to the x direction, the direction of wave propagation, was included in the simulation. To investigate the effect the kappa distribution has on the dispersion properties of the Bernstein waves, simulations were run for (a) an

electron-ion plasma modelled by Maxwellian velocity distributions and (b) an electron-ion plasma modelled by kappa velocity distributions.

The spectrum of electric field intensities, as functions of ω and k, was then analysed. The regions of strongest wave activity were found to agree well with the linear dispersion relations for generalised Bernstein waves, Equations (4.1) and (4.10), for the Maxwellian and kappa plasmas, respectively, which were derived by Mace (2003, 2004). In the simulation runs we used a reduced ion-to-electron mass ratio of $m_i/m_e = 100$, which allowed sufficient separation of the electron and ion time scales, but permitted both electron and ion Bernstein waves to be resolved simultaneously.

The intensity plots of Figures 4.1 (p. 87) and 4.4 (p. 93), for the Maxwellian and kappa plasmas respectively, illustrated five electron Bernstein waves, i.e., those which propagate between harmonics of the electron cyclotron frequency. The kappa distribution was found to produce a change in the wave behaviour in all frequency domains for these waves, when compared to that of the Maxwellian. The kappa distribution, however, had no effect on the upper hybrid frequency, i.e., the upper hybrid frequency in both the Maxwellian and kappa plasmas was equal, as expected.

In both plasmas, the single wave observed to propagate below the upper hybrid frequency displayed enhanced levels of wave activity occurring at frequencies decreasing monotonically from $\omega/\omega_{ce} = 2$ to $\omega/\omega_{ce} = 1$, as $k\lambda_{De}$ increased. This wave in the kappa plasma, however, exhibited a slower monotonic decrease to $\omega/\omega_{ce} = 1$, when compared to the Maxwellian [see Figures 4.1 (p. 87) and 4.4 (p. 93), as well as the dispersion relations in Figure 4.5 (p. 95)].

For the wave propagating within the upper hybrid frequency band, as well as those in the three harmonic bands above it, the regions of strong wave activity in the kappa plasma were observed to occupy a diminished range of frequencies, over the whole range of $k\lambda_{De}$ values, when compared to their Maxwellian counterparts. Also, a shift in the location of the peak frequencies of observed enhanced wave activity, to higher values of $k\lambda_{De}$ was observed in the kappa plasma, when compared to those in the Maxwellian plasma [see Figures 4.1 (p. 87) and 4.4 (p. 93), as well as the dispersion relations in Figure 4.5 (p. 95)].

The intensity plots of Figures 4.2 (p. 89) and 4.6 (p. 97), for the Maxwellian and kappa plasmas respectively, illustrated seventeen ion Bernstein waves.

The general behaviour of the ion Bernstein waves was found to be similar to that of the electron Bernstein type. The differences between the ion Bernstein and electron Bernstein waves are that the electron Bernstein wave frequencies are governed by ω_{ce}, while the ion Bernstein wave frequencies are governed by ω_{ci}. Second, the electron Bernstein wave wavelengths are governed by R_{Le}, while the ion Bernstein wave wavelengths are governed by R_{Li}. Finally, the frequency dividing the two types of dispersion behaviour for electron Bernstein waves is ω_{uh}, while that for ion Bernstein waves is ω_{lh} The lower hybrid frequency, in our simulations, equalled the 9th harmonic of the ion cyclotron frequency, $\omega_{lh} = 9\omega_{ci}$, in both the Maxwellian and kappa plasmas.

The kappa distribution was found to produce a change in the wave behaviour, in all frequency domains, for ion Bernstein waves as well. Enhanced levels of wave activity were observed to occur at frequencies decreasing monotonically from $\omega = n\omega_{ci}$ to $\omega = (n-1)\omega_{ci}$, for the waves propagating below the lower hybrid frequency band, as $k\lambda_{De}$ increased. A slower fall off of these waves was observed in the kappa plasma, when compared to those in the Maxwellian plasma [see Figures 4.2 (p. 89) and 4.6 (p. 97), as well as the dispersion relations in Figure 4.7 (p. 98)]. This trend was also observed for the wave propagating within the lower hybrid frequency band in the kappa plasma.

Enhanced levels of wave activity were also observed to occupy a diminished range of frequencies, over the range of $k\lambda_{De}$ values, for the waves propagating above the lower hybrid frequency band in the kappa plasma. The regions of strong wave activity were also observed to occur at peak frequencies shifted to higher values of $k\lambda_{De}$ in the kappa plasma, when compared to those in the Maxwellian [see Figures 4.2 (p. 89) and 4.6 (p. 97), as well as the dispersion relations in Figure 4.7 (p. 98)].

Figures 4.3 (p. 91) and 4.8 (p. 100) illustrated the energies in the Maxwellian and kappa plasmas, respectively. Although stable Bernstein waves were expected in both plasmas, the kappa plasma exhibited energy exchange between its species [see Figure 4.8 (p. 100)], indicative of a plasma not in equilibrium. The cause of this energy exchange is unknown at present; however, we speculate that the enhanced thermal fluctuations, associated with the kappa plasma, had some effect on this.

The results of the simulations presented in this thesis give us considerable confidence of the correctness of our particle-in-cell simulation code. They

also validate the simulation technique as a means to investigate space plasma phenomena, and readily provide insights into the nonlinear regime of plasma wave evolution. The results also demonstrate the usefulness of the kappa loader that we devised, making more realistic approximations to actual observed particle distributions a reality.

Appendix A

In the particle-in-cell simulation code described in this thesis, the plasma species are loaded into the simulation box with either Maxwellian or kappa velocity distributions. To achieve the relevant loading, the particle velocities are assigned random deviates generated from the chosen distribution.

Deviates from the Maxwellian distribution are generated using the Box-Muller transform (Box and Muller, 1958), described in Section 2.1.1 (p. 14). The Box-Muller transform generates the normal distributed random deviates y_1 and y_2 using the equations (Press et al., 2007, p. 364)

$$y_1 = \sqrt{-2 \ln x_1} \cos(2\pi x_2), \tag{A.1}$$

$$y_2 = \sqrt{-2 \ln x_1} \sin(2\pi x_2), \tag{A.2}$$

where x_1 and x_2 are two uniformly distributed random deviates. The two normal distributed deviates, y_1 and y_2, are then used to generate deviates from the Maxwellian distribution [see Section 2.1.1 (p. 14) or Press et al. (2007, p. 364)]. Presented here is a derivation of Equations (A.1) and (A.2).

The standard normal distribution $p(y)$ is given by (Press et al., 2007, p. 364)

$$p(y)dy = \frac{1}{\sqrt{2\pi}} e^{-y^2/2} dy. \tag{A.3}$$

By employing the independence property, the joint probability distribution for two quantities y_1 and y_2 is given by

$$
\begin{aligned}
p(y_1, y_2)dy_1dy_2 &= p(y_1)dy_1 \cdot p(y_2)dy_2 \\
&= \frac{1}{2\pi}e^{-(y_1^2+y_2^2)/2}dy_1dy_2. \qquad \text{(A.4)}
\end{aligned}
$$

Now, treating the variables y_1 and y_2 as representing the coordinates of a point in a Cartesian coordinate system, the corresponding coordinates of the point in a polar coordinate system (r, θ) are related via

$$
\begin{aligned}
r^2 &= y_1^2 + y_2^2, \qquad \text{(A.5)} \\
\theta &= \tan\left(\frac{y_2}{y_1}\right), \qquad \text{(A.6)}
\end{aligned}
$$

with the inverse relations given by

$$
\begin{aligned}
y_1 &= r\cos\theta, \qquad \text{(A.7)} \\
y_2 &= r\sin\theta. \qquad \text{(A.8)}
\end{aligned}
$$

The Jacobian determinant for this transformation of coordinates is thus (Gradshteyn and Ryzhik, 2007, p. 1078)

$$
J_y = \begin{vmatrix} \frac{\partial y_1}{\partial r} & \frac{\partial y_1}{\partial \theta} \\ \frac{\partial y_2}{\partial r} & \frac{\partial y_2}{\partial \theta} \end{vmatrix} = r\cos^2\theta + r\sin^2\theta = r. \qquad \text{(A.9)}
$$

Hence, the polar form of Equation (A.4) is

$$
p(r, \theta)drd\theta = \frac{1}{2\pi}e^{-r^2/2}rdrd\theta. \qquad \text{(A.10)}
$$

Now, to obtain the values of r and θ we first find the marginal probabilities of Equation (A.10). The marginal probability distribution of Equation (A.10)

with respect to r, i.e., $p(r)dr$, is obtained via an integration of Equation (A.10) with respect to θ, from $0 \rightarrow 2\pi$. That is,

$$\begin{aligned} p(r)dr &= \left(\int_0^{2\pi} \frac{r}{2\pi} e^{-r^2/2} d\theta \right) dr \\ &= 2\pi \frac{r}{2\pi} e^{-r^2/2} dr \\ &= r e^{-r^2/2} dr. \end{aligned} \tag{A.11}$$

The marginal probability distribution of Equation (A.10) with respect to θ, i.e., $p(\theta)d\theta$, is obtained via an integration of Equation (A.10) with respect to r, from $0 \rightarrow \infty$. That is,

$$\begin{aligned} p(\theta)d\theta &= \left(\int_0^{\infty} \frac{r}{2\pi} e^{-r^2/2} dr \right) d\theta \\ &= \frac{1}{2\pi} d\theta, \end{aligned} \tag{A.12}$$

where we used the substitutions $u = -r^2/2$ and $du = -rdr$ to evaluate the integral in Equation (A.12).

It should be noted that the fundamental transformation law of probabilities states that if v is a random deviate with the probability distribution $p(v)dv$, and if there exists w which is a function of v, then the probability distribution of w is given by (Press et al., 2007, p. 362)

$$p(w)dw = p(v) \left| \frac{dv}{dw} \right| dw. \tag{A.13}$$

Furthermore, if v is a deviate defined to be uniformly distributed on the interval $[0, 1]$, then Equation (A.13) becomes (Press et al., 2007, p. 362)

$$p(w)dw = \left| \frac{dv}{dw} \right| dw. \tag{A.14}$$

Thus, if we let r and θ be functions of the deviates x_1 and x_2, respectively, and define x_1 and x_2 to be uniformly distributed on the interval $[0, 1]$, then the marginal probabilities in Equations (A.11) and (A.12) can be written, using Equation (A.14), as

$$\begin{aligned} p(r)dr &= \left|\frac{dx_1}{dr}\right| dr, && \text{(A.15)} \\ p(\theta)d\theta &= \left|\frac{dx_2}{d\theta}\right| d\theta. && \text{(A.16)} \end{aligned}$$

Having derived the distributions in Equations (A.15) and (A.16) we may now obtain equations for r and θ in terms of the uniformly distributed deviates x_1 and x_2, respectively. Integrating Equation (A.15) up to an arbitrary $r^{'}$, yields

$$\begin{aligned} \int_0^{r'} p(r)dr &= \int_0^{r'} \left|\frac{dx_1}{dr}\right| dr \\ \int_0^{r'} re^{-r^2/2}dr &= |x_1| \\ 1 - e^{-(r')^2/2} &= |x_1|. && \text{(A.17)} \end{aligned}$$

Since x_1 is defined strictly to be positive, i.e., x_1 is defined on the interval $[0, 1]$, inverting Equation (A.17) yields, where we may omit the prime,

$$\begin{aligned} 1 - e^{-r^2/2} &= x_1 \\ e^{-r^2/2} &= 1 - x_1 \\ -r^2 &= 2\ \ln(1 - x_1) \\ r &= \sqrt{-2\ \ln(1 - x_1)} \\ r &= \sqrt{-2\ \ln x_1}, && \text{(A.18)} \end{aligned}$$

where the last step in Equation (A.18) follows from the fact that $1 - x_1$ and x_1, respectively, have the same distribution, i.e., both are uniformly

distributed on the interval $[0, 1]$. Similarly, integrating Equation (A.16) up to an arbitrary $\theta^{'}$, yields

$$\begin{aligned} \int_0^{\theta'} p(\theta)d\theta &= \int_0^{\theta'} \left|\frac{dx_2}{d\theta}\right| d\theta \\ \int_0^{\theta'} \frac{1}{2\pi} d\theta &= |x_2| \\ \frac{\theta'}{2\pi} &= |x_2|. \end{aligned} \tag{A.19}$$

Inverting Equation (A.19) yields, omitting the prime,

$$\begin{aligned} \frac{\theta}{2\pi} &= x_2 \\ \theta &= 2\pi x_2. \end{aligned} \tag{A.20}$$

Therefore, having the definitions for r and θ in terms of the uniformly distributed deviates x_1 and x_2, Equations (A.18) and (A.20), respectively, we get equations for the variables y_1 and y_2 using Equations (A.7) and (A.8). Substituting Equations (A.18) and (A.20) into Equations (A.7) and (A.8) yields

$$y_1 = \sqrt{-2\ln\, x_1}\, \cos(2\pi x_2), \tag{A.21}$$

$$y_2 = \sqrt{-2\ln\, x_1}\, \sin(2\pi x_2), \tag{A.22}$$

which are identical to the Box-Muller Equations (A.1) and (A.2). Thus if x_1 and x_2 are deviates uniformly distributed on the interval $[0, 1]$, then two random deviates y_1 and y_2 from the normal distribution may be generated using Equations (A.1) and (A.2).

Appendix B

In Appendix A, a derivation of the equations used to generate the Box-Muller deviates was presented. Presented here is a derivation of the equation used to generate a Student t deviate.

Random deviates from the kappa distribution are generated in our simulation using the closely related Student t distribution, as described in Section 2.1.2 (p. 15). A deviate from the Student t distribution is generated by first generating the deviate y using the equation (Press et al., 2007, p. 371)

$$y = \sqrt{\nu(u_1^{-2/\nu} - 1)}\,\cos(2\pi u_2), \tag{B.1}$$

where u_1 and u_2 are two uniformly distributed random deviates and ν shapes the tail of the Student t distribution. The deviate y is then used to generate a deviate from the Student t distribution [see Section 2.1.2 (p. 15) or (Press et al., 2007, p. 371)].

Equation (B.1) can be derived in a manner similar to the derivation of the Box-Muller equations derived in Appendix A; however, only one deviate is generated at a time, unlike the Box-Muller transform which generates two (Bailey, 1994; Press et al., 2007).

The multivariate form of the Student-t distribution, with mean $\mu = 0$ and $\sigma = 1$, is given by (Shaw and Lee, 2008)

$$p(y_1, y_2, ..., y_n)dy_1dy_2...dy_n \equiv p(\boldsymbol{y})d\boldsymbol{y} = \frac{\Gamma(\frac{\nu+q}{2})}{\Gamma(\frac{\nu}{2})}\frac{\sqrt{|R|}}{\sqrt{\nu^q\pi^q}}\left(1 + \frac{\boldsymbol{y}^T R\boldsymbol{y}}{\nu}\right)^{-(\nu+q)/2} d\boldsymbol{y}, \tag{B.2}$$

where $\boldsymbol{y}^T$ is the transpose of the vector $\boldsymbol{y} = (y_1, y_2, ..., y_n)$, q is the dimensionality of the distribution, R is a matrix characterising the correlation between the variables and ν is a positive real number known as the shape parameter. The bivariate form of Equation (B.2), i.e., $q = 2$ in Equation (B.2), with zero correlation between the variables, i.e., R is a $q \times q$ identity matrix, is

$$\begin{aligned} p(y_1, y_2)dy_1 dy_2 &= \frac{\Gamma(\frac{\nu+2}{2})}{\Gamma(\frac{\nu}{2})} \frac{1}{\nu\pi} \left(1 + \frac{y_1^2 + y_2^2}{\nu}\right)^{-(\nu+2)/2} dy_1 dy_2 \\ &= \frac{1}{2\pi} \left(1 + \frac{y_1^2 + y_2^2}{\nu}\right)^{-(\nu+2)/2} dy_1 dy_2, \end{aligned} \tag{B.3}$$

where we used the following property of the gamma function in the last step of Equation (B.3)

$$\Gamma(z+1) = z\Gamma(z).$$

As before, we now treat the quantities y_1 and y_2 as the coordinates of a point in a Cartesian coordinate system. The coordinates of the corresponding point in a polar coordinate system are related via

$$r^2 = y_1^2 + y_2^2, \tag{B.4}$$

$$\theta = \tan\left(\frac{y_2}{y_1}\right), \tag{B.5}$$

with the inverses

$$y_1 = r\cos\theta, \tag{B.6}$$

$$y_2 = r\sin\theta. \tag{B.7}$$

This transformation yields the polar form of Equation (B.3) as

$$p(r,\theta)drd\theta = \frac{r}{2\pi}\left(1+\frac{r^2}{\nu}\right)^{-(\nu+2)/2} drd\theta. \tag{B.8}$$

The values of r and θ are obtained by first finding the marginal probabilities of Equation (B.8). The marginal probability distribution of Equation (B.8) with respect to r, i.e., $p(r)dr$, is obtained via an integration of Equation (B.8) with respect to θ, from $0 \to 2\pi$. That is,

$$\begin{aligned} p(r)dr &= \left[\int_0^{2\pi} \frac{r}{2\pi}\left(1+\frac{r^2}{\nu}\right)^{-(\nu+2)/2} d\theta\right] dr \\ &= 2\pi\frac{r}{2\pi}\left(1+\frac{r^2}{\nu}\right)^{-(\nu+2)/2} dr \\ &= r\left(1+\frac{r^2}{\nu}\right)^{-(\nu+2)/2} dr. \end{aligned} \tag{B.9}$$

The marginal probability distribution of Equation (B.8) with respect to θ, i.e., $p(\theta)d\theta$, is obtained via an integration of Equation (B.8) with respect to r, from $0 \to \infty$. That is,

$$p(\theta)d\theta = \left[\int_0^{\infty} \frac{r}{2\pi}\left(1+\frac{r^2}{\nu}\right)^{-(\nu+2)/2} dr\right] d\theta. \tag{B.10}$$

Equation (B.10) is evaluated using the standard integral (Gradshteyn and Ryzhik, 2007, p. 325 ch. 3.251 Eq. 11)

$$\int_0^{\infty} x^{\mu-1}(1+\beta x^p)^{-n} dx = \frac{1}{p}\beta^{-\frac{\mu}{p}} B\left(\frac{\mu}{p}, n-\frac{\mu}{p}\right), \tag{B.11}$$

where the Beta function $B(x,y)$ is defined as

$$B(x,y) = \frac{\Gamma(x)\Gamma(y)}{\Gamma(x+y)}.$$

Thus setting $\mu = 2$, $p = 2$, $\beta = 1/\nu$ and $n = (\nu + 2)/2$ in Equation (B.11), Equation (B.10) reduces to

$$\begin{aligned} p(\theta)d\theta &= \frac{1}{2\pi}\frac{\nu}{2}B\left(1, \frac{\nu}{2} + 1 - 1\right)d\theta \\ &= \frac{\nu}{4\pi}\frac{\Gamma(1)\Gamma(\nu/2)}{\Gamma(1+\nu/2)}d\theta \\ &= \frac{1}{2\pi}d\theta. \end{aligned} \tag{B.12}$$

Analogously to the derivation in Appendix A, we let r and θ be functions of two deviates u_1 and u_2 which are uniformly distributed on the interval $[0, 1]$. Thus the marginal probabilities in Equations (B.9) and (B.12) can be written as

$$p(r)dr = \left|\frac{du_1}{dr}\right| dr, \tag{B.13}$$

$$p(\theta)d\theta = \left|\frac{du_2}{d\theta}\right| d\theta. \tag{B.14}$$

The equations for r and θ in terms of u_1 and u_2, respectively, are obtained by integrating Equations (B.13) and (B.14). Taking the integral of Equation (B.13) up to $r^{'}$ yields,

$$\begin{aligned} \int_0^{r'} p(r)dr &= \int_0^{r'} \left|\frac{du_1}{dr}\right| dr \\ \int_0^{r'} r\left(1 + \frac{r^2}{\nu}\right)^{-(\nu+2)/2} dr &= |u_1| \\ 1 - \left(1 + \frac{(r')^2}{\nu}\right)^{-\nu/2} &= |u_1|, \end{aligned} \tag{B.15}$$

where we used the following standard integral in the last step of Equation (B.15) (Gradshteyn and Ryzhik, 2007, p. 71 ch. 2.124 Eq. 2)

$$\int x(a+bx^2)^{-m}dx = -\frac{1}{2b(m-1)(a+bx^2)^{m-1}}. \tag{B.16}$$

Since u_1 is defined to be positive, i.e., u_1 is distributed on the interval [0,1], inverting Equation (B.15) yields (omitting the prime)

$$\begin{aligned}
1-\left(1+\frac{r^2}{\nu}\right)^{-\nu/2} &= u_1 \\
1+\frac{r^2}{\nu} &= (1-u_1)^{-2/\nu} \\
r^2 &= \nu[(1-u_1)^{-2/\nu}-1] \\
r &= \sqrt{\nu[(1-u_1)^{-2/\nu}-1]} \\
r &= \sqrt{\nu(u_1^{-2/\nu}-1)},
\end{aligned} \tag{B.17}$$

where the last step in Equation (B.17) follows from the fact that $1-u_1$ and u_1 are both are uniformly distributed on the interval [0,1]. Similarly, taking the integral of Equation (B.14) to $\theta^{'}$ yields

$$\begin{aligned}
\int_0^{\theta'} p(\theta)d\theta &= \int_0^{\theta'} \left|\frac{du_2}{d\theta}\right| d\theta \\
\int_0^{\theta'} \frac{1}{2\pi}d\theta &= |u_2| \\
\frac{\theta'}{2\pi} &= |u_2|.
\end{aligned} \tag{B.18}$$

Inverting Equation (B.18), taking positive u_2, yields (omitting the prime)

$$\begin{aligned}
\frac{\theta}{2\pi} &= u_2 \\
\theta &= 2\pi u_2.
\end{aligned} \tag{B.19}$$

Finally, substituting Equations (B.17) and Equation (B.19) into Equation (B.6) yields

$$y = \sqrt{\nu(u_1^{-2/\nu} - 1)}\,\cos(2\pi u_2), \tag{B.20}$$

which is identical to Equation (B.1). Thus, using the uniformly distributed deviates u_1 and u_2, Equation (B.1) can be used to generate a deviate from the Student t distribution using the method described in Section 2.1.2 (p. 15).

Appendix C

In particle-in-cell simulations, a set of Newton's and Maxwell's equations are solved in discrete form at each time step of the simulation run, updating the dynamics of the simulation particles as well as the electromagnetic fields. The basic equations governing the dynamics of the plasma system, for our electrostatic simulation, are, for the particle dynamics,

$$\frac{d\boldsymbol{x}_i(t)}{dt} = \boldsymbol{v}_i(t), \tag{C.1}$$

$$m_i \frac{d\boldsymbol{v}_i(t)}{dt} = q_i \left[\boldsymbol{E}(\boldsymbol{x}_i(t), t) + \boldsymbol{v}_i(t) \times \boldsymbol{B}_0\right], \tag{C.2}$$

where $\boldsymbol{x}_i$ and $\boldsymbol{v}_i$ are the position and velocity of a particle i with mass m_i and charge q_i, $\boldsymbol{E}(\boldsymbol{x}_i(t), t)$ is the electric field and $\boldsymbol{B}_0$ is a static, uniform magnetic field, and, for the electric field,

$$\boldsymbol{\nabla} \cdot \boldsymbol{E}(\boldsymbol{x}_i, t) = \frac{1}{\epsilon_0} \sum_i n_i(\boldsymbol{x}_i, t) q_i, \tag{C.3}$$

where $n_i(\boldsymbol{x}_i, t)$ is the number density. The Equations (C.1) to (C.3) are strictly valid for S.I. units; however, particle-in-cell simulations often employ parameters in units more appropriate for physical interpretation. Our goal is to now rewrite Equations (C.1) to (C.3) in terms of units more appropriate for physical interpretation.

In particle-in-cell simulations, it is frequently useful to measure distance and time with respect to the natural length and time scales that appear in the

problem of interest. Choosing an arbitrary species α as an example, we introduce the dimensionless parameters

$$t' = \frac{t}{\tau_{p\alpha}} = \omega_{p\alpha} t, \qquad \text{and} \qquad \boldsymbol{x}_i' = \frac{\boldsymbol{x}_i}{\lambda_{D\alpha}} \tag{C.4}$$

where $\tau_{p\alpha} = 1/\omega_{p\alpha}$ is the reciprocal of the plasma frequency for the species α and $\lambda_{D\alpha}$ is the Debye length of species α.

At a more formal level, the relations given in Equation (C.4) can be written as functions

$$t'(t) = \omega_{p\alpha} t, \qquad \text{and} \qquad \boldsymbol{x}_i'(\boldsymbol{x}_i) = \frac{\boldsymbol{x}_i}{\lambda_{D\alpha}}, \tag{C.5}$$

and we can write formally, for the position of the ith particle,

$$\boldsymbol{x}_i(t) = \boldsymbol{x}_i'(t'(t))\lambda_{D\alpha}. \tag{C.6}$$

Now we wish to re-write Equation (C.1) in terms of Equations (C.5) and (C.6). First, consider the left hand side of Equation (C.1)

$$\frac{d\boldsymbol{x}_i(t)}{dt} = \frac{d}{dt}\boldsymbol{x}_i'(t'(t))\lambda_{D\alpha} = \frac{d\boldsymbol{x}_i'(t')}{dt'}\frac{dt'}{dt}\lambda_{D\alpha}, \tag{C.7}$$

and by Equation (C.5) we have

$$\frac{d\boldsymbol{x}_i(t)}{dt} = \frac{d\boldsymbol{x}_i'(t')}{dt'}\omega_{p\alpha}\lambda_{D\alpha} = \frac{d\boldsymbol{x}_i'(t')}{dt'}v_{th,\alpha}. \tag{C.8}$$

By substituting Equation (C.8) into Equation (C.1) we obtain

$$\frac{d\boldsymbol{x}_i'(t')}{dt'}v_{th,\alpha} = \boldsymbol{v}_i(t). \tag{C.9}$$

If we now introduce, by analogy with Equation (C.6)

$$\boldsymbol{v}_i(t) = \boldsymbol{v}'_i(t'(t))v_{th,\alpha}, \tag{C.10}$$

then Equation (C.9) reduces to

$$\frac{d\boldsymbol{x}'_i(t')}{dt'} = \boldsymbol{v}'_i(t'), \tag{C.11}$$

which is identical in form to the original Equation (C.1) but is now written in units given by Equation (C.4) where

$$\boldsymbol{v}'_i = \frac{\boldsymbol{v}_i}{v_{th,\alpha}}. \tag{C.12}$$

We now turn our attention to Equation (C.2). By Equation (C.10) we have

$$\frac{d\boldsymbol{v}_i(t)}{dt} = \frac{d\boldsymbol{v}'_i(t')}{dt'}\frac{dt'}{dt}v_{th,\alpha} = \frac{d\boldsymbol{v}'_i(t')}{dt'}\omega_{p\alpha}v_{th,\alpha}, \tag{C.13}$$

where the last step follows from Equation (C.5). Substituting this relation into Equation (C.2) yields

$$m_i\frac{d\boldsymbol{v}'_i(t')}{dt'} = \frac{q_i}{\omega_{p\alpha}v_{th,\alpha}}\left[\boldsymbol{E}(\boldsymbol{x}_i(t),t) + \boldsymbol{v}_i(t)\times\boldsymbol{B}_0\right]. \tag{C.14}$$

Using

$$\omega_{p\alpha}v_{th,\alpha} = \frac{q_\alpha}{m_\alpha}\left(\frac{n_{0\alpha}T_\alpha}{\epsilon_0}\right)^{1/2}, \tag{C.15}$$

Equation (C.14) can be written as

$$
\begin{aligned}
m_i \frac{d\boldsymbol{v}_i'(t')}{dt'} &= \frac{q_i m_\alpha}{q_\alpha}\left(\frac{\epsilon_0}{n_{0\alpha}T_\alpha}\right)^{1/2}\boldsymbol{E}(\boldsymbol{x}_i(t),t) + \frac{q_i}{\omega_{p\alpha}v_{th,\alpha}}\left[\boldsymbol{v}_i(t)\times\boldsymbol{B}_0\right] \\
&= \frac{q_i m_\alpha}{q_\alpha}\left(\frac{\epsilon_0}{n_{0\alpha}T_\alpha}\right)^{1/2}\boldsymbol{E}(\boldsymbol{x}_i(t),t) + \left[\frac{\boldsymbol{v}_i(t)}{v_{th,\alpha}}\times\frac{q_i}{\omega_{p\alpha}}\boldsymbol{B}_0\right] \\
&= \frac{q_i m_\alpha}{q_\alpha}\left(\frac{\epsilon_0}{n_{0\alpha}T_\alpha}\right)^{1/2}\boldsymbol{E}(\boldsymbol{x}_i(t),t) + \left[\frac{\boldsymbol{v}_i(t)}{v_{th,\alpha}}\times\frac{q_i m_\alpha}{q_\alpha}\frac{q_\alpha}{\omega_{p\alpha}m_\alpha}\boldsymbol{B}_0\right].
\end{aligned}
\tag{C.16}
$$

A dimensionless electric and magnetic field can be introduced by noting that the units of ϵ_0 are $\mathrm{C}^2/\mathrm{N.m}^2$ and hence the units of the factor $(\epsilon_0/n_{0\alpha}T_\alpha)^{1/2}$, in Equation (C.16), are easily checked to be C/N, which represents the reciprocal of the electric field units in S.I. units. Hence the quantity $(n_{0\alpha}T_\alpha/\epsilon_0)^{1/2}$ represents an electric field strength and can be used as an appropriate unit to introduce a dimensionless electric field

$$
\boldsymbol{E}'(\boldsymbol{x}_i'(\boldsymbol{x}_i),t'(t)) = \frac{\boldsymbol{E}(\boldsymbol{x}_i,t)}{(n_{0\alpha}T_\alpha/\epsilon_0)^{1/2}}. \tag{C.17}
$$

Also, the term $q_\alpha/(\omega_{p\alpha}m_\alpha)$, in Equation (C.16), has the units of C.s/ kg which is the reciprocal of the magnetic field units in S.I. units. Hence the quantity $(\omega_{p\alpha}m_\alpha)/q_\alpha$ represents a magnetic field strength and can be used as an appropriate unit to introduce a dimensionless magnetic field

$$
\boldsymbol{B}_0' = \frac{\boldsymbol{B}_0}{(\omega_{p\alpha}m_\alpha)/q_\alpha}. \tag{C.18}
$$

Thus, using Equation (C.17) and (C.18) in Equation (C.16) we obtain

$$
m_i' \frac{d\boldsymbol{v}_i'(t')}{dt'} = q'[\boldsymbol{E}'(\boldsymbol{x}_i',t') + \boldsymbol{v}_i'(t')\times\boldsymbol{B}_0'], \tag{C.19}
$$

where we have used Equation (C.12) and have introduced the dimensionless mass and charge as

$$
\begin{aligned}
m_i' &= \frac{m_i}{m_\alpha}, \\
q_i' &= \frac{q_i}{q_\alpha}.
\end{aligned}
$$

Equation (C.19) is identical in form to Equation (C.2), but is now written in terms of variables from the species α and the dimensionless fields given in Equations (C.17) and (C.18).

Finally, turning our attention to Equation (C.3), using Equation (C.17) we obtain

$$
\begin{aligned}
\boldsymbol{\nabla} \cdot \boldsymbol{E}(\boldsymbol{x}_i, t) =& \frac{\partial E_x(\boldsymbol{x}, t)}{\partial x_i} + \frac{\partial E_y(\boldsymbol{x}_i, t)}{\partial y} + \frac{\partial E_z(\boldsymbol{x}_i, t)}{\partial z} \\
=& \left(\frac{n_{0\alpha} T_\alpha}{\epsilon_0} \right)^{1/2} \left[\frac{\partial E_x'(\boldsymbol{x}_i'(\boldsymbol{x}_i), t'(t))}{\partial x'} \frac{\partial x'}{\partial x} + \frac{\partial E_y'(\boldsymbol{x}_i'(\boldsymbol{x}_i), t'(t))}{\partial y'} \frac{\partial y'}{\partial y} \right. \\
& \left. + \frac{\partial E_z'(\boldsymbol{x}_i'(\boldsymbol{x}_i), t'(t))}{\partial z'} \frac{\partial z'}{\partial z} \right] \\
=& \left(\frac{n_{0\alpha} T_\alpha}{\epsilon_0} \right)^{1/2} \frac{1}{\lambda_{D\alpha}} \boldsymbol{\nabla}' \cdot \boldsymbol{E}' \left(\boldsymbol{x}_i', t' \right) \\
=& \frac{n_{0\alpha} q_\alpha}{\epsilon_0} \boldsymbol{\nabla}' \cdot \boldsymbol{E}' \left(\boldsymbol{x}_i', t' \right),
\end{aligned}
$$

where Equation (C.5) was used in the third step. Thus Equation (C.3) can be written as

$$
\boldsymbol{\nabla}' \cdot \boldsymbol{E}'(\boldsymbol{x}_i', t') = \sum_i \frac{1}{n_{0\alpha}} n_i(\boldsymbol{x}_i, t) \frac{q_i}{q_\alpha}. \tag{C.20}
$$

Introducing the dimensionless number density $n_i'(\boldsymbol{x}_i', t')$ through

$$
n_i(\boldsymbol{x}_i, t) = n_{0\alpha} n_i'(\boldsymbol{x}_i'(\boldsymbol{x}_i), t'(t)),
$$

Equation (C.20) reduces to

$$\boldsymbol{\nabla}' \cdot \boldsymbol{E}'(\boldsymbol{x}_i', t') = \sum_i n_i'(\boldsymbol{x}_i', t') q_i',$$

which is the dimensionless form of Equation (C.3).

Appendix D

The particle-in-cell simulation code described in this thesis uses the Boris method (Boris, 1970) for updating particle velocities. As discussed in Section 2.4.1 (p. 27), the Boris method describes a three step procedure for updating the velocity of a particle. These three steps are as follows:

1. The particle, with the initial velocity $\boldsymbol{v}^{n-1/2}$, is accelerated by the electric field $\boldsymbol{E}$ for half of the time step, $\Delta t/2$, and the intermediate velocity, $\boldsymbol{v}^-$, is obtained, i.e., $\boldsymbol{v}^{n-1/2} \rightarrow \boldsymbol{v}^-$.

2. The rotation of the new particle velocity, $\boldsymbol{v}^-$, by the magnetic field $\boldsymbol{B}_0$ is then calculated for the full time step, Δt, producing the velocity $\boldsymbol{v}^+$, i.e., $\boldsymbol{v}^- \rightarrow \boldsymbol{v}^+$.

3. Finally the particle is accelerated for another half of the time step and the updated particle velocity is obtained, i.e., $\boldsymbol{v}^+ \rightarrow \boldsymbol{v}^{n+1/2}$.

Further details for the Boris method is given in Section 2.4.1 (p. 27) and can also be found in the works by Boris (1970), Hockney and Eastwood (1981) and Birdsall and Langdon (1985). The rotation computed in step two is calculated using

$$\frac{\boldsymbol{v}^+ - \boldsymbol{v}^-}{\Delta t} = \frac{q}{2m}\left(\boldsymbol{v}^+ + \boldsymbol{v}^-\right) \times \boldsymbol{B}. \tag{D.1}$$

Boris (1970) further described a two step method to perform the calculation in Equation (D.1) using the equations

$$\boldsymbol{v}^{'} = \boldsymbol{v}^{-} + \boldsymbol{v}^{-} \times \boldsymbol{t}, \tag{D.2}$$
$$\boldsymbol{v}^{+} = \boldsymbol{v}^{-} + \boldsymbol{v}^{'} \times \boldsymbol{s}, \tag{D.3}$$

where $\boldsymbol{v}^{'}$ in Equations (D.2) and (D.3) is an intermediate velocity and $\boldsymbol{t}$ is given by

$$\boldsymbol{t} = \frac{q\boldsymbol{B}\Delta t}{2m}, \tag{D.4}$$

and $\boldsymbol{s}$ is a scaled version of $\boldsymbol{t}$ given by

$$\boldsymbol{s} = \frac{2\boldsymbol{t}}{1+t^2}, \tag{D.5}$$

Even though Boris (1970) used geometry to derive Equations (D.2) and (D.3), presented here is a derivation of an equivalent equation using tensor analysis.

First we write the variables as

$$\begin{aligned} \boldsymbol{v}^{-} &= (v_1^{-}, v_2^{-}, v_3^{-}), \\ \boldsymbol{v}^{+} &= (v_1^{+}, v_2^{+}, v_3^{+}), \\ \boldsymbol{t} &= (t_1, t_2, t_3). \end{aligned}$$

Thus, performing the calculations given in Equations (D.2) and (D.3) yields the results (omitting the steps)

$$\boldsymbol{v}^{+} = \frac{1}{1+\|\boldsymbol{t}\|^2} \begin{bmatrix} (1+t_1^2-t_2^2-t_3^2)v_1^{-} + 2[(t_1t_2+t_3)v_2^{-} - (t_2+t_1t_3)v_3^{-}] \\ (1-t_1^2+t_2^2-t_3^2)v_2^{-} + 2[(t_1t_2-t_3)v_1^{-} + (t_1+t_2t_3)v_3^{-}] \\ (1-t_1^2-t_2^2+t_3^2)v_3^{-} + 2[(t_1t_3+t_2)v_1^{-} - (t_1+t_2t_3)v_2^{-}] \end{bmatrix}. \tag{D.6}$$

We shall now show that the result given in Equation (D.6) can be reproduced using tensor analysis to evaluate Equation (D.1). We now rewrite Equation (D.1) as

$$\boldsymbol{v}^+ = \boldsymbol{v}^- + \left(\boldsymbol{v}^+ + \boldsymbol{v}^-\right) \times \boldsymbol{t}. \tag{D.7}$$

Using Cartesian tensor notation, Equation (D.7) becomes

$$v_i^+ = v_i^- + \epsilon_{ijk} v_j^+ t_k + \epsilon_{ijk} v_j^- t_k, \tag{D.8}$$

where ϵ_{ijk}, the Levi-Civita symbol, is defined via (Aris, 1989)

$$\epsilon_{ijk} = \begin{cases} +1, & \text{for an even permutation of } (i,j,k), \\ -1, & \text{for an odd permutation of } (i,j,k), \\ 0, & \text{if } i=j \text{ or } j=k \text{ or } k=i. \end{cases}$$

Equation (D.8) can now be written in the simplified form, as

$$(\delta_{ij} - \epsilon_{ijk} t_k) v_j^+ = (\delta_{ij} + \epsilon_{ijk} t_k) v_j^-, \tag{D.9}$$

where δ_{ij} is the Kronecker delta tensor. By defining

$$\begin{aligned} m_{ij} &= \delta_{ij} - \epsilon_{ijk} t_k, \\ n_{ij} &= \delta_{ij} + \epsilon_{ijk} t_k, \end{aligned}$$

Equation (D.9) becomes

$$m_{ij} v_j^+ = n_{ij} v_j^-, \tag{D.10}$$

or in matrix notation

$$MV^+ = NV^-. \tag{D.11}$$

Thus

$$V^+ = M^{-1}NV^-. \tag{D.12}$$

Using the definitions of m_{ij} and n_{ij}, the matrices M and N are respectively given by

$$M = \begin{pmatrix} 1 & -t_3 & t_2 \\ t_3 & 1 & -t_1 \\ -t_2 & t_1 & 1 \end{pmatrix}, \tag{D.13}$$

and

$$N = \begin{pmatrix} 1 & t_3 & -t_2 \\ -t_3 & 1 & t_1 \\ t_2 & -t_1 & 1 \end{pmatrix}. \tag{D.14}$$

We now use the following definition for matrix inversion

$$M^{-1} = \frac{1}{\det(M)}\text{adj }(M), \tag{D.15}$$

where the determinant of matrix M, Equation (D.13), is given by

$$\begin{aligned} \det(M) &= (1+t_1^2) + t_3(t_3 - t_1t_2) + t_2(t_1t_3 + t_2) \\ &= 1 + t_1^2 + t_3^2 - t_1t_2t_3 + t_1t_2t_3 + t_2^2 \\ &= 1 + t_1^2 + t_2^2 + t_3^2 \\ &= 1 + \|\boldsymbol{t}\|^2, \end{aligned} \tag{D.16}$$

and the classical adjoint of matrix M, adj(M), is a matrix constructed from M by replacing each element in M by its cofactor and transposing (Aris, 1989). Thus, the classical adjoint of matrix M is given by

$$\mathrm{adj}(M) = \begin{pmatrix} 1+t_1^2 & t_1t_2+t_3 & t_1t_3-t_2 \\ t_1t_2-t_3 & 1+t_2^2 & t_2t_3+t_1 \\ t_1t_3+t_2 & t_2t_3-t_1 & 1+t_3^2 \end{pmatrix}.$$

Thus, Equation (D.15), the inverse of matrix M, is

$$M^{-1} = \frac{1}{1+\|\boldsymbol{t}\|^2} \begin{pmatrix} 1+t_1^2 & t_1t_2+t_3 & t_1t_3-t_2 \\ t_1t_2-t_3 & 1+t_2^2 & t_2t_3+t_1 \\ t_1t_3+t_2 & t_2t_3-t_1 & 1+t_3^2 \end{pmatrix}. \tag{D.17}$$

Substituting the expressions for the matrices M^{-1}, Equation (D.17), and N, Equation (D.14), into Equation (D.12) yields

$$\begin{aligned} V^+ &= \frac{1}{1+\|\boldsymbol{t}\|^2} \begin{pmatrix} 1+t_1^2 & t_1t_2+t_3 & t_1t_3-t_2 \\ t_1t_2-t_3 & 1+t_2^2 & t_2t_3+t_1 \\ t_1t_3+t_2 & t_2t_3-t_1 & 1+t_3^2 \end{pmatrix} \begin{pmatrix} 1 & t_3 & -t_2 \\ -t_3 & 1 & t_1 \\ t_2 & -t_1 & 1 \end{pmatrix} \begin{pmatrix} v_1^- \\ v_2^- \\ v_3^- \end{pmatrix} \\ &= \frac{1}{1+\|\boldsymbol{t}\|^2} \begin{bmatrix} (1+t_1^2-t_2^2-t_3^2)v_1^- + 2[(t_1t_2+t_3)v_2^- - (t_2+t_1t_3)v_3^-] \\ (1-t_1^2+t_2^2-t_3^2)v_2^- + 2[(t_1t_2-t_3)v_1^- + (t_1+t_2t_3)v_3^-] \\ (1-t_1^2-t_2^2+t_3^2)v_3^- + 2[(t_1t_3+t_2)v_1^- - (t_1+t_2t_3)v_2^-] \end{bmatrix}, \end{aligned} \tag{D.18}$$

which is identical to Equation (D.6). Thus using tensor analysis to evaluate Equation (D.1) we have reproduced an equivalent result to using the Boris equations, Equations (D.2) and (D.3).

Appendix E

The particle-in-cell technique models a plasma as being composed of a large number of particles. A state vector, containing a position and a velocity, is then created for each particle. One advantage of this is that the evolution of the velocity distributions can be tracked throughout the simulation and kinetic effects, such as plateau formation on the velocity distribution can be observed.

To obtain the velocity distribution of each plasma species, we appeal to the definition of the one dimensional velocity distribution as given in kinetic theory. The one dimensional velocity distribution $f(x, v_x)$ is defined so that

$$dN = f(x, v_x)\, dx\, dv_x, \tag{E.1}$$

is the number of particles with a position x^* satisfying $x < x^* < x + dx$ and whose velocity v_x^* lies in the range $v_x < v_x^* < v_x + dv_x$. We are interested primarily in the case when the velocity distribution is uniform in space. In this case, $f(x, v_x)$ is independent of x and we can write, with some abuse of notation,

$$\Delta N = \left[\int_0^L f(v_x)\, dx\right]\, dv_x = L f(v_x)\, dv_x, \tag{E.2}$$

where ΔN now represents the number of particles, contained within the entire (one dimensional) volume L, having a velocity v_x^* that lies in the range $v_x < v_x^* < v_x + dv_x$.

To adapt Equation (E.2) for our purposes, we partition the velocity space into M equal intervals of size Δv over the range of interest. We denote the lower limit of this range by $v_{\min}$ and the upper limit by $v_{\max}$. Then

$$\Delta v = \frac{v_{\max} - v_{\min}}{M}. \tag{E.3}$$

We denote the lower limit of the ith interval by

$$v_i = v_{\min} + i\Delta v \qquad (i = 0, \ldots, M-1). \tag{E.4}$$

Thus, the range of velocities v_x spanned by the interval i satisfy

$$v_i \leq v_x < v_i + \Delta v. \tag{E.5}$$

By counting the number of particles ΔN_i in the simulation box with a velocity v_x satisfying Equation (E.5), i.e., whose velocity lies within the ith velocity "bin", we obtain, according to Equation (E.2),

$$\Delta N_i \simeq L f(v_i)\, \Delta v, \tag{E.6}$$

where true equality is approached in the limit of infinitesimal Δv. Equation (E.6) is readily rearranged to provide us with an estimate for the velocity distribution $f(v_i)$ evaluated at the discrete points v_i, defined in Equation (E.4). Thus we obtain the estimate

$$f(v_i) = \frac{\Delta N_i}{L\, \Delta v}, \tag{E.7}$$

where ΔN_i is the number of particles in the simulation box with v_x satisfying Equation (E.5), L is the size of the box and Δv is given by Equation (E.3).

However, the velocity distributions in Equations (2.1) and (2.5), the Maxwellian and kappa distributions, respectively, are normalised velocity distributions, usually denoted by $\hat{f}(v_x)$, which is related to $f(v_x)$ by

$$\hat{f}(v_x) = \frac{1}{\bar{n}} f(v_x),$$

where $\bar{n} = N/L$ is the average number density in one dimension. Thus for direct comparison with Equations (2.1) and (2.5), we need to divide Equation (E.7) by $\bar{n}$, which yields our final result

$$\hat{f}(v_i) = \frac{\Delta N_i / N}{\Delta v}. \tag{E.8}$$

Thus, using Equation (E.8) we are able to probe the velocity distributions of each plasma species present in the plasma. Note that in Equations (2.1) and (2.5) the "hat" on f has been omitted, as is done throughout this thesis when using Equation (E.8).

Appendix F

Overview of the simulation code, directories and files

A one dimensional particle-in-cell simulation code was created, using the C programming language, and described in this thesis. The simulation code is contained in the folder labelled *ESPIC* (Electrostatic Particle-In-Cell) provided on the accompanying compact disk. Presented below is a brief description of the particle-in-cell simulation code we created.

The computation of the simulation was broken up into segments and each segment was written to a separate file. Each file, thus, contains functions written to control a specific portion of the simulation computations, each of which will be described below. This was done to provide a separation of concerns in the simulation code, aiding in the testing of the code at each stage of development. Contained in the folder *ESPIC* are the following files:

- `main.c`: controls the flow of the simulation by calling the functions contained in the other files, when needed.
- `field_solver.c` and the header file `field_solver.h`: contain the functions concerned with calculating the electric field at the simulation grid points, using discrete Fourier transforms.
- `movie.c` and the header file `movie.h`: contain the functions concerned with creating the phase space configuration plots for every plasma species, as well as the plot of the electric field as a function of x/λ_{De}. These plots are combined into a movie clip at the end of the simulation run.

- `plasma.c` and the header file `plasma.h`: contain the functions concerned with controlling the dynamics of each plasma species. This includes loading each plasma species into the simulation box and updating the position and velocity of each plasma particle at every time step.

- `simulation.c` and the header file `simulation.h`: contain the functions concerned with initialising and resetting the simulation grids, correcting the grid quantities at the simulation boundaries as well as creating the simulation output directories (described later).

- `xmltools.c` and the header file `xmltools.h`: contain the functions concerned with reading in data from an input file. Our simulation code utilises input files which are given in .xml format, where the input parameter values are given between parameter name tags (see the sample input file displayed below). The parameter name tags are read first, after which the associated parameter value is assigned to the simulation variable corresponding to the name tag.

The folder *ESPIC* also contains a `Makefile`, used to build the simulation code, creating the executable run file `espic`, and the directory *input*, used to store all the simulation input files (in .xml format). A sample input file is given below,

```
<espic_params>
   <run_control>
               <num_cells>1024.0</num_cells>
               <box_length>512.0</box_length>
               <timestep>0.1</timestep>
               <iterations>60000</iterations>
               <write_energy>50</write_energy>
               <write_ptcl_state>250</write_ptcl_state>
               <movie_interval>10</movie_interval>
               <E_plot_bounds_min>-1.0</E_plot_bounds_min>
               <E_plot_bounds_max>1.0</E_plot_bounds_max>
               <cyclotron_freq>-0.5</cyclotron_freq>
               <theta>90.0</theta>
               <phi>0.0</phi>
   </run_control>
   <plasma>
               <species>
                       <name>electrons</name>
                       <vel_dist>kappa</vel_dist>
                       <kappa_val>2.0</kappa_val>
                       <num_ptcl>2097152</num_ptcl>
                       <plasma_freq>1.0</plasma_freq>
```

```
                <charge_to_mass>-1.0</charge_to_mass>
                <thermal_speed>1.0</thermal_speed>
                <drift_speed>0.0</drift_speed>
                <vel_plot_bounds_min>-20.0</vel_plot_bounds_min>
                <vel_plot_bounds_max>20.0</vel_plot_bounds_max>
        </species>
        <species>
                <name>ions</name>
                <vel_dist>kappa</vel_dist>
                <kappa_val>2.0</kappa_val>
                <num_ptcl>2097152</num_ptcl>
                <plasma_freq>0.1</plasma_freq>
                <charge_to_mass>0.01</charge_to_mass>
                <thermal_speed>0.01</thermal_speed>
                <drift_speed>0.0</drift_speed>
                <vel_plot_bounds_min>-0.5</vel_plot_bounds_min>
                <vel_plot_bounds_max>0.5</vel_plot_bounds_max>
        </species>
    </plasma>
</espic_params>
```

The simulation run parameter values are given between the starting tag, `<param_name>`, and end tag, `</param_name>`. The `<run_control>`...`</run_control>` tags encapsulate the parameters associated with the simulation box and diagnostic output. These are

- `num_cells`: the number of cells in the simulation box.
- `box_length`: the length of the simulation box.
- `timestep`: the time step used in the simulation.
- `iterations`: the number of time steps the simulation will be run for.
- `write_energy`: the interval at which the energies in the plasma are written to file, i.e., every 50 time steps here.
- `write_ptcl_state`: the interval at which the particle state vector, in the form $[x, v_x, v_y, v_z]$, is written to file, i.e., every 250 time steps here.
- `movie_interval`: the interval at which the phase space configuration plots are exported in image format, i.e., every 10 time steps here.
- `E_plot_bounds_min` and `E_plot_bounds_max`: the upper and lower bounds in the plot of the electric field, i.e., the plot will be created between [`E_plot_bounds_min` , `E_plot_bounds_max`], over the range of x/λ_{De} values.

- `cyclotron_freq`: the cyclotron frequency of one of the plasma species, $\omega_c = qB/m$. The magnetic field in the plasma is then calculated using the cyclotron frequency, i.e., $B = \omega_c m/q$.
- `theta`: the angle of inclination of the magnetic field, in degrees, given with reference to the x axis.
- `phi`: the azimuthal angle of the magnetic field in the $x - y$ plane, in degrees, given with reference to the x axis.

The `<species>...</species>` tags encapsulate the plasma species parameters, where any number of plasma species may be present. These are,

- `name`: a name given to the plasma species.
- `vel_dist`: the velocity distribution used to model the particles (`maxwellian` or `kappa`).
- `kappa_val`: the value of κ, used when the particles are modelled by a kappa velocity distribution. If the Maxwellian distribution is chosen, this parameter will not be read.
- `plasma_freq`: the natural frequency of the plasma species.
- `charge_to_mass`: the charge to mass ratio, q/m, for the plasma species.
- `thermal_speed`: the thermal velocity of the particles.
- `drift_speed`: the drift velocity of the particles.
- `vel_plot_bounds_min` and `vel_plot_bounds_max`: the upper and lower bounds used in the phase space configuration plot for this species, .i.e., the plot will be created between [`vel_plot_bounds_min`, `vel_plot_bounds_max`], over the range of x/λ_{De} values.

Implementation of the Manager-Workers pattern

Our simulation code was parallelised using Message Passing Interface (MPI). This allowed the code to be run on a distributed memory system. Inter-processor communication, when using MPI, is controlled by the default MPI

communication object `MPI_COMM_WORLD`, which includes all the processors in the communication.

In our simulation code, we implemented the Manager-Workers pattern as an improvement to our parallelisation scheme. This involved the separation of tasks in our simulation (see Section 2.6 (p. 34) for a description of the Manager and Worker tasks). To achieve the separation of tasks, a separate workers communication object was required, in addition to the default MPI communicator. This was to allow independent communication between the workers, set apart from the manager processor. Defining a new communication object in MPI is done as follows,

```
int num_proc;            // the number of processors
int my_rank;             // the rank of each processor
int root_rank = 0;

/* Initialise MPI */
MPI_Init( &argc, &argv );

/* assign a value to num_proc and my_rank */
MPI_Comm_size ( MPI_COMM_WORLD, &num_proc );
MPI_Comm_rank ( MPI_COMM_WORLD, &my_rank );

MPI_Group  group_world, group_worker;
MPI_Comm   comm_worker;

/* Creates the worker group and communicator */
MPI_Comm_group ( MPI_COMM_WORLD, &group_world);
MPI_Group_excl ( group_world, 1, &root_rank, &group_worker );
MPI_Comm_create( MPI_COMM_WORLD, group_worker, &comm_worker );
```

where the created communication object `comm_worker` controls the inter-processor communication between the Workers.

The kappa velocity loader

Our particle-in-cell simulation code incorporated a kappa distributed velocity loader. The kappa loader we devised generates deviates from the kappa distribution by sampling from the closely related Student t distribution, using the method described in Section 2.1.2 (p. 15). This is done as follows,

```
 /*
* The kappa velocity loader
* inputs are the initial thermal velocity (vth) and the kappa indicie (kp)
*
*/
static double kappa_random_deviate ( double vth, double kp )
{
     double kappa  = kp;
     double mu     = 0.0;
     double nu     = (2 * kappa) - 1;

     double u1     = uniform_random_deviate (  );
     double u2     = uniform_random_deviate (  );

     double sigma  = sqrt((kappa - 1.5)/(kappa - 0.5)) * vth;
     double y      = sqrt(nu * (pow(u1, -2/nu) - 1)) * cos(2 * M_PI * u2);

     double deviate;

     deviate = mu + (sigma * y);

     return deviate;
}
```

Code dependencies

Our simulation code was written using the C programming language, thus a C compiler, such as gcc, is required to compile the simulation code. Furthermore, the Open MPI library is required to compile and run the parallelised simulation code. Our code utilises the Fastest Fourier Transform in the West (FFTW) library, to perform the Fourier transforms and the PLPLOT library is used to produce the phase space configuration plots during the simulation run.

Running the code

Presented here are instructions to run our simulation code, provided on the accompanying compact disk, from a UNIX terminal. To run the simulation code requires that the folder *ESPIC* be copied from the compact disk to the home directory on you computer. This can be done by issuing the following command in a terminal,

```
cp -r /media/cdrom/ESPIC /home/<user_name>
```

To build the code requires you to be in the same directory as the `Makefile`, which contains the commands necessary to build the simulation code, and is located in the *ESPIC* directory. This is done by first issuing the command,

```
cd /home/<user_name>/ESPIC
```

to move into the *ESPIC* directory and

```
make
```

to build the code, creating the object files as well as the executable file `espic`. If no errors were displayed when building the code, you may execute the file `espic` and run the simulation using the following MPI command

```
mpi-exec -np <number_of_processors> ./espic <input_file_name>
```

where `<number_of_processors>` is the number of processors on which the simulation code will be run and `<input_file_name>` is the name of the input file, without the .xml extension.

When the simulation is started, the *input* directory is searched for the input file. If the file is found and is of the correct format, the simulation will progress, alternatively, if it is not found, an error will be displayed and execution of the simulation will stop. If, however, no errors are displayed, a number of output folders are created which will contain the simulation diagnostic outputs. The root folder for the diagnostic outputs is created in the same directory as *ESPIC* and is given a name corresponding to the name of the input file, followed by the time stamp corresponding to the start of the simulation execution. The simulation then runs for the allocated amount of steps.

A series of simulations may also be set to run consecutively using shell scripting. An example of running two simulations using such a scripting file is,

```
#! /bin/bash

make clean
```

```
make
mpi-exec -np <number_of_processors> ./espic <input_file_name1>

make clean
make
mpi-exec -np <number_of_processors> ./espic <input_file_name2>
```

Bibliography

Abreu, P., Fonseca, R. A., Pereira, J. M., and Silva, L. O. (2011). PIC codes in new processors: A full relativistic PIC code in CUDA-enabled hardware with direct visualization. *IEEE Trans. Plasma Sci.*, 39:675 – 685.

Adam, J. C., Serveniere, A. G., and Langdon, A. B. (1982). Electron subcycling in particle simulation of plasmas. *J. Comput. Phys.*, 47:229 – 244.

Anderson, R. R., Parks, G. K., Eastman, T. E., Gurnett, D. A., and Frank, L. A. (1981). Plasma waves associated with energetic particles streaming into the solar wind from the Earth's bow shock. *J. Comput. Phys.*, 86:4493 – 4510.

Appert, K. and Vaclavik, J. (1981). Tail formation by nonresonant interaction of ions with ion acoustic turbulence. *Plasma Phys.*, 23(9):763 – 774.

Aris, R. (1989). *Vectors, Tensors, and the Basic Equations of Fluid Mechanics*. Dover Publications, INC.

Aydemir, A. Y. (1994). A unified Monte Carlo interpretation of particle simulations and applications to non-neutral plasmas. *Phys. Plas.*, 1(4).

Bailey, R. W. (1994). Polar generation of random variates with the $t-$distribution. *Math. of Comput.*, 62:779 – 781.

Baldwin, D. E. and Rowlands, G. (1966). Plasma oscillations perpendicular to a weak magnetic field. *Phys. Fluids*, 9(12):2444.

Benson, F. R., Osherovich, V. A., Fainberg, J., and Reinisch, B. W. (2003). Classification of IMAGE/RPI-stimulated plasma resonances for the accu-

rate determination of magnetospheric electron-density and magnetic field values. *J. Geophys. Res.*, 108(A5):SMP16–1 – SMP16–14.

Benson, F. R., Osherovich, V. A., Fainberg, J., Vinas, A. F., and Rupert, D. R. (2001). An interpretation of banded magnetospheric radio emissions. *J. Geophys. Res.*, 106(A7):13179 – 13190.

Berger, M. J. and Oliger, J. (1984). Adaptive mesh refinement for hyperbolic partial differential equations. *J. Comput. Phys.*, 53:484 – 512.

Bernstein, I. B. (1958). Waves in a plasma in a magnetic field. *Phys. Rev.*, 109:10 – 21.

Bertrand, P. (2005). Vlasov code applications. In *Proceedings of ISSS-7*.

Bettencourt, M. T. and Greenwood, A. D. (2008). Performance improvements for efficient electromagnetic particle-in-cell computation on 1000s of CPUs. *IEEE Trans. Antennas and Propagation*, 56:2178 – 2186.

Birdsall, C. K. (1991). Particle-in-cell charged-particle simulations, plus monte carlo collisions with neutral atoms, PIC-MCC. *IEEE Trans. Plas. Sci.*, 19(2):65 – 85.

Birdsall, C. K. and Fuss, D. (1969). Clouds-in-clouds, clouds-in-cells physics for many body plasmas. *J. Comput. Phys.*, 3:494 – 511.

Birdsall, C. K. and Langdon, A. B. (1985). *Plasma Physics via Computer Simulation*. McGraw-Hill Book Company.

Biskamp, D. and Chodura, R. (1971). Computer simulation of anomalous resistivity. *Phys. Rev. Lett.*, 27:1553.

Boris, J. P. (1970). Relativistic plasma simulation-optimization of a hybrid code. In *Proceedings of the Fourth Conference on Numerical Simulation of Plasmas*, page 3.

Box, G. E. P. and Muller, M. E. (1958). A note on the generation of random normal deviates. *Ann. Math. Stat.*, 29(2):610 – 611.

Brackbill, J. U. (1993). An adaptive grid with directional control. *J. Comput. Phys.*, 108(1):38 – 50.

Brecht, S. H., Lyon, J. G., Fedder, J. A., and Hain, K. (1981). A simulation study of the east-west IMF effects on the magnetosphere. *Geophys. Res. Lett.*, 8:397.

Brecht, S. H., Lyon, J. G., Fedder, J. A., and Hain, K. (1982). A time dependent three dimensional simulation of the Earth's magnetosphere: Reconnection events. *J. Geophys. Res.*, 87:6098.

Bryant, D. A. (1996). Debye length in a kappa-distributed plasma. *J. Plas. Phys.*, 56(1):87 – 93.

Buneman, O. (1959). Dissipation of currents in ionized media. *Phys. Rev.*, 115(3):503 – 517.

Burgess, D. (2006). Interpreting multipoint observations of substructure at the quasi-perpendicular bow shock: Simulations. *J. Geophys. Res.*, 111.

Buschmann, F., Meunier, R., Rohnert, H., Sommerland, P., and Stal, M. (1996). *Pattern-Oriented Software Architecture*. John Wiley and Sons, Ltd.

Byers, J. A. and Grewal, M. (1970). Perpendicular propagating plasma cyclotron instabilities simulated with a one-dimensional computer model. *Phys. Fluids*, 13(7):1819 – 1830.

Cairns, R. A., Mamum, A. A., Bingham, R., Bostrom, R., Dendy, R. O., Nairn, C. M. C., and Shukla, P. K. (1995). Electrostatic solitary structures in non-thermal plasmas. *Geophys. Res. Lett.*, 22:20.

Carlson, C. W., Pfaff, R. F., and Watzin, J. G. (1998). The fast auroral snapshot (FAST) mission. *Geophys. Res. Lett.*, 25(12):2013 – 2016.

Chen, F. F. (2006). *Plasma Physics and Controlled Fusion*. Springer Science, second edition.

Christon, S. P., Mitchell, D. G., Williams, D. J., Frank, L. A., Huang, C. Y., and Eastman, T. E. (1988). Energy spectra of plasma sheet ions and electrons from $\approx$ 50 ev/e to $\approx$ 1 mev during plasma temperature transitions. *J. Geophys. Res.*, 93(A4):2562 – 2572.

Christon, S. P., Williams, D. J., Mitchell, D. J., Frank, L. A., and Huang, C. Y. (1989). Spectral characteristics of plasma sheet ion and electron populations during undisturbed geomagnetic conditions. *J. Geophys. Res.*, 94(A10):13409 – 13424.

Cohen, B. I., Langdon, A. B., and Friedman, A. (1982). Implicit time integration for plasma simulation. *J. Comput. Phys.*, 46:15 – 38.

Cooley, J. W. and Turkey, J. W. (1965). An algorithm for the machine calculation of complex fourier series. *Math. Comput.*, 19:297 – 301.

Crary, F. J., Goldman, M. V., Ergun, R. E., and Newman, D. L. (2001). Explanation for the simultaneous occurrence of bipolar structures and waves near ion-cyclotron harmonics in the auroral ionosphere. *Geophys. Res. Lett.*, 28(15):3059 – 3062.

Crawford, F. W. (1965). A review of cyclotron harmonic phenomena in plasmas. *Nucl. Fusion*, 5:73 – 84.

Crumley, J. P., Cattell, C. A., Lysak, R. L., and Dombeck, J. P. (2001). Studies if ion solitary waves using simulations including hydrogen and oxygen. *J. Geophys. Res.*, 106:6007 – 6015.

Dawson, J. M. (1962). One-dimensional plasma model. *Phys. Fluids*, 5(4):445 – 459.

Dawson, J. M. (1964). Thermal relaxation in a one-species, one-dimensional plasma. *Phys. Fluids*, 7:419 – 425.

Dawson, J. M. (1983). Particle simulation of plasmas. *Rev. Mod. Phys*, 55(2):403 – 447.

Dawson, J. M. (1985). The future of space plasma simulation. *Space Sci. Rev.*, 42:187 – 208.

Dawson, J. M., Decyk, V. K., Sydora, R., and Liewer, P. (1993). High-performance computing and plasma physics. In *Physics Today*, pages 64 – 70.

Decyk, V. K. and Singh, T. V. (2011). Adaptable particle-in-cell algorithms for graphical processing units. *Comput. Phys. Comm.*, 182:641 – 648.

DeGroot, J. S., Barnes, C., Walstead, A. E., and Buneman, O. (1977). *Phys. Rev. Lett.*, 38:1383.

Denton, R. and Kotschenreuther, M. (1995). δf algorithm. *J. Comput. Phys.*, 119(2):283 – 294.

Denton, R. E., Engerbretson, M. J., Keiling, A., Walsh, A. P., Gary, S. P., Décréau, P. M. E., Cattell, C. A., Glassmeier, K. H., and Rème, H. (2010). Multiple harmonic ulf waves in the plasma sheet boundary layer: Instability analysis. *J. Comput. Phys.*, 115:A12224.

Dougherty, J. P. and Monaghan, J. J. (1966). The theory of resonances observed in ionograms taken by sounders above the ionosphere. *Proc. R. Soc. London Ser. A*, 289(1417):214 – 234.

Drury, L. O. (1983). An introduction to the theory of diffusive shock acceleration of energetic particles in tenuous plasmas. *Rep. Prog. Phys.*, 46:973 – 1027.

Dum, C. T., Chodura, R., and Biskamp, D. (1974). *Phys. Rev. Lett.*, 32:1231.

Ergun, R. E., Carlson, C. W., McFadden, J. P., Mozer, F. S., Muschietti, L., and Roth, I. (1998). Debye-scale plasma structures associated with magnetic-field-aligned electric fields. *Phys. Rev. Lett.*, 81(4):826 – 829.

Forslund, D. W. (1985). Fundamentals of plasma simulation. *Space Sci. Rev.*, 42:3 – 16.

Fredricks, R. W. (1968). Structure of the Bernstein modes for large values of the plasma parameter. *J. Plas. Phys.*, 2:197 – 206.

Gary, S. P., Liu, K., Winske, D., and Denton, R. E. (2010). Ion Bernstein instability in the terrestrial magnetosphere: Linear dispersion theory. *J. Geophys. Res.*, 115:A12209.

Giacalone, J. (2006). The hybrid simulation applied to space plasmas. In *Numerical Modeling of Space Plasma Flows: Astronum-2006 Conference Series*, pages 241 – 250.

Gloeckler, G., Geiss, J., Balsiger, H., Bedini, P., Cain, J. C., Fischer, J., Fisk, L. A., Galvin, A. B., Gliem, F., Hamilton, D. C., Hollweg, J. V., Ipavich, F. M., Joos, R., Livi, S., Lundgren, R., Mall, U., Mckenzie, J. F., Ogilvie, K. W., Ottens, F., Rieck, W., Tums, E. O., von Steiger, R., Weiss, W., and Wilken, B. (1992). The solar wind ion composition spectrometer. *Astron. Astrophys. Suppl. Series*, 92:267 – 289.

Gloeckler, G. and Hamilton, D. C. (1987). AMPTE ion composition results. *Phys. Scripta*, T18:73.

Gradshteyn, I. S. and Ryzhik, I. M. (2007). *Table of Integrals, Series and Products*. Elsevier Inc., seventh edition.

Groth, C. P. T., Zeeuw, D. L. D., Gombosi, T. I., and Powell, K. G. (2000). Global three-dimensional MHD simulation of a space weather event: CME formation, interplanetary propagation, and interaction with the magnetosphere. *J. Comput. Phys.*, 105:25 053.

Gurnett, D. A. and Anderson, R. R. (1977). Plasma wave electric fields in the solar wind: Initial results from Helios 1. *J. Geophys. Res.*, 82(4):632 – 650.

Gurnett, D. A. and Frank, L. A. (1978). Ion acoustic waves in the solar wind. *J. Geophys. Res.*, 83(A1):58 – 74.

Hellinger, P., Trávníček, P., and Menietti, J. D. (2004). Effective collision frequency due to ion-acoustic instability: Theory and simulations. *Geophys. Res. Lett.*, 31(L10806):1 – 4.

Henning, F. D., Mace, R. L., and Pillay, S. R. (2011). Electrostatic Bernstein waves in plasmas whose electrons have a dual kappa distribution: Applications to the Saturnian magnetosphere. *J. Geophys. Res.*, 116.

Hockney, R. W. (1965). A fast direct solution of poisson's equation using Fourier analysis. *J. Assoc. Comput. Mach.*, 12:95 – 113.

Hockney, R. W. (1966). Computer simulation of anomalous plasma diffusion and numerical solution of poisson's equation. *Phys. Fluids*, 9:1826 – 1835.

Hockney, R. W. and Eastwood, J. W. (1981). *Computer Simulation Using Particles*. New York: McGraw-Hill.

Horne, R. B., Wheeler, G. V., and Alleyne, H. S. C. K. (2000). Proton and electron heating by radially propagating fast magnetosonic waves. *J. Geophys. Res.*, 105(A12):27597 – 27610.

Horowitz, E. J., Shumaker, D. E., and Anderson, D. V. (1989). QN3D: A three-dimensional quasi-neutral hybrid particle-in-cell code with applications to the tilt mode instability in field reversed configurations. *J. Comput. Phys.*, 84:279 – 310.

Huba, J. D., Joyce, G., and Fedder, J. A. (2000). Ion sound waves in the topside low latitude ionosphere. *Geophys. Res. Lett.*, 27:3181 – 3184.

Huff, R. W., Dawson, J. M., and Culler, G. (1982). Computer modeling in plasma physics on the parallel-architecture CHI computer. In *Parallel Computations*, page 365. Academic Press.

Ichimaru, S. (1973). *Basic Principles of Plasma Physics: A statistical Approach*. Westview Press.

Ishihara, A. (1971). *Statistical Physics*. Academic Press, Inc.

Jackson, R. and Zaidman, E. (1987). In *Twelfth Conf. on the Numerical Sim. of Plasmas*, page paper iW2.

Janhunen, P., Olsson, A., Vaivads, A., and Peterson, W. K. (2003). Generation of Bernstein waves by ion shell distributions in the auroral region. *Ann. Geophys.*, 21:881 – 891.

Kamimura, T., Wagner, T., and Dawson, J. M. (1978). Simulation study of Bernstein modes. *Phys. Fluids*, 21(7):1151 – 1167.

Kasaba, Y., Matsumoto, H., and Omura, Y. (2001). One- and two-dimensional simulations of electron beam instability: Generation of electrostatic and electromagnetic $2f_p$ waves. *J. Geophys. Res.*, 106:18,693 – 18,711.

Kennel, C. F. and Ashour-Abdalla, M. (1982). Electrostatic waves and the strong diffusion of magnetospheric electrons. In *Magnetospheric Plasma Physics*, pages 244 – 344.

Kleiman, S., Devang, S., and Smaalders, B. (1996). *Programming with Threads*. Sun Microsystems, Inc.

Koen, E. J., Collier, A. B., and Maharaj, S. K. (2012a). Particle-in-cell simulations of beam-driven electrostatic waves in a plasma. *Phys. Plas.*, 19:042101.

Koen, E. J., Collier, A. B., and Maharaj, S. K. (2012b). A simulation approach of high-frequency electrostatic waves found in Saturn's magnetosheath. *Phys. Plas.*, 19:042102.

Krall, N. A. and Trivelpiece, A. W. (1973). *Principles of Plasma Physics*. McGraw-Hill.

Labelle, J., Ruppert, D. R., and Treumann, R. A. (1999). *J. Geophys. Res.*, 104:293.

Labelle, J. and Treumann, R. A. (1988). Plasma waves at the dayside magnetopause. *Space Sci. Rev.*, 47:175 – 202.

Landau, L. (1946). On the vibration of the electronic plasma. *J. Phys. USSR*, 10:25.

Lapenta, G. (2012). Particle simulations of space weather. *J. Comput. Phys.*, 231(3):795 – 821.

Leboeuf, J. N., Tajima, T., Kennel, C. F., and Dawson, J. M. (1978). Global simulations of the time-dependent magnetosphere. *Geophys. Res. Lett.*, 5:609.

Leboeuf, J. N., Tajima, T., Kennel, C. F., and Dawson, J. M. (1981). Global simulations of the three-dimensional magnetosphere. *Geophys. Res. Lett.*, 8:257.

Leubner, M. P. (2004). Fundamental issues on kappa-distributions in space plasmas and interplanetary proton distributions. *Phys. Plas.*, 11(4):1308 – 1316.

Liewer, P. C. and Decyk, V. K. (1989). A general concurrent algorithm for plasma particle-in-cell simulation codes. *J. Comput. Phys.*, 85:302 – 322.

Liewer, P. C., Decyk, V. K., Dawson, J. M., and Fox, G. C. (1988). A universal concurrent algorithm for plasma particle-in-cell simulation codes. *Proceedings of the third conference on Hypercube concurrent computers and applications*, 2:53.

Liewer, P. C., Leaver, E. W., Decyk, V. K., and Dawson, J. M. (1990). Dynamic load balancing in a concurrent plasma pic code on the JPL/Caltech Mark III hypercube. *Proc. Fifth Distributed Memory Computing Conf.*, 2:939.

Livadiotis, G. and McComas, D. J. (2009). Beyond kappa distributions: Exploring tsallis statistical mechanics in space plasmas. *J. Geo. Res.*, 114(A11105):1 – 21.

Lu, Q., Shan, L., Shen, C., Zhang, T., Li, Y., and Wang, S. (2011). Velocity distributions of superthermal electrons fitted with a power law function in the magnetosheath: Cluster observations. *J. Geo. Res..*, 116:A03224.

Lu, Q., Wang, S., and Dou, X. (2005). Electrostatic waves in an electron-beam plasma system. *Phys. Plas.*, 12:072903.

Lu, Q., Zhou, L., and Wang, S. (2010). Particle-in-cell simulations of whistler waves excited by an eletron κ distributions in space plasma. *J. Geo. Res..*, 115:A02213.

Lui, K., Gary, S. P., and Winske, D. (2011). Excitation of magnetosonic waves in the terrestrial magnetosphere: Particle-in-cell simulations. *J. Geophys. Res.*, 116:A07212.

Mace, R. L. (2003). A Gordeyev integral for electrostatic waves in a magnetized plasma with a kappa velocity distribution. *Phys. Plas.*, 10(6):2181 – 2193.

Mace, R. L. (2004). Generalized electron Bernstein modes in a plasma with a kappa distribution. *Phys. Plas.*, 11(2):507 – 522.

Mace, R. L. and Hellberg, M. A. (1995). A dispersion function for plasmas containing superthermal particles. *Phys. Plas.*, 2(6):2098 – 2109.

Mace, R. L., Hellberg, M. A., and Treumann, R. A. (1998). Electrostatic fluctuations in plasmas containing suprathermal particles. *J. Plas. Phys.*, 59:393 – 416.

Maksimovic, M., Pierrard, V., and Riley, P. (1997). Ulysses electron distributions fitted with kappa functions. *J. Geophys. Res.*, 24(9):1151 – 1154.

Mani, K., Taylor, C., and Taylor, S. (1992). *An Introduction to Parallel Programming*. Jones and Bartlett Publishers, Inc.

Martino, B. D., Briguglio, S., Vlad, G., and Sguazzero, P. (2001). Parallel pic plasma simulation through particle decomposition techniques. *Parallel Comput.*, 27:295 – 314.

Matsumoto, H. and Omura, Y. (1984). Particle simulation of electromagnetic waves and its application to space plasmas. In *Computer Simulation of Space Plasmas*, pages 43 – 102. Terra Scientific Publishing Co., Tokyo.

Matsumoto, H. and Omura, Y. (1993). *Computer Space Plasma Physics: Simulation Techniques and Software*. Terra Scientific Publishing Co.

Meng, Z., Thorne, R. M., and Summers, D. (1992). Ion-acoustic wave instability driven by drifting electrons in a generalized Lorentzian distribution. *J. Plas. Phys.*, 47:445 – 464.

Morse, R. L. and Nielson, C. W. (1969). Numerical simulation of warm two-beam plasma. *Phys. Fluids*, 12:2418 – 2425.

Okuda, H. and Ashour-Abdulla, M. (1988). Ion acoustic instabilities excited by injection of an electron beam in space. *J. Geophys. Res.*, 93:2011 – 2115.

Okuda, H. and Birdsall, C. K. (1970). Collisions in a plasma of finite-size particles. *Phys. Fluids*, 8:2123 – 2134.

Omidi, N. and Winske, D. (1990). Steepening of kinetic magnetosonic waves into shocklets: Simulations and consequences for planetary shocks and comets. *J. Geophys. Res.*, 95:2281.

Omura, Y. (2007). One-dimensional electromagnetic particle code: KEMPO1, A tutorial on microphysics in space plasmas. In Usui, H. and Omura, Y., editors, *Advanced Methods for Space Simulations*, pages 1 – 21. Terra Scientific Publishing Co., Tokyo.

Ortega-Arjona, J. L. (2004). The Manager Workers pattern: An activity parallelism architecture pattern for parallel programming. In *EuroPLoP conference proceedings*, pages A4–1.

Parker, E. N. and Tidman, D. A. (1958). Suprathermal particles. *Phys. Rev.*, 111(5):1206 – 1211.

Perraut, S., Roux, A., Robert, P., Gendrin, R., Sauvaud, J. A., Bosqued, J. M., Kremser, G., and Korth, A. (1982). A systematic study of ULF waves above F_{H+} from GEOS 1 and 2 measurements and their relationships with proton ring distributions. *J. Geophys. Res.*, 87:6219 – 6236.

Pierrard, V. and Lazar, M. (2010). Kappa distributions: Theory and applications in space plasmas. *Solar Phys.*, 267:153 – 174.

Press, W. H., Teukolsky, S. A., Vetterling, W. T., and Flannery, B. P. (2007). *Numerical Recipes: The Art of Scientific Computing*. Cambridge University Press, third edition.

Puri, S., Leuterer, F., and Tutter, M. (1973). Dispersion curves for the generalised Bernstein modes. *J. Plas. Phys.*, 9:89 – 100.

Qiang, J. and Xiaoye, L. (2010). Particle-field decomposition and domain decomposition in parallel particle-in-cell beam dynamics simulation. *Comput. Phys. Comm.*, 181:2024 – 2034.

Quest, K. B. (1988). Theory and simulation of collisionless parallel shocks. *J. Geophys. Res*, 93:9649.

Russel, C. T., Holzer, R. E., and Smith, E. J. (1970). OGO 3 observations of ELF noise in the magnetosphere 2. The nature of the equatorial noise. *J. Geophys. Res.*, 75(4):755 – 768.

Sato, T. and Okuda, H. (1980). Ion-acoustic double layers. *Phys. Rev. Lett.*, 44:740 – 744.

Scales, W. A., Cheng, K. T., and Srivastava, S. (1997). Simulation studies of processes associated with stimulated electromagnetic emission (SEE) in the ionosphere. *J. Atmos. and Sol. Terres. Phys.*, 59(18):2373 – 2381.

Schippers, P., Blanc, M., André, N., Dandouras, I., Lewis, G. R., Gilbert, L. K., Persoon, A. M., Krupp, N., Gurnett, D. A., Coates, A. J., Krimigis, S. M., Young, D. T., and Dougherty, M. K. (2008). Multi-instrument analysis of electron populations in Saturn's magnetosphere. *J. Geophys. Res.*, 113.

Shaw, W. T. and Lee, K. T. A. (2008). Bivariate student t distributions with variable marginal degrees of freedom and independence. *J. Multivariate Anal.*, 99:1276 – 1287.

Stanchev, P. G., Dorland, W., and Gumerov, N. (2009). Fast parallel particle-to-grid interpolation for plasma simulations on the gpu. *J. Parallel Distrib. Comput.*, 68:1339.

Stewart, J. (2003). *Calculus*. Thomson Learning, Inc, fifth edition.

Stix, T. H. (1992). *Waves in Plasmas*. AIP Press.

Summers, D. and Thorne, R. M. (1991). The modified plasma dispersion function. *Phys. Fluids B*, 3(8):1835 – 1847.

Swanson, D. G. (2003). *Plasma Waves*. IOP Publishing Ltd, second edition.

Sydora, R. D. (1999). Low-noise electromagnetic and relativistic particle-in-cell plasma simulation models. *J. Comput. and Appl. Math.*, 109:243 – 259.

Tajima, T. (1989). *Computational Plasma Physics: With Applications to Fusion and Astrophysics*. Addison-Wesley Publishing Company, Inc.

Tataronis, J. A. and Crawford, F. W. (1970). Cyclotron harmonic wave propagation and instabilities: I. perpendicular propagation. *J. Plas. Phys.*, 4(2):231 – 248.

Thorne, R. M. and Summers, D. (1991). Landau damping in space plasmas. *Phys. Fluids B*, 3(8):2117 – 2123.

Toida, M., Suzuki, T., and Ohsawa, Y. (2003). Multi-ion-species effects on power spectra and autocorrelation functions of ion Bernstein waves. *J. Plas. Fusion Res.*, 79:549 – 550.

Toida, M., Suzuki, T., and Ohsawa, Y. (2004). Collective behaviour of ion Bernstein waves in a multi-ion-species plasma. *Phys. Plas.*, 11(6):3028 – 3034.

Treumann, R. A. and Baumjohann, W. (1997). *Advanced Space Plasma Physics*. Imperial College Press.

Treumann, R. A., Jaroschek, C. H., and Scholer, M. (2004). Stationary plasma states far from equilibrium. *Phys. Plas.*, 11(4):1317 – 1325.

Tsallis, C. (1988). Possible generalization of Boltzmann-Gibbs statistics. *J. Stat. Phys.*, 52(1):479 – 487.

Ueda, H., Omura, Y., Matsumoto, H., and Okuzawa, T. (1994). A study of the numerical heating in electrostatic particle simulations. *Comput. Phys. Comm.*, 79:249 – 259.

Vasyliunas, V. M. (1968). A survey of low-energy electrons in the evening sector of the magnetosphere with OGO 1 and OGO 3. *J. Geophys. Res.*, 73:2839 – 2884.

Verboncoeur, J. P. (2005). Particle simulation of plasmas: Review and advances. *Plasma Phys. Control. Fusion*, 47(5A):A231 – A260.

Viñas, A., Mace, R. L., and Benson, R. F. (2005). Dispersion characteristics for plasma resonances of maxwellian and kappa distribution plasmas and their comparisons to the IMAGE/RPI observations. *J. Geophys. Res.*, 110:A06202.

Walck, C. (2007). *Hand-book on STATISTICAL DISTRIBUTIONS for Experimentalists*. Universitet Stockholms.

Watt, C. E. J., Horne, R. B., and Freeman, M. P. (2002). Ion acoustic resistivity in plasmas with similar ion and electron temperatures. *Geophys. Res. Lett.*, 29(1):1004.

Winske, D. (1985). Hybrid simulation codes with application to shocks and upstream waves. *Space Sci. Rev.*, 42:53.

Winske, D. and Omidi, N. (1996). A nonspecialist's guide to kinetic simulations of space plasmas. *J. Geophys. Res*, 101(A8):17 287 – 17 303.

Yoshiya, T., Toida, M., and Ohsawa, Y. (2004). Numerical studies of magnetosonic waves in thermal equilibrium, multi-ion-species plasmas. *J. Plas. Fusion Res.*, 6:383 – 386.

Yu, S. P., Kooyers, G. P., and Buneman, O. (1965). A time dependent computer analysis of electron-wave interaction in crossed-fields. *J. Appl. Phys.*, 36:2550 – 2559.